SYNTHESIS AND CHARACTERIZATION OF GRAPHENE: A RAMAN STUDY OF THE EFFECT OF ELECTROMAGNETIC AND PROTON IRRADIATIONS ON GRAPHENE

By

Puleng Nontobeko Mbuyisa

Thesis presented in fulfilment of the requirements for the degree of

Master of Science at the University of Zululand.

Supervisor: Prof. M. Maaza

Material Research Group

IThemba LABS

Co-supervisor: Prof. O.M. Ndwandwe

Department of Physics and Engineering

University of Zululand

2009

DECLARATION

I, the undersigned, hereby declare that the work contained in this thesis is my own original work and that I have not previously in its entirety or in part submitted it at any university for a degree.

Signature: ……

Date: ……

ABSTRACT

Graphene, a single atomic layer of hexagonally arranged sp^2–hybridized carbon atoms, with a thickness of only 0.34 nm, exhibits unique properties. The current interest in graphene can be attributed to three main reasons. Firstly, various forms of graphite, nanotubes, buckyballs and others can all be viewed as derivatives of graphene. Secondly, the scalability of graphene devices to nano-dimensions makes it a promising candidate for applications in nano-devices. Thirdly, its electron transport properties are described by the Dirac equation which allows access to quantum electrodynamics in a simple condensed matter experiment. The methods for obtaining individual graphene sheets have progressed, from ripping it with adhesive tape, or gently pushing small graphite crystals along a hard surface to produce high quality graphene by cleaving of graphite, to oxidation of graphite using the modified Hummers method developed by M. Hirata *et al. (Carbon 42(2004)).* In this research the graphene was synthesized using the modified Hummers method which resulted in a suspension of graphene oxide flakes in distilled water. The graphene oxide (GO) was then chemically reduced to produce graphene or reduced graphene oxide (rGO). The physical properties of the resulting graphene films were characterized and the effects of irradiation by an excimer pulsed laser (UV radiations), visible light (green) and proton irradiation were investigated. During the irradiations the dose of the radiation was varied in order to track the changes in the properties of the materials as a function of the flux. The different spots were then characterized using Raman spectroscopy to measure the created disorder. The Raman spectra of the samples irradiated by light displayed the D and G mode. The Raman spectra characteristics for the UV irradiated sample were similar to that of the proton irradiated sample. In both cases there was a splitting of the G mode. It was then concluded that the splitting of the G band similar to that found in semiconducting Single Walled Nanotubes is an indication that the samples are semiconducting. However the G line shape is highly sensitive to whether the SWNT is metallic or semiconducting and in the UV irradiated sample there was a transition from semiconducting to more metallic as the irradiation was increased.

ACKNOWLEDGEMENTS

Above all I would like to thank God for giving me life and hope, for the people who have played their part in my life to make me the strong independent women that I am today. I also wish to send a special thank you to the Mbuyisa and Khumalo family and especially to my parents Sipho and Margaret Mbuyisa for their support and understanding; I would not have survived without their love.

I would like to express my sincere appreciation to:

- Prof M Maaza, my supervisor, for his guidance, support and encouragement that enabled me to reach my full potential in the course of this research.
- Prof OM Ndwandwe, my co-supervisor, for the opportunity to be part of the Manus/Matsci program and for his interest in the progress and successful completion of my project.
- Dr A Nechaev, Post Doc at iThemba Labs, for his assistance in the lab and with the preparation of the graphene solutions. Also for always having his office door open and for being willing to discuss my work.
- Dr R Nemutudi, MRD head, for helping me with the sample preparation for transport measurements and for dealing with students affairs with so much consideration for the students.
- Prof T Doyle, S-block iThemba LABS, for his assistance in the transport measurements, for his time and for the enthusiasm towards my work.
- Mr U Buttner, Physics and Engineering department at the University of Stellenbosch, for the warm welcome, assistance and opportunity to make use of the equipment.
- Mrs M Waldron, UCT, for her assistance with the SEM unit.
- Gerald Malgas for the HRSEM, James Ramontja for the FTIR and especially Manfred Scriba for the HRTEM and for organizing my visit.
- All the guys at the CSIR who assisted me.
- Prof M Chhowalla and his group, especially Dr G Eda, of Rutgers University, for the samples and advice.
- Yulanda Rumo and Ntsiki, TUT, for their patience and for assisting me to master the use of Raman spectroscopy and to the TUT for granting me access to their facilities.

- All the MRG staff, especially Dr M Nkosi in the solid state LAB, Mr P Sechogela for the proton irradiations, Ms Cuba for the administrative assistance and Ms Mabotshwa for the honest advice.
- All the University of Zululand staff, especially Ms B Kibirige, Dr Nemorou and Prof Sendezera. You guys laid the foundation for my academic success.
- All my colleagues at MRG with special mention to Mr C Ndlangamandla and K Saleh, thank you for all your support. Every discussion I had with all you guys made a difference.
- Finally Ms Shozi, Mr Majola, Mr Sefage, Mr Malindisa and Mr Nzimande, for being there when I needed you most last year. May God bless you and make you fruitful.
- The National Research foundation for their financial support towards my Honours and Masters degree.

TABLE OF CONTENTS

CHAPTER 1 ***1***

1.1 Introduction **1**

1.2 Historical survey **4**

1.3 Aim and Motivation of Investigation **6**

1.3.1 Aim of the project 6
1.3.2 Project objectives 6
1.3.3 Benefits of the research 7
1.3.4 Scope of investigation 7

CHAPTER 2 ***8***

2.1 Literature Review **8**

2.1.1 Properties of graphene 8
2.1.2 Structural properties 11
2.1.3 Mechanical properties 12
2.1.4 Thermal conductivity 12
2.1.5 Electronic-conductivity properties 12
2.1.6 Photo-electric properties 13
2.1.7 Electromagnetic properties 14
2.1.8 Influence of particle irradiation on graphite properties 15
2.1.9 Graphene sheets applications 16
2.1.10 Methods for producing graphene sheets 17

CHAPTER 3 ***20***

3.1 Characterization techniques **20**

3.1.1 Atomic Force Microscopy (AFM) 20
3.1.2 Scanning Electron Microscopy (SEM) 23
3.1.3 Transmission Electron Microscope (TEM) 25
3.1.4 Fourier Transform Infrared Spectroscopy (FTIR) 27
3.1.5 Raman Spectroscopy 29
3.1.6 Ultra-Violet and Visible Absorption Spectroscopy 32

CHAPTER 4 ***35***

4.1 Experimental procedure **35**

4.1.1 Hummers method 35
4.1.2 Reduction 36
4.1.3 Cleaning of substrates 37
4.1.4 Sample preparation 37
4.1.5 Annealing conditions 37
4.1.6 Reduced Graphene Oxide irradiation 38

CHAPTER 5 ***39***

5.1 Results and discussion **39**

5.1.1 Morphology 39
5.1.2 Structure 51
5.1.3 Optical properties 55
5.1.4 Current - Voltage Characteristics 63
5.1.5 Raman spectroscopic studies of irradiated graphene 65

CHAPTER 6 _____ *75*

6.1 Conclusion _____ **75**

6.2 References _____ **79**

LIST OF FIGURES

Figure 1-1 Fuel element design at PBMR with cross section of the pebble showing the layers of coatings [scienceinafrica2009] 3
Figure 1-2 Solar cell characteristics of an OPV with a reduced GO thin film as the transparent electrode measured in the dark and under illumination [Goki Eda *et al.*APL92 2008]. 3
Figure 2-1 carbon phase diagram [] 9
Table 1 Table of comparison for graphite, diamond and diamond-like carbon properties 10
Figure 2.2 Schematic of the sp2 hybridized structure of graphene showing the sigma bonds and the 2p free electrons (above and below the sigma orbit & plane) [6] 11
Figure 3-1 Cantilever with deflection detection system scanning the sample. The sample is visualized on a computer with installed scan software which directs the scan itself [36] 22
Figure 3-2 Typical AFM images and the corresponding height profiles of the graphene. The thicknesses of the graphenes are 1.9–2.3 nm, 1.3–2.1 nm, and 1.1–1.3 nm, respectively [13]. The pronounced roughness is attributed by sp^3 centers and point defects in the carbon lattice that cause wrinkling of the sheets [39] 22
Figure 3-3 Diagram of electron beam path in a SEM courtesy of unl.edu 24
Figure 3-4 Typical SEM micrographs of graphene from different graphite materials [] 24
Figure 3-6 Interactions between material and electrons schetch courtesy of Fichiers chap3 26
Figure 3-5 Image of Scanning Electron Microscopy setup. Nobelprize.org [] 26
Figure 3-7 Typical HRTEM images of (a) single-, (b) double-, and (c) triple-layer graphene sheets with folded edges obtained by chemical exfoliation [] 26
Figure 3-8 Fourier Transform Infrared spectroscopy setup courtesy of thermonicolet.com 28
Figure 3-9 IR spectrum (400-4000cm-1) of as-made GS and GO. The shading region is from about 1400 to 1900 cm^{-1} showing the signal of carboxylic groups [].The absorption at 3390cm-1 indicates the presences of the hydroxyl (OH group) and at a wavenumber of 1629cm-1 and 1720 cm-1 indicates the presence of the carbonyl and carboxyl respectively [31] 28
Figure 3-10 The entire Raman spectra for a single- and multi-layered reduced Graphene Oxide [] .The three major carbon features (D, G and 2D peaks) along with the Si peaks from the substrates are labeled. The prominent D peak in the Raman spectra is an indication of the presence of disorder in the samples [46] 30
Figure 3-11 The possible electron band structures in solids at 0 K. (a)The one outermost band is only partially filled with electrons, this energy band structure is typical of metals with a single s valence electron. (b) The electron band structure of metals, wherein there is an overlap of filled and empty outer bands. (c) The electron band structure of insulators, the filled valence band is separated from the empty conduction band by a large band gap (>2 eV) .(d) The ban structure found in semiconductors with a narrow band gap(<2 eV) 34
Figure 3-12 Tauc plot for estimating the optical band gap of thin films 34
Figure 4-1 Transformation of clear yellow graphene oxide to black graphene sheets suspension 36
Figure 5-1 3D image of Graphene oxide reference sample deposited on glass by spin coating at 5500 rmps.The surface of the film is very rough due to the presence of the oxygen functional groups and sp^3 hybridized clusters. 41

Figure 5-2 AFM image of graphene oxide (GO-G) spin coated onto a glass substrate with an average roughness of 7.38 nm.The light spots on the image can be undissolved salts added during the oxidation process and dust particles. 41
Figure 5-3 Height profile for the graphene oxide (GO-G) deposited on a glass substrate with an average thickness of 18.75nm indicating a multi-layered sample. The thickness was calculated by taking a height profile of three different sheets edges as displayed on the right side of the image. 42
Figure 5-4 Height profiles for the reduced graphene (rGO-G) spin coated at 5500 rmps on a glass substrate with an average thickness of 7.95nm and average roughness of 1.99 nm. The removal of the epoxide and hydroxyl bonded below and above the carbon layer during reduction has resulted in an enormous decrease in the average roughness. 42
Figure 5-5 Reduced graphene oxide reference sample drop coated onto a $Si/Si0_2$ substrate with minimum thickness of 1.358 nm as determined from the cross section image on the right. 43
Figure 5-6 Cross section of reduced graphene oxide reference sample on $Si/Si0_2$ substrate with thickness of 1.141 nm measured on the "step" edge of two overlapping sheets..... 43
Figure 5-7 Reduced graphene oxide reference sample on $Si/Si0_2$ substrate with individual sheet thickness of 4 nm as measured from the cross section captured..... 44
Figure 5-8 Raman spectra for reduced GO for different number of graphene layers. Black, for a monolayer characterized by a single sharp D peak and red for multilayered sample as characterized by the two component D peak. 44
Figure 5-9 continuous Graphene film vacuum filtrated onto a track etch membrane consisting of multiple layers among monolayers. 45
Figure 5-10 3D and image results for 2 MeV proton irradiated graphite strip with an average roughness of 13.3 rms irradiated with a dose ranging from $5.9x10^{18}$ to $29.4x10^{19}$ ions/cm^2.The surface is profoundly rough due to the reduction of crystallite size during irradiation. 45
Figure 5-11 SEM images for GO-G(left) and rGO-G(right) spin coated on a glass substrate. GO-G consists of highly ordered stack of graphene oxide layers. 48
Figure 5-12 Reduced graphene oxide 10-15 nm thick (left) and 1-3 nm thick (right). The samples were deposited with an intention that they have different thickness but as mentioned earlier one of the shortcomings of chemical reduction is the aggregation of the layers due to the attraction force between the layers. 48
Figure 5-13 Reduced graphene oxide with undissolved salts decorating the sheets surface.The particles are charging as indicated by their brightness in the image as compared to the semi-conducting graphene sheets..... 49
Figure 5-14 Reduced graphene oxide sheets and zoomed Isolated reduced GO graphene oxide sheet deposited on FTO by drop coating, supporting the fact that the dilution level of the as-prepared solution is correlated to the number of deposited layers. 49
Figure 5-15 SEM image of rGO-P solution on glass drop coated once (left) and eleven times (right).When the number of layers coated on to the substrate increase the number of layers also increase. 50
Figure 5-16 SEM micrograph of graphene sheet on track etch membrane revealing the ununiform distribution of the pores on the membrane. 50
Figure 5-17 TEM image of onion shaped particles of carbon film deposited at RT. 52
Figure 5-18: TEM image of graphene oxide showing aggregation of sheets. 52
Figure 5-19 TEM of suspended graphene. Top GO and electron diffraction pattern , bottom left rGO and bottom right zoom rGO edge of two and three layers dominated by two and three dark lines respectively..... 53

Figure 5-20 Raman spectra of graphite, GO and reduced GO display a disorded D peak at 1359 cm^{-1} and a G peak at 1587 cm^{-1}, corresponding to the first-order scattering of the E_{2g} mode. 54
Figure 5-21 GO and rGO edge respectively. The reduction of GO does not affect the transmittance of an individual sheets but decreases that of multiple layers..... 57
Table 4 Summary of sample description..... 58
Figure 5-22 The edges of the sheets are unstable and therefore tend to fold and wrinkle. 58
Figure 5-23 Plot of transmittance % as a function of wavelength for graphene oxide and graphene in the Ultra-violent and Visible range. 59
Figure 5-24 Absorption spectra for different graphene films. Most of the films have the same band gap of 4.12 eV while that of the diluted reduced graphene is 3.97 eV .Nevertheless they are both above the maximum band gap energy for absorption of visible light. 60
Figure 5-25 Transmittance % plot as a function of wavenumber in cm^{-1} for the different chemically treated samples. 61
Figure 5-26 The transmission spectra for Graphene before and after annealing at 500 ^{0}C for 6 hr under a vacuum. The transmittance of the graphene film decreases with annealing due to further reduction of the film and increased number of free electrons. 62
Figure 5-27 The current and voltage characteristics of graphene as a function of temperature..... 64
Figure 5-28 Images of proton irradiated sheets ,(a) unirradiated sheet (b) to (g) spot 1 to spot 6 respectively. The bright areas of the images indicate the thicker regions in the image while the faded regions indicate the thinner regions in the sample. 67
Figure 5-29 Raman spectra of rGO-G films on Si/SiO_2 substrate irradiated with protons. The G^+ feature is associated with carbon atom vibrations along the nanotubes axis .The G^- feature is in contrast is associated with vibrations of carbon atoms along the circumferential direction of the SWNT.The splitting of the peaks indicate that the measurements were done at a folded edge. 68
Figure 5-30 Images of proton irradiated sheets ,(a) spot1 $1.79x10^{16}$ to (f) spot6 $1.07x10^{17}$ ions/cm^2 respectively. 69
Figure 5-31 Raman spectra of rGO-G films on Si/SiO_2 substrate irradiated with protons with a single sharp D peak confirming, with the visual inspection of the figure 5-31,that the measurements were done on monolayer's. 70
Figure 5-32 Plot of the ratio of the intensities of the D and G peaks as a function of the proton irradiation dose. The increase in the ratio from the unirradiated to the irradiated sample indicates a decrease in crystallite size of the irradiated sample..... 70
Figure 5-33 Images of UV irradiated sheets ,(a) boundary between irradiated and unirradiated the black portion is the area which was irradiated with a mask to focus the beam ,(c) spot 1 =19 keV to (f) spot 4= 24 keV respectively. 71
Figure 5-34 Raman spectra of rGO-G films on Si/SiO_2 substrate UV irradiated the G peak has also consists of two components as the proton irradiated graphene. 72
Figure 5-35 Raman spectra of rGO-G films on Si/SiO_2 substrate as a function of the incident power,There was no induced damage of the sheet at 05 mW but above there was visible damage as illustrated by the marks left behide by the beam. 73
Figure 5-36 Raman spectra of rGO-G films on Si/SiO_2 substrate as a function of the incident power from 5 to 40 mW irradiated with visible (green) light. .. 73
Figure 5-37 D and G peak intensity ration as a function of the incident power. The net motion of the ratio is a decrease but there is no major change. 74

CHAPTER 1

1.1 Introduction

The ever-increasing population of the world resulted in high demands for both renewable and non-renewable resources. Due to the increase in the standard of living, power, or more specifically electricity, has become one of the requisites for everyday living; unfortunately for us fossil fuel resources are non-renewable and the oil prices are continuously increasing. The next best option is nuclear power because it is more efficient, yielding maximum output power with minimum input fuel. It is stable, reliable and environmentally friendly, but like most new ideas it has advantages and disadvantages. One of the most prominent concerns and inhibiter of development is safety, due to past disasters (core melt accident at the Chernobyl nuclear reactor in Russia in 1986) and the scale of damages, which have since been researched, leading to the development of preventive measures. Graphite is used as one of the protective surfaces of the fuel pebbles for the Pebble Bed Modular Reactor. Other surfaces are also made of carbon derivatives. While graphite has been studied extensively, less work has been done on graphene. Graphene is a nano-form of graphite and it is important to do research on it also. The fuel sphere is 60 mm in diameter consisting of a 0.5 mm diameter uranium oxide core as illustrated in Figure 1.1 below, which radiates both particles and photons[1]. The research reported in this work concentrates mainly on the effects of photon and proton radiation of the mono-layer of carbon atoms in an attempt to improve the safety of fission reactors. It is also important to study the radiation damage in terms of practical aspects because low energy electrons and photons are often used in analytical and lithographic tools.

Low cost of production, mass production, abundance of source material, quality performance with minimum power requirement, heat dissipation, controllability of properties, efficiency, reliability and stability of materials and most importantly multi-functionality or applicability of material, are the concepts that come to mind when someone mentions "new material". Graphene has been studied for years but was only truly discovered in 2004. Among its properties are high electrical conductivity and high optical transparency, making it a candidate for transparent conducting electrodes required for applications such as touch screens, liquid crystal displays, organic photovoltaic cells (OPV's) and organic light emitting diodes. In particular, graphene's mechanical strength and flexibility are

advantageous compared to indium-tin oxide, which is brittle and graphene films may be deposited from a solution over large areas. At present, indium-tin oxide (ITO) is the state-of-the-art material for transparent and conducting hole collecting electrodes, with transparency of > 90% at 550 nm and low sheet resistance of (10–30) $X10^2$ Ω/m. However, ITO cracks upon flexing, thus, to move toward truly flexible OPV's, alternatives to ITO and Al electrodes are needed. The use of solution-deposited single-walled carbon nanotube thin films as cathodes in OPVs has been demonstrated in previous work. Transparent and conducting thin films from thermal reduction of graphene oxide (GO) with sheet resistance as low as $600X10^2$ Ω/m and with transparency of 60% at 1100 °C in a Ar/H_2 atmosphere have been previously reported and demonstrated to be suitable as electrodes for dye sensitized solar cells by Goki Eda *et al.* APL92 2008 (see Figure 1.2) .

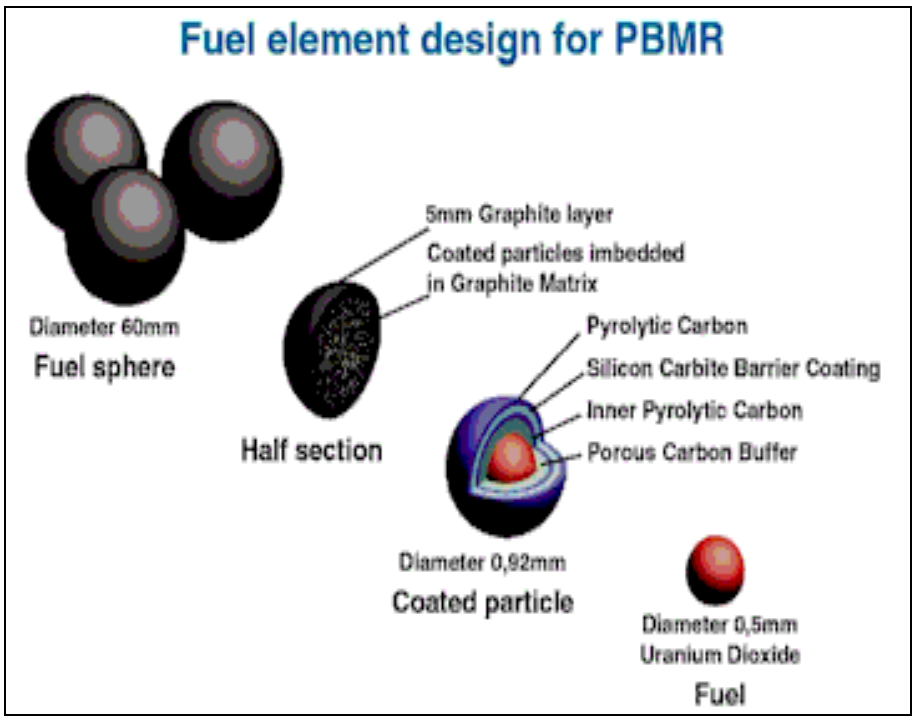

Figure 1-1 Fuel element design for the PBMR with cross section of the pebble showing the layers of coatings [scienceinafrica2009]

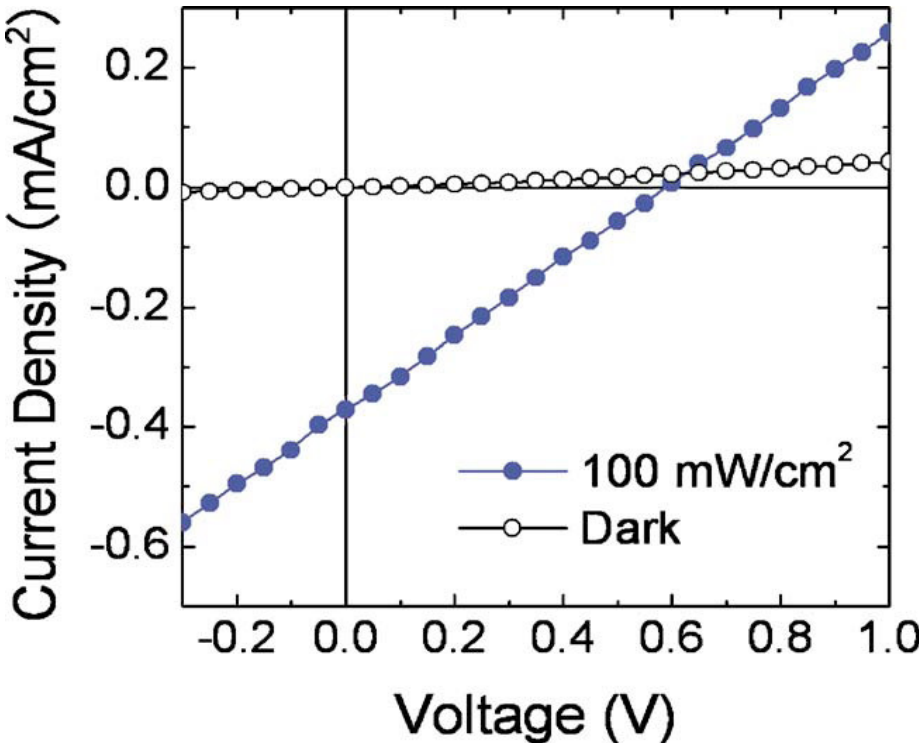

Figure 1-2 Solar cell characteristics of an OPV with a reduced GO thin film as the transparent electrode measured in the dark and under illumination [Goki Eda *et al.*APL92 2008].

1.2 Historical survey

In the late 1930s Landau and Peierls argued that Graphene, a monolayer of graphite with a minimum thickness of about 0.34 nm, could not exist, because of its 2D atomic crystal arrangement. Their arguments were based on the theory that the melting temperature of thin films rapidly decreases with decreasing thickness and would become unstable. Single layers of graphite were grown epitaxially on mono-crystals with similar crystal lattices, but there was significant charge transfer from the substrate to the epitaxial graphene and in some cases hybridization between the d-orbitals of the substrate atoms and π-orbitals of graphene, to considerably change the electronic structure of the graphene. In contrast with past ideas it was found to be stable and free standing, not destroyed by thermal fluctuations. There has been number of efforts to make very thin films of graphite by mechanical exfoliation starting from the 1990 but nothing thinner than 50 to 100 layers were produced. The first paper on graphene was published in October 2004, entitled "Electric field effect in atomically thin carbon films" by Andre Geim and Kostya Novoselov at the Manchester University who managed to extract single atom layer crystallites from bulk graphite. Andre Geim had the idea of polishing down a graphite block to just 10 or 100 layers thickness and then to study the material's properties. One of his students was assigned the task and consequently produced a speck of graphite roughly 1000 layers thick. Geim then had the idea to use Scotch tape to peel away the top layer. Flakes of graphite came off onto the tape and the process could be repeated several times to achieve progressively thinner flakes attached to the tape. He then dissolved the tape in solution, leaving him with ultra-thin flakes of graphite: just 10 layers thick. Within weeks, his team had begun fabricating rudimentary transistors with the material. Subsequent refinements of the technique finally yielded the first graphene sheets. (The history of the Andre Geim and Kostya Novoselov discovery was reported on the American Physics Society website on 22 October 2009). Graphene is visible by means of an optical microscope if placed on top of a Si wafer with specific thickness of SiO_2. If the SiO_2 is any thicker then 300 nm it becomes invisible. Graphene has contributed to the development of high energy physics, and the previously unobservable can now be observed [2,3]. Its unique properties result from its honeycomb lattice structure. The geometry is due to the hybridized sp^2 orbitals. These hybridized orbitals form directional sigma bonds with neighbouring carbon atoms leading to the hexagonal geometry with lattice parameter a = 24.6 nm. The free delocalized

electron is oriented perpendicular to this plane [4,5,6]. It can be used to describe properties of various carbon-based materials and provide a condensed-matter analogue of 2D quantum electronics. Due to interactions between the electrons and the periodic potential of the lattice, electronic properties are described by the Dirac equation instead of the Schrödinger equation, because the charge carriers are massless and travel at a speed close to the speed of light (10^6 m.s^{-1}) [3,7,8]. Graphene exhibits unusual transport and electrodynamics properties due to its linear dispersion of charge carries [9,10,11] .

The methods for obtaining individual graphene sheets have progressed, from ripping it with adhesive tape or gently pushing small graphite crystals along a hard surface, to oxidation of graphite using the Hummers method [12]. The modified Hummers method requires first the oxidation of graphite to synthesize graphene oxide (GO). Secondly, exfoliation of the as-prepared GO has to be performed to obtain thermally expended GO (TEGO). Finally, the TEGO is reduced to produce graphene. The type of graphite that is used influences the number of graphene layers produced. Graphite with small lateral size yields single layers of graphene [13].

1.3 Aim and Motivation of Investigation

1.3.1 Aim of the Project

The aim of the project was to synthesize single and multiple layers of graphene by chemical exfoliation of graphite. Then to investigate the optical and structural changes as graphene oxide was chemically reduced to produce graphene. Finally to study the effects of photon and proton irradiation on the physical and structural properties of graphene.

1.3.2 Project objectives

The main objective of the project was to synthesize graphene oxide using the Hummers method, which involved the chemical oxidation of graphite followed by a purification process, to remove the undissolved salts and large graphene oxide flakes. The graphene oxide produced in this way was then chemically reduced to graphene, by adding hydrazine (a strong reducing agent). The graphene oxide and graphene solutions were then deposited onto various substrates depending on the type of characterization to be done, using various deposition methods. A vapour deposition system was used to produce the 300 nm thick silicon dioxide substrate. Fluorine-tin oxide coated glass substrates were used to study the morphology of single and multilayered sheets, with the aid of the scanning electron microscope and the atomic force microscope. The latter was also used to determine the sheet thickness as well as the surface topography. The solutions were deposited on electron-microscopy copper grids, for performing the high resolution transmission electron microscopy and for obtaining the electron diffraction patterns. In this latter part, selected area diffraction was done to determine the crystalline structure of the sheets at different spots, such as at the edge and at the centre of single and multilayered sheets. Raman spectroscopy measurements were done to determine the number of layers and bonding structure of the films. Use was made of the fact that different numbers of layers give a specific spectrum. Glass substrates were used for studying the optical properties, using UV-Visible spectroscopy to determine the transmittance percent of the thin films. Silicon dioxide substrates with silver electrodes were used for

the transport measurements of the samples. Finally the samples were irradiated with green light, ultra-violet light and protons after which RAMAN measurements were done to determine if structural changes had occurred during the irradiation and how much the change were influenced by the dose of radiation.

1.3.3 Benefits of the research

Since graphene is a new material and information about it is limited, this research contributed to the data about this unique material. The basic building block of carbon based material was researched, and the results may help to explain bulk behaviour and deviations. Graphene exhibits unique properties which include high thermal conductivity, with values ranging from 4.84×10^3 $W.m^{-1}.K^{-1}$ to 5.30×10^3 $W.m^{-1}.K^{-1}$ and electron mobility of 1.500×10^5 $mm.V^{-1}.s^{-1}$. The high thermal conductivity makes it an ideal candidate for the Pebble Bed Modular Reactor (PBMR) coating applications to keep the core cool and prevent disasters such as that which happened in 1986 in Russia. A study of graphene can assist in the risk assessment of the nuclear power industry and eliminate the safety concerns about the use of nuclear energy. Another remarkable property of graphene and graphene oxide is their optical-transport coupled behaviour, which is important for transparent conducting-oxide type applications.

1.3.4 Scope of investigation

Chapter 1 is an overview of the history and progress of grapheme. It also presents the aim and motivation for this research. Chapter 2 is a literature review, first comparing the properties of a few carbon allotropes and then discussing the different properties of graphene. It also gives an overview of the effects of radiation on graphite, growth methods of graphene and finally graphene applications. Chapter 3 describes the characterization techniques on which the analysis of the results will be based. Chapter 4 gives the procedures used to synthesize graphene from graphite. Also to reduce graphene oxide to graphene otherwise stated as reduced graphene oxide. In Chapter 5 the experimental results are presented and discussed. The conclusion and references cited in this work are given in Chapter 6.

CHAPTER 2

2.1 Literature Review

2.1.1 Properties of graphene

The element carbon has many allotropes including graphite, diamond and diamond-like carbon. They have the same basic building block, the carbon atom, but different crystalline forms. The properties of the various carbon allotropes can vary widely. For instance, diamond is by far the hardest known material, while graphite can be one of the softest. Diamond is transparent to the visible spectrum, while graphite is opaque; diamond is a semi-conductor while graphite is a conductor. DLC is a combination microcrystalline diamond and graphite produced by low-pressure synthesis. The carbon phase diagram is shown in Figure 2-1. Carbon vaporizes at 4800 K at a pressure of 1000 atmospheres, conditions under which diamond is stable. The high-pressure conversion of diamond from graphite occurs at temperatures of approximately 3000 K and pressures above 125 kilo bars. DLC converts to graphite at lower temperature than diamond. An initial transformation has been observed at a temperature as low as 250 °C. The transformation is rapid at 400 °C and proceeds by loss of hydrogen and subsequent graphitization. A maximum temperature for the long term use of DLC is 250 – 300 °C. Graphene layers have a high thermal conductivity, mechanical stiffness and electronic transport that rival the remarkable in-plane, like-properties of bulk graphite[2]. These layers are also electrically conductive with a minimum value of e^2/h instead of the theoretical value of $4e^2/h\pi$, (missing pie theory)[3]. The carbon atoms are covalently bonded with bond length of 14.2 nm to three others. However, carbon has 4 valence electrons. Therefore it has delocalized electrons in ∏-bonds, contributing to its conductivity [4,5,6,14] .

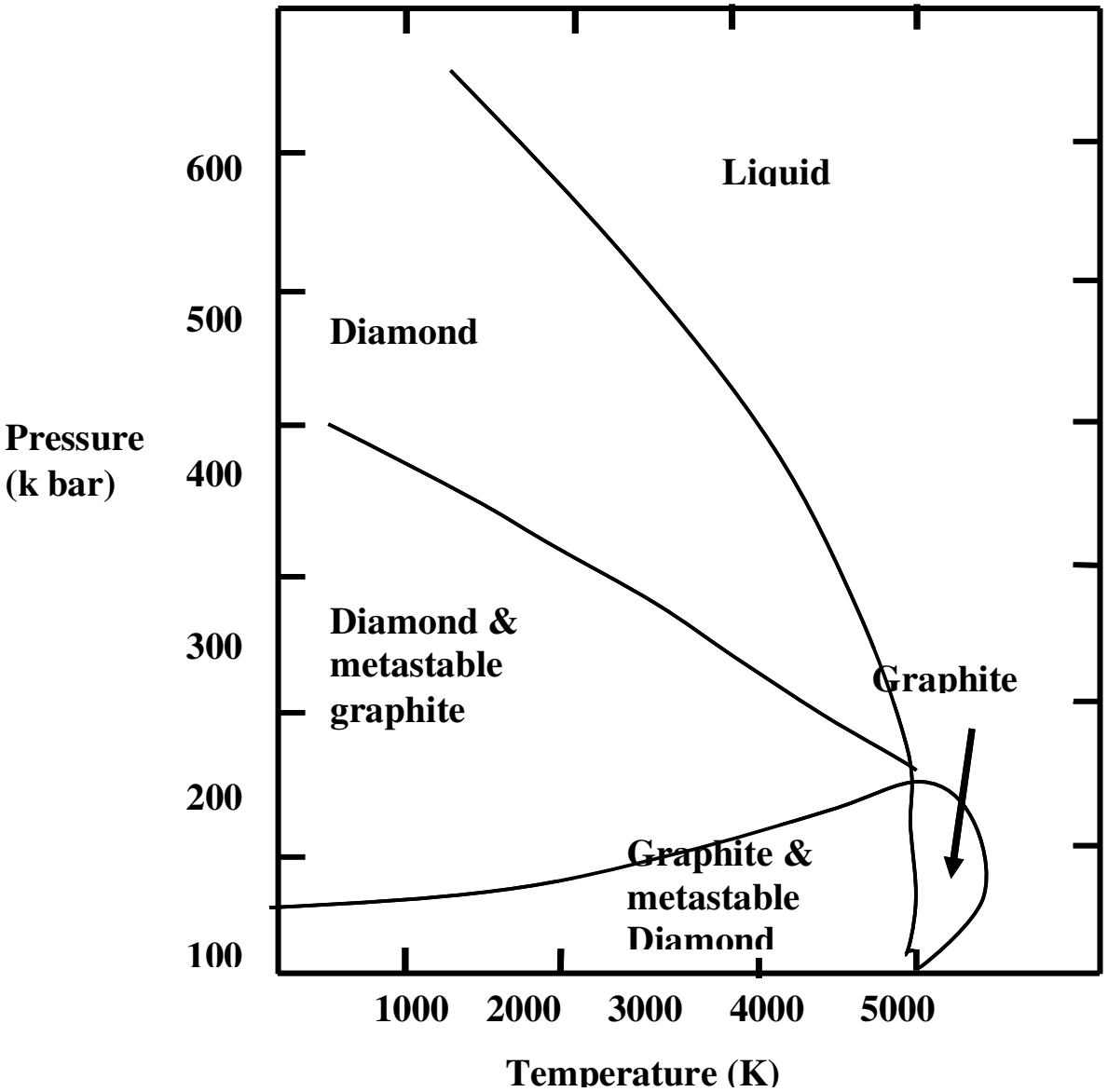

Figure 2-1 Carbon phase diagram [6]

Table 1 Table of comparison for graphite, diamond and diamond-like carbon properties

Property	Graphite	Diamond	Diamond-like carbon
Composition	Pure carbon	<1 at% hydrogen	≤50 at% hydrogen
Microstructure	crystalline	crystalline	amorphous
Atom bonding state	Sp^2	Sp^3	Sp^3 Sp^2 Sp^1
Bond energy (kJ/mole)	680	370	
Stability	Stable	Stable	Metastable
Electrical conductivity	Conductor	Insulator	Insulator
Resistivity (Ω. cm)	$3x10^{-11}$ *c* 2.2 - $5x10^{-8}$ *ab*	10^{12}-10^{16}	10^{5}-10^{15}
Band gap (eV)	-0.04	5.48	0.8-3
Thermal conductivity (W/ cm. K)	398 *c* 2.2 *ab*	> 1300	400 - 1000
Density (g/cm^3)	2.26	3.515	1.8 - 2.8
Index of refraction	2.6	2.4	1.8-2.4
Raman spectrum (cm^{-1})	Sharp peak @1580	Sharp peak @1352	Broad humps @ 1330 and 1550

2.1.2 Structural properties

Graphene has a two-dimensional hexagonal atomic structure, made up of individual atomic planes, one atom thick with a lattice parameter of 0.246 nm and is black in colour. It consists of hexagonal sp^2 bonded C atoms made of benzene rings, stripped of H atoms. Each atom is connected to three nearest neighbours, within the sheets, by covalent bonds that separate them by a distance of 14.15 nm. This bonding arrangement results from the sp^2 hybridization of carbon's electronic orbital. Within the graphite sheets the distributed pi-bonding exists between the carbon atoms and this gives rise to delocalized electrons, making graphene electrically conducting [6]. The schematic of the bond structure is as shown below in Figure 2.2.

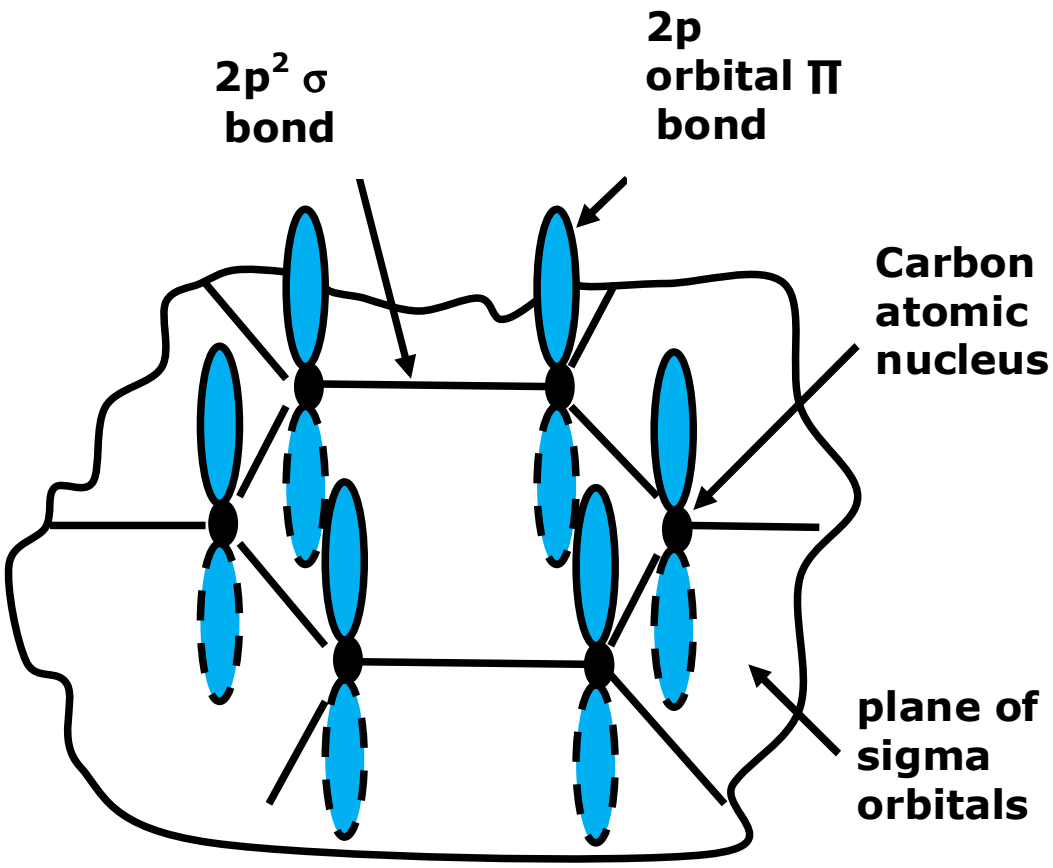

Figure 2.2 Schematic of the sp^2 hybridized structure of graphene showing the sigma bonds and the 2p free electrons (above and below the sigma orbit & plane) [6]

2.1.3 Mechanical properties

An atomic force microscope can be used to measure the mechanical properties of suspended graphene, produced by exfoliating thin layers of graphite over photo-lithographically defined trenches in silicon dioxide films on a silicon substrate. By pressing with a calibrated spring constant in the Atomic Force Microscope the spring constant of the sheets can be derived. By drawing a graph of the force exerted on the tip versus the displacement of the graphene sheets and making use of Hooke's law, the effective spring constant can be determined. Values of 1-5 N/m for sheet thickness from 2 to 8 nm were found. Fitting to the model of a doubly clamped beam in equilibrium with a static force and under axial tension, a value for Young's modulus of 0.5 TPa can be derived [15].

2.1.4 Thermal conductivity

With the continuously decreasing size of electronic devices and increasing dissipation power density in downscaled circuits, there is a notable growth in the importance of materials that can conduct heat efficiently and once again graphene outperforms the rest of the carbon based nano-materials, with a thermal conductivity range of $(4.84 \pm 0.44) \times 10^3$ to $(5.30 \pm 0.48) \times 10^3$ $W.m^{-1}.K^{-1}$ compared to the values of 3000 $W.m^{-1}.K^{-1}$ and 3500 $W.m^{-1}.K^{-1}$ for Multi-Walled Carbon Nanotubes (MW-CNT) and Single-Walled Carbon Nanotubes (SW-CNT) respectively. The non-contact confocal micro-Raman spectroscopy can be used to measure the thermal conductivity, by determining the dependence of the Raman G peak frequency on the excitation laser power. Graphene, having high thermal conductivity, does not meet the requirements for conventional methods. The 3w "laser-flash" method, for instance, requires a substantial temperature drop over the thickness of the examined film and the thermal bridge is technologically very challenging [16].

2.1.5 Electronic-conductivity properties

The electronic properties of materials are commonly described in terms of quasi-particles. The characteristics of Dirac fermions in graphene are described as follows: Graphene can be distinguished from ordinary metal by the Hall effect. The integer quantum Hall effect (QHE) in graphene occurs at a half-inter filling

factor due to invoked coupling between pseudo spin and orbital motion, resulting in a π-shift in the phase of the quantum oscillations. Graphically the quantum Hall effect of graphene has a ladder of equidistant steps in the Hall conductivity through the neutrality (Dirac) point (where the charge carries change from electrons to holes)[7]**.** Annealing graphene based devices in a vacuum, shift the peak to zero voltages. Exposing it to water vapour or NH_3 leads to p- and n-doping respectively. Graphene properties can be controlled by the application of the electric field, unlike most thin films which are unstable. Its behaviour resembles that of the ambipolar field effect in semiconductors but there is no zero conductance region associated with the Fermi level. The reason is that it is pinned inside the band gap. Up to date no metal or semi-metal (excluding grapheme) has been shown to exhibit a noticeable field effect, and thereby creating an obstacle to metallic electronics [17].

Graphene has an ambipolar electric field such that charge carriers can be tuned continuously between electrons and holes in concentrations n as high as 10^{13} cm^{-2}. Their mobility μ can exceed 15,000 $cm^2.V^{-1}.s^{-1}$, even under ambient conditions [3]. Resistivity and conductivity are quantized, rather than resistance and conductance. Conductivity never falls below a minimum value corresponding to the conductive quantum e^2/h, even when the carrier concentration tends to zero. Normally such low conductivity leads to a metal-insulator transition at low temperatures but no sign of the transition has been observed in graphene down to liquid-helium temperature. The conductance can be enhanced by p-type doping of grapheme. This is done by dipping the film in thionly-chloride ($SOCl_2$) for an hour. Hall resistivity is quantized to discrete values of h/he^2. Unlike in metals the QHE is observed at low temperatures because the magnetic energy of electrons is 1000 times greater. The electrical resistance is independent of the number of impurities and therefore the material can be used as high-speed electronic switching devices (ballistic transistors) [7,14,18].

2.1.6 Photo-electric properties

Dirac fermions carry one unit of electric charge and can be manipulated by an electromagnetic field. Photo-electrons are emitted from matter after the absorption of energy from electro-magnetic (EM) radiation, if the radiation frequency is above the threshold frequency specific to that type of surface material. The Schrödinger equation is used to calculate the photo-electric effect in two layers of graphite. The intensity of the classical photo-electric effect is peaked

in the direction of the electric vector of the wave. The ballistic interaction of photons with electrons is not possible in a vacuum for point-like electrons; it is only possible in a medium and there are also no excited states of electrons in vacuum. At room temperature the radiation is unstable and therefore the photo-electric effect can only be realized by very short laser pulses. Deformed graphene is influenced by the gravitational field which results in a modification of the photo-electric effect [19]. When graphene is exposed to an electromagnetic field the carriers acquire a mass of approximately 10^{-4} m_e. The particles are no longer massless due to the gap opening [20].

2.1.7 Electromagnetic properties

An isolated graphene layer can be used as a simple tuneable frequency multiplier with operating frequency variable in a broad range, from microwaves to infrared. When a graphene layer is irradiated with an electromagnetic wave with frequency Ω it re-emits radiation at higher harmonics $m\Omega$, where m is an odd integer. Normal 2D systems have a parabolic energy dispersion i.e. the velocity V_x and current j_x are proportional to the momentum p and therefore responds at the same frequency. In graphene the velocity is a non linear function of p_x and therefore has an unharmonic response [9,21].

Graphene/polymer composites can be used commercially as effective and lightweight shielding materials for electromagnetic radiation. These composites show a low percolation threshold of 0.52 vol. %. The highest EMI SE of the composites containing 15 wt % (8.8 vol. %) SPFG is measured at 21 dB in the X-band (8.2-12.4 Hz) when the target value of the EMI SE needed for commercial applications is around 20 dB [10].

Measurements on irradiated graphite reveal large strains growth parallel to the c-axis and contractions within the basal planes. Irradiation produces interstitial and vacancy defects (Frenkel pairs). These defects form strong covalent bridges between atomic layers and provide conduction paths in this direction, lowering the resistivity. Cross-linking interstitials pin the dislocation motion [22]. Vacancies produced by irradiation are stabilized by creating pentagon-heptagon defects and at the same time pushing one carbon atom out of the graphene plane. Electronic excitations are solely responsible for the defects formation [23].

Irradiation damage is prominent in rolled up graphene sheets but not in planar sheets. It was found that 20 eV photons are more destructive than higher energy

photons because a larger area can be irradiated easily. The low energy damage can be recovered by annealing in a vacuum or argon atmosphere.

2.1.8 Influence of particle irradiation on graphite properties

Not much work has been done on the effect of electromagnetic irradiations on the properties of either graphene nor graphene oxide. That is why the effects of particle irradiation have been presented in the previous paragraph. According to the literature review the changes in the properties are due to the lattice displacement and not due to the implanted species. Therefore the expected changes can be used as a guide for electromagnetic irradiation investigations. The sp^2 to sp^3 transition of carbon atoms can be easily recovered through annealing of the lightly irradiated samples, provided that the samples are kept far below the graphitization temperature. However, the high dose irradiated samples form Sp^3 clusters which are harder to anneal out. The sp^2 to sp^3 transition influences the properties of graphene by reducing its thermal conductivity and increasing its electrical resistivity, hydrogen retention and dimensional change. Reduction of thermal conductivity and increase of hydrogen retention make the life-time of first-wall graphite very short, which affects its use in nuclear reactors. Once graphene loses its 2D structure the recovery to its initial structure is difficult because the basal planes lose their ordering and this leads to breaks and bends in the lattice[24]. Recently, ferromagnetism in ion-irradiated carbon materials has been attracting much attention. The radiation treatment of carbon materials, apart from its applications in the nuclear industry, is a versatile tool for manipulating the physical and the chemical properties of carbon materials. Phase transformation of graphite to diamond-like carbon and graphitization of nano-diamonds by ion irradiation have been reported. Most interesting is the ferromagnetism observed in proton-irradiated highly oriented pyrolytic graphite (HOPG), for which many theoretical and experimental studies have been done. Still, the origin of ferromagnetism in proton-irradiated graphite remains unclear. On one hand an electron spin resonance study has shown that the localized spins produced by the proton irradiation do not interact with the spins of charge carriers, suggesting a direct (unmediated) interaction between the localized spins as an origin of the ferromagnetism in proton-irradiated HOPG. On the other hand, an X-ray magnetic circular dichroism study has suggested that spin polarization of the delocalized π-electrons is responsible for the ferromagnetism in proton-

irradiated carbon. Furthermore, an X-ray photoelectron spectroscopy (XPS) study on proton-irradiated polycrystalline graphite showed an increase of sp^3 hybridization, suggesting a possibility that mixed hybridization of sp^2 and sp^3 is responsible for the Ferro-carbons [25,26].

2.1.9 Graphene sheets applications

The low production cost makes graphene-based composite materials attractive for a variety of uses but it is doubtful that it will be able to match the mechanical strength of the nanotubes. For instance, graphene powder of micron-size crystallites can now be mass produced for use as filler in conductive plastics and in electric batteries, instead of nano-fibers, because of its large surface-to-volume ratio and high conductivity. Graphene is capable of absorbing large amounts of hydrogen, so that can be used for hydrogen storage. Gas molecules measurably affect the electronic properties of grapheme. Consequently it can be used for producing gas sensors which are sensitive to a single atom or molecule. As it is very thin, it may be used for supporting micro- and nanoscopic objects as support membranes for transmission electron microscopy. It would not interfere with the image and because of its very simple crystal structure it's contribution can easily be eliminated from diffraction patterns if used as the substrate. Graphene is resistant to attack by many powerful acids and alkalis such as hydrofluoric acid and ammonia and can act as an inert and thin protective coating. Graphene can be used as transistors, because graphene is so thin that it's conductive state can be controlled by the application of an electrical field, unlike the case of other competitive metals. It can also be assembled into paper-like material consisting of interlocked graphene oxide sheets due to its high mechanical stiffness caused by the lack of boundaries [2,7]. After oxidation the graphene can be introduced with hydrophilic groups and can be well-dispersed in an aqueous solution for delivery of water-insoluble drugs. While carbon nanotubes load drugs via surface and tips and form bundles when used, graphene loads the drugs via its two faces and edges [27]. Graphene can also be used as a thermal management material, in optoelectronics, photonics and bioengineering, because of its high thermal conductivity. This is also the reason for the integration of graphene with nanometre-scale silicon in complementary metal-oxide semiconductors (CMOS) [20]. Despite its usefulness there are still challenges to be overcome, including high quality wafer production and in controlling individual features for reproducibility. The transmission probability of electrons in graphene may be

largely independent of the potential barrier height and width, resulting in the conductivity not being influenced by the gate voltage. This makes it suitable for application in FET.

2.1.10 Methods for producing graphene sheets

2.1.10.1 Mechanical exfoliation of graphite

This is the simplest method for obtaining graphene sheets from bulk graphite. Graphene is repeatedly pealed from highly oriented pyrolytic graphite, using cellophane tape, and deposited onto a silicon substrate. Mechanical exfoliation of 3D graphite crystals to study the electrical properties of thin graphite films led to the accidental discovery of graphene because purely 2D crystals were unknown and presumed not to exist. The disadvantages of using this method is that yields from this method are extremely low and involve searching the substrate for single sheets among a multitude of multilayered flakes [28].

2.1.10.2 Epitaxial growth

Graphene may be obtained by heating silicon carbide to high temperatures (1100 °C), but the size of the grown sample is dependent on the SiC substrate used. The face of the SiC used for graphene growth highly influences the thickness, mobility and carrier density of the graphene [29] .

2.1.10.3 Exfoliation-re-intercalation expansion of graphite

Commercial expandable graphite is exfoliated by brief (60 s) heating to 1000 °C in a forming gas. The exfoliated graphite is then grounded, re-intercalated with oleum (fuming sulfuric acid with 20% free SO_3), and then tetrabutylammonium hydroxide (TBA, 40% solution in water) is inserted into oleum-intercalated graphite in N, N-dimethylformamide. The TBA-inserted 3 oleum-intercalated graphite is sonificated in a dimethylformamide solution of 1,2-distearoyl-sn-

glycero-3-phosphoethanolamine-N-[methoxy(polyethyleneglycol)-5000](DSPE-mPEG) for 60 minutes to form a homogeneous suspension. Centrifugation is used to remove large pieces of material from the supernatant i.e. allow them to settle at the bottom of the suspension. This method easily obtains large amounts of graphene sheets suspended in DMF and these sheets could be transferred to other liquids, including water and organic solvents [30].

2.1.10.4 Oxidation of graphite (Hummers method)

Graphite is subjected to an oxidative treatment with potassium permanganate ($KMnO_4$) in concentrated sulphuric acid. The graphite (2 g) is placed into a round bottom flask. Concentrated sulphuric acid (46 ml) is added and the mixture is cooled in an ice bath. Potassium permanganate is then added to the ice-cooled mixture in small portions over 30 minutes. Following this addition, the reaction mixture is stirred at 35 degrees C for 2 hours. After the two hour period, water (92 ml) is added and stirring is continued for 15 minutes. Finally, the mixture is poured into 270 ml of water and the excess of potassium permanganate is neutralized by adding a sufficient amount of water solution (30%) of hydrogen peroxide. Graphite oxide is recovered by filtration. The filtered graphite oxide is washed with an HCl solution (10:1 water:concentrated HCl) until sulphates are no longer detected by a barium chloride test. The graphite oxide is then dried under vacuum for 24 hours [31].

The disadvantage of this method is that the GO sheets are decorated by epoxide and hydroxyl below and above each carbon layer with carbonyl and carboxyl bonding at the edges. These covalently attached oxygen functionalities alter the Van De Wall interactions between the GO layers. A cross-sectional step height of more than 1 nm is often observed for a single sheet, which is larger than the theoretical values and is detrimental to the electrical properties.

The GO then needs to be reduced using dimethyl-hydrazine as the reducing agent, to remove the oxygen functional groups [32]. Reduction in the solution stage causes the sheets to aggregate due to the attractive force between layers and decrease hydrophilicity, resulting in many of the sheets to be wrinkled or folded when examined by an atomic force microscope (AFM). Aqueous dispersions also aggregate during the evaporation process, during deposition and during the drying of the sample.

2.1.10.5 Reduction methods

The method involves first the immersion of the solid-supported sheets in a 1 volume % hydrazine solution in dimethyl-formamide (DMF) at 80 °C for 24 h. Then the samples are exposed to a hydrogen plasma (30 W at a pressure of 0.8 mbar) for 5-10 s at room temperature [28]. Finally the graphite oxide is transferred into argon, and rapidly heated to 1050 ^{0} C [33]

Hydrazine reacts with oxygen slowly but the kinetics of the reaction increases as the temperature increases. At low temperatures it does not rapidly decompose to ammonia unless an active surface or ionic impurity catalyses the decomposition [34].

The reaction is given by:

(a) In the presence of oxygen,

$N_2H_4 + O_2$ ----------> $2H_2O + N_2$

(b) At high temperature or in the presence of catalysts:

$3N_2H_4$ ----------> $N_2 + 4NH_3$

CHAPTER 3

3.1 Characterization techniques

3.1.1 Atomic Force Microscopy (AFM)

The atomic force microscope is a type of scanning probe for topographic imaging having atomic level resolution through the utilization of a mechanical probe. The advantages over the transmission electron microscope (TEM) is that it can image any type of surface unlike the latter which requires the surface to be either conducting or semi-conducting. It also allows for height and 3D surface profiling and surface roughness estimations. With the first scanning probe microscope, the scanning tunneling microscope (STM), it became possible to look into the fascinating world of atoms. The STM was developed by Gerd Binnig and Heinrich Rohrer in the early 80's at the IBM research laboratory in Switzerland. However, the STM technique is also restricted to electrically conducting surfaces. An extension of this technique, called Atomic Force Microscopy (AFM), was developed by G. Binnig, C. Quate and C. Gerber. The AFM also allowed insulating materials to be analyzed. The AFM and STM techniques do not require optical focusing elements. Instead, a small sharp probing tip is scanned very closely across the sample surface. The distance between the tip and the sample surface is so small that atomic-range forces act between them. In an AFM, a tip is attached to the end of a cantilever in order to measure these forces. The force acting on the tip can then be determined by detecting the deflection of this cantilever. The measurement of the cantilever deflection can be used to control the tip–surface distance on an atomic scale. Thus, high resolution can be achieved, so that even the atomic arrangement of surfaces can be probed. This measurement is called a static operating mode, in which the static deflection of the cantilever is used. Generally, the forces acting on the tip will cause it to snap onto the sample, which will result in an effective nanometre-range flattening of the tip, and friction between the tip and the sample. To eliminate the aforementioned problems, the dynamic force microscopy modes may be used. In this mode, the cantilever vibrates during the operation. In the dynamic modes, changes in the free resonance frequency and the damping of the cantilever vibration caused by the

forces between the tip and the cantilever can be measured and used to regulate the tip–sample distance. To achieve atomic resolution, ultra-clean and flat surfaces prepared in highly sophisticated vacuum systems are needed. Nevertheless, measurements in air can give useful results for many technically relevant surfaces. An image of the surface is made by scanning over the sample surface in the X and Y directions. The sample structure image is obtained by recording the output of the height control loop as a function of the tip position [35,36,37].

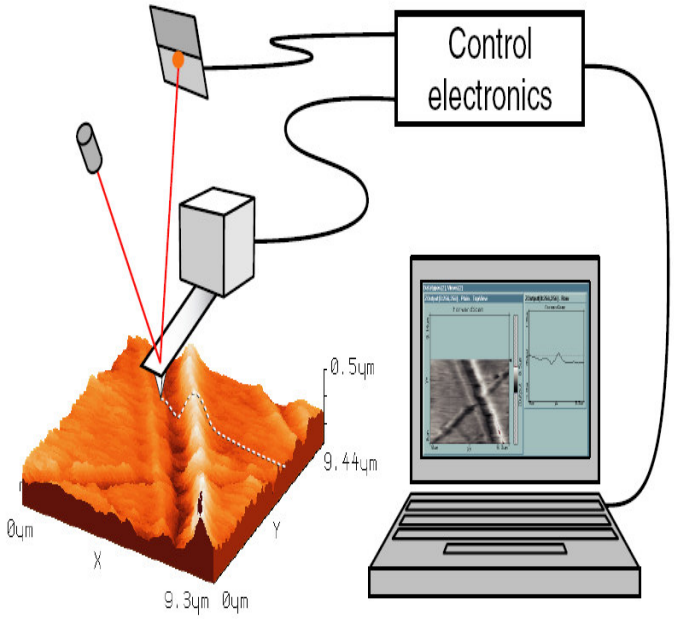

Figure 3-1 Cantilever with deflection detection system scanning the sample. The sample image is displayed on a computer with installed scan software which directs the scan itself [36].

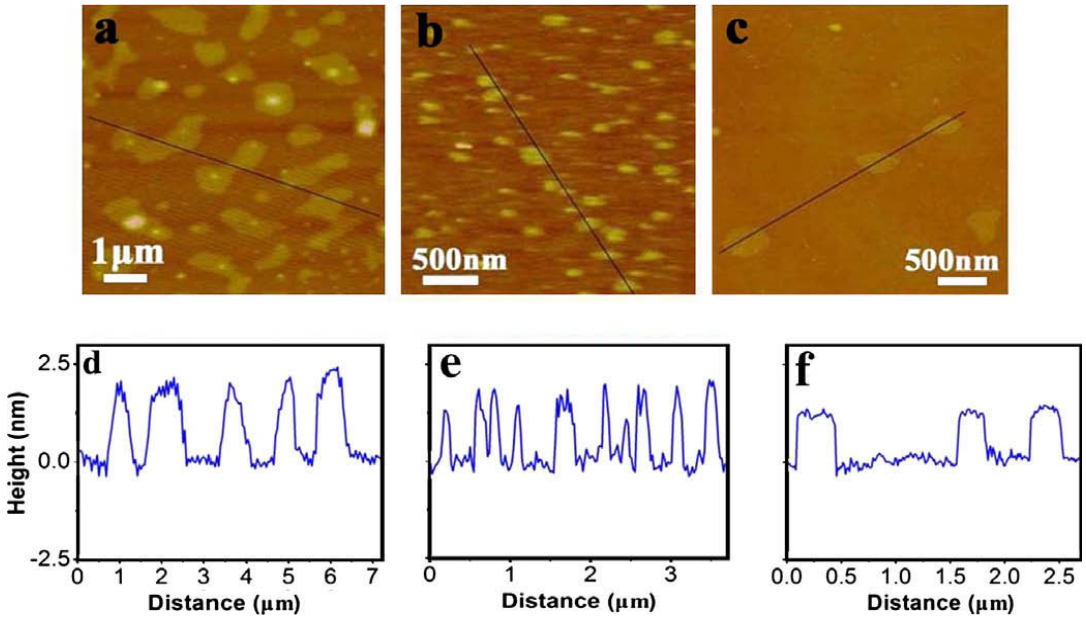

Figure 3-2 Typical AFM images and the corresponding height profiles of the graphene. The thicknesses of the graphenes are 1.9–2.3 nm, 1.3–2.1 nm, and 1.1–1.3 nm, respectively [13]. The pronounced roughness is attributed by sp^3 centres and point defects in the carbon lattice that cause wrinkling of the sheets [39].

3.1.2 Scanning Electron Microscopy (SEM)

The scanning electron microscope reveals information about the morphology, chemical composition, electrical conductivity and crystalline structure of the samples by scanning the surface with a high energy beam of electrons. As compared to the AFM, the SEM scans images much faster and has a very large depth of field which yields a characteristic 3D appearance of the surface structure, although it is actually a 2D image. The absence of charging during SEM indicates that the networks of graphene-based sheets are electrically conductive. The electron gun produces a stream of monochromatic electrons. The stream is "condensed" by the first condenser lens. This lens is used to both form the beam and limit the amount of current in the beam. The beam is also constricted by the condenser aperture, eliminating some large-angle electrons. The second condenser lens forms the electrons into a thin, tight, coherent beam. A user selectable objective aperture further eliminates large-angle electrons from the beam. A set of coils then "scans" or "sweeps" the beam in a grid fashion, dwelling on points for a period of time determined by the scan speed (usually in the microsecond range). The final lens, the "objective", focuses the scanning beam onto the part of the specimen desired. When the beam strikes the sample (and dwells for a few microseconds) interactions occur in the sample and are detected by means of various instruments.

Before the beam moves to its next dwell point these instruments count the number of interactions and display a pixel on a CRT whose intensity is determined by this number (the more reactions the brighter the pixel). This process is repeated until the grid scan is finished and then repeated. The entire pattern can be scanned 30 times per second [35,38] .

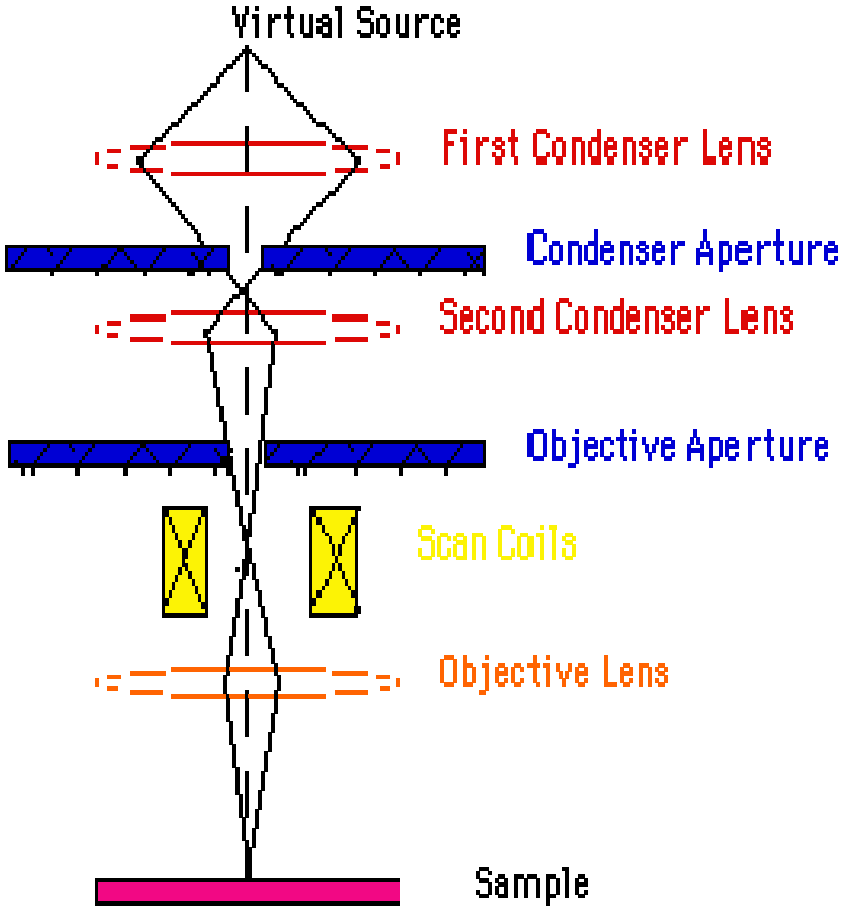

Figure 3-3 Diagram of electron beam path in a SEM (courtesy of unl.edu)

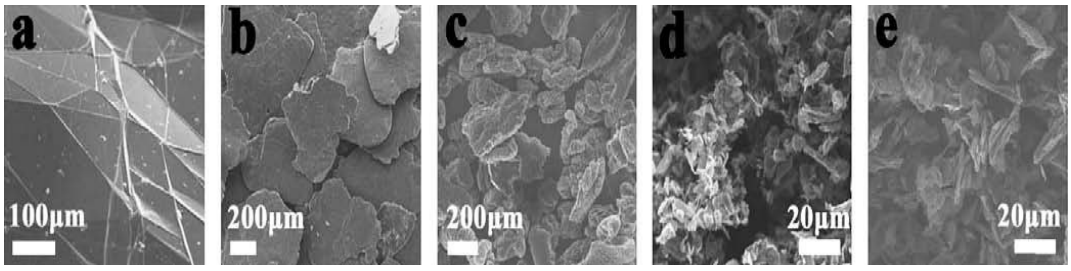

Figure 3-4 Typical SEM micrographs of graphene from different graphite materials [13]

3.1.3 Transmission Electron Microscope (TEM)

In a transmission electron microscope, the topology of the samples is studied by passing a beam of electrons through an ultra thin specimen. A transmission electron microscope is constituted of: (1) two or three condenser lenses to focus the electron beam on the sample, (2) an objective lens to form the diffraction on the back focal plane and the image of the sample on the image plane, (3) some intermediate lenses to magnify the image or the diffraction pattern on the screen. If the sample is thin (< 200 nm) and constituted of light chemical elements, the image presents a very low contrast when it is focused. To obtain a contrasted image, an objective diaphragm is inserted at the back focal plane to select the transmitted beam (and possibly some diffracted beam). The crystalline parts in Bragg orientation appear dark and the amorphous or not Bragg oriented parts appear bright. To do that, the incident beam must be tilted so that the diffracted beam is positioned on the objective lens axis to avoid off-axis aberrations. This mode is called the dark-field mode (DF). The bright field (BF) and DF modes are used for imaging materials to nanometre scale. A "light source" at the top of the microscope emits the electrons that travel through vacuum in the column of the microscope. Unlike in a light microscope where glass lenses focuses the light. TEM uses electromagnetic lenses to focus the electrons into a very thin beam. The electron beam then travels through the specimen to be studied. Depending on the density of the material present, some of the electrons are scattered and disappear from the beam. At the bottom of the microscope the un-scattered electrons hit a fluorescent screen, which gives rise to a "shadow image" of the specimen with its different parts displayed in varied darkness according to their density. The image is magnified and can be studied directly by the operator or photographed with a camera. Objects to the order of less than a nanometer (i.e. 10^{-10} m) can be studied down to near atomic levels. The selected area diaphragm is used to select only one part of the imaged sample, for example a particle or a precipitate. This mode is called selected area electron diffraction SAED. The spherical aberrations of the objective lens limit the area of the selected object to few hundred nanometres. Nevertheless, it is possible to obtain diffraction patterns of a smaller object by focusing the electron beam with the projector lenses to obtain a small spot size on the object surface (2-10 nm). The spots of SAED become disks whose radii depend on the condenser diaphragm. SAED and micro-diffraction patterns of a crystal permit one to obtain the symmetry of its lattice and calculate its inter-planar distances, making use of the Bragg law [39,40].

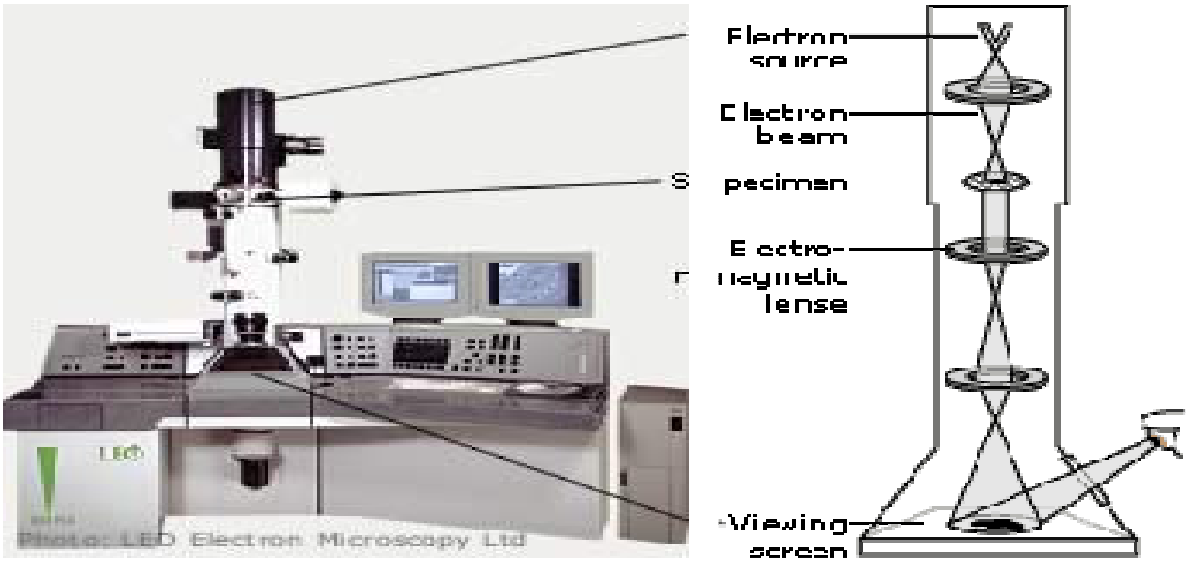

Figure 3-5 Image of Scanning Electron Microscopy setup. (Nobelprize.org [39])

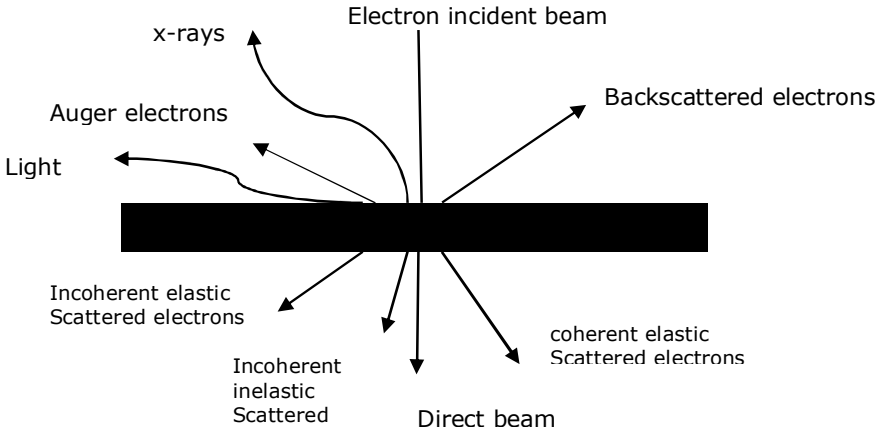

Figure 3-6 Interactions between material and electrons (sketch courtesy of Fichiers chap3)

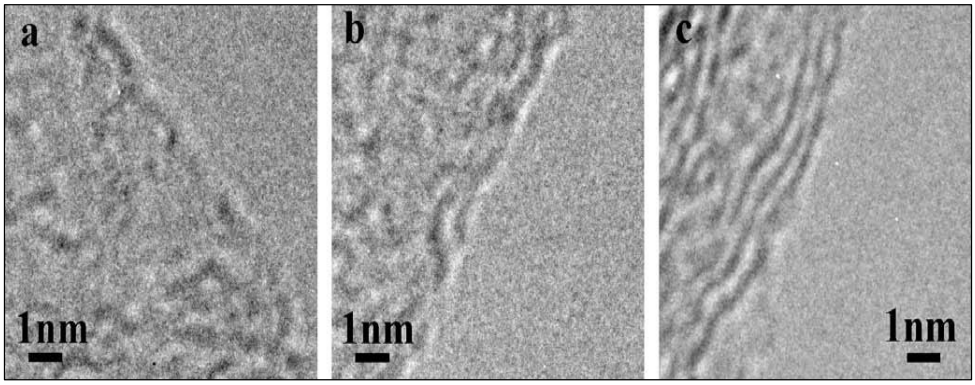

Figure 3-7 Typical HRTEM images of (a) single-, (b) double-, and (c) triple-layer graphene sheets with folded edges obtained by chemical exfoliation [13].

3.1.4 Fourier Transform Infrared Spectroscopy (FTIR)

Fourier transform infrared spectroscopy is a tool used to identify types of chemical bonds, i.e. functional groups in a molecule, by irradiating the sample with infrared radiation (IR). IR is electromagnetic radiation of a wavelength longer than that of visible light, but shorter than that of microwaves. The IR light is used because it contains enough energy to cause changes in vibration energy levels. The data collected is converted from an interference pattern to an infrared absorption spectrum that is unique to a particular molecule, like a fingerprint. This is due to the fact that the bonds vibrate at various frequencies depending on the element and therefore the wavelength of light absorbed is characteristic of the chemical bond and element. Infrared energy is emitted from a glowing black-body source. This beam passes through an aperture which controls the amount of energy presented to the sample (and, ultimately, to the detector). The beam enters the interferometer where the "spectral encoding" takes place. The resulting interferogram signal then exits the interferometer. The beam enters the sample compartment where it is transmitted through, or reflected off the surface of the sample, depending on the type of analysis being done. At this stage specific frequencies of energy, which are uniquely characteristic of the sample, are absorbed. The beam finally passes to the detector for final recording. The detectors used are specially designed to measure the special interferogram signal. The measured signal is digitized and sent to the computer where the Fourier transformation takes place. The final infrared spectrum is then presented to the user for interpretation and possibly further manipulation. Because there needs to be a relative scale for the absorption intensity, a background spectrum must also be measured. This is normally a measurement with no sample in the beam. This can be compared to the measurement with the sample in the beam to determine the "percent transmittance." This technique results in a spectrum which has all of the instrumental characteristics removed. Thus, all spectral features which are present are strictly due to the sample. A single background measurement can be used for many sample measurements because this spectrum is characteristic of the instrument itself.

Fourier transfer infrared radiation analysis (FTIR) can also be used for quantitative analysis because the strength of the absorption is proportional to the concentration. Therefore a quantitative measure of components of an unknown mixture may be obtained [41,42,43].

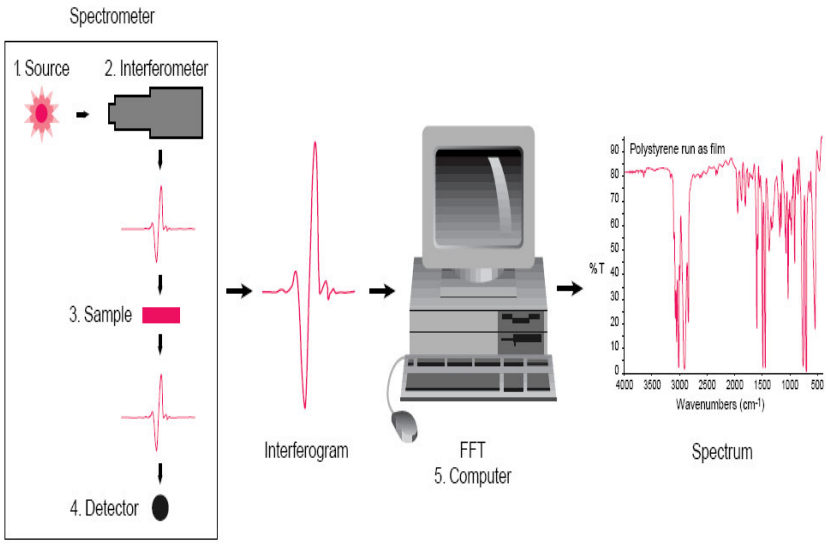

Figure 3-8 Fourier-transform infrared spectroscopy setup (courtesy of thermonicolet.com)

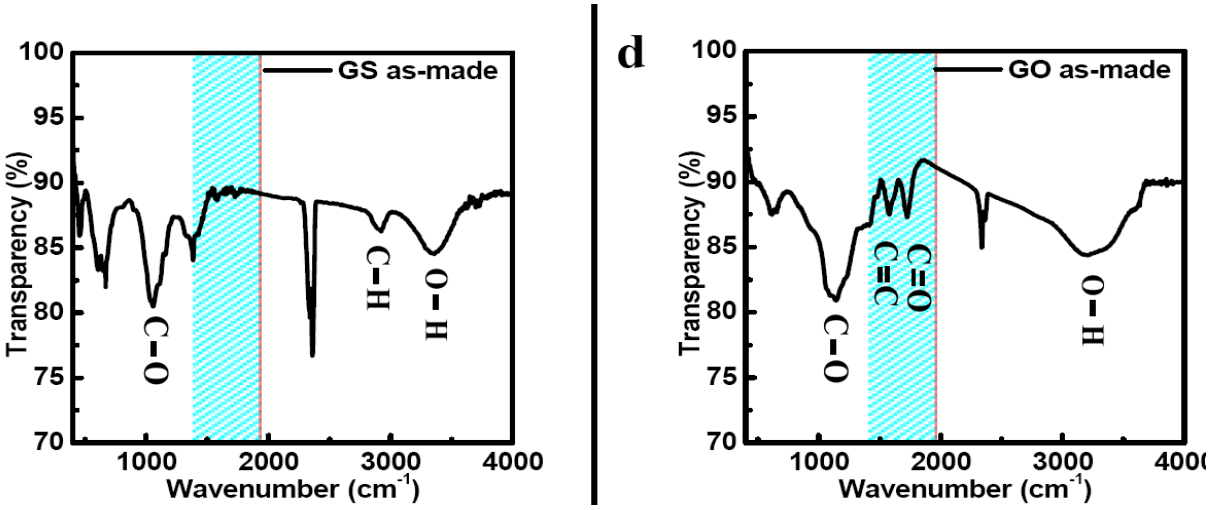

Figure 3-9 IR spectra (400-4000cm^{-1}) of as-made GS and GO. The shading region is from about 1400 to 1900 cm^{-1} showing the signal of carboxylic groups [30]. The absorption at 3390 cm^{-1} indicates the presences of the hydroxyl (OH group) and at a wave number of 1629 cm^{-1} and 1720 cm^{-1} indicates the presence of the carbonyl and carboxyl respectively [32] .

3.1.5 Raman Spectroscopy

Infrared (IR) and Raman spectroscopy both measure the vibration energies of molecules but these methods rely on different selection rules. For a vibration motion to be IR active, the dipole moment of the molecule must change. Raman scattering is a powerful light scattering technique used to diagnose the internal structure of molecules and crystals by utilization of an intense and monochromatic light source (laser beam) in the visible, near infrared or near ultraviolet range. It is a complementary technique to FTIR because IR absorption only maps out the non-Raman active excitation. Light of a known frequency and polarization is scattered from a sample. As the light interacts with the sample, it is frequency-shifted indicating that some energy is deposited in the sample. Fluorescence signals, similar to Raman radiation, are also shifted from the laser frequency, and so can be difficult to separate from the other signals. Therefore a calibration of the spectrometer response to a source with a known spectrum is done. The wavelength/intensity information is then converted to frequency/intensity which is analyzed to obtain the vibration, rotation and other low-frequency modes specific of the chemical bonds. Unlike the case for FTIR measurements, water does not interfere with the signal and Raman spectroscopy can measure species present in a volume less than 1 μm in diameter. In the Raman spectra of graphene, there are many features that can be identified with specific phonon modes and with specific Raman scattering processes. The Raman spectra of graphene can provide us with information about the exceptional 1D property of carbon materials, such as their phonon structure and their electronic structure, as well as information about sample imperfections (defects). Since mechanical properties, elastic properties and thermal properties also are strongly influenced by phonons, Raman spectra provide general information about the structure and properties of graphene. Raman scattering is the inelastic scattering of light. During a scattering event, an electron is excited from the valence energy band to the conduction energy band by absorbing a photon. The excited electron relaxes to the valence band by emitting a photon. Generally the Raman spectrum of the scattered photons (light), having energy less than that of the incident photon, is observed. By measuring the intensity of the scattered light as a function of frequency downshift (lost energy) of the scattered light, (which is plotted in Raman spectra), we obtain an accurate measure of the phonon frequencies of the material. By combining this information with the original geometrical structure of a crystal (or molecule), we can deduce the phonon dispersion relations (or normal mode frequencies). Raman scattering can be

measured for phonon emission (as described above) or for phonon absorption and these two processes are called the Stokes process and anti-Stokes process, respectively. Since Raman scattering refers to the inelastic scattering of light, not only phonons, but any elementary excitation (such as a magnon, plasmon etc.) can be involved in a scattering process in which the elementary excitation satisfies energy–momentum conservation in the scattering process [44,45,46].

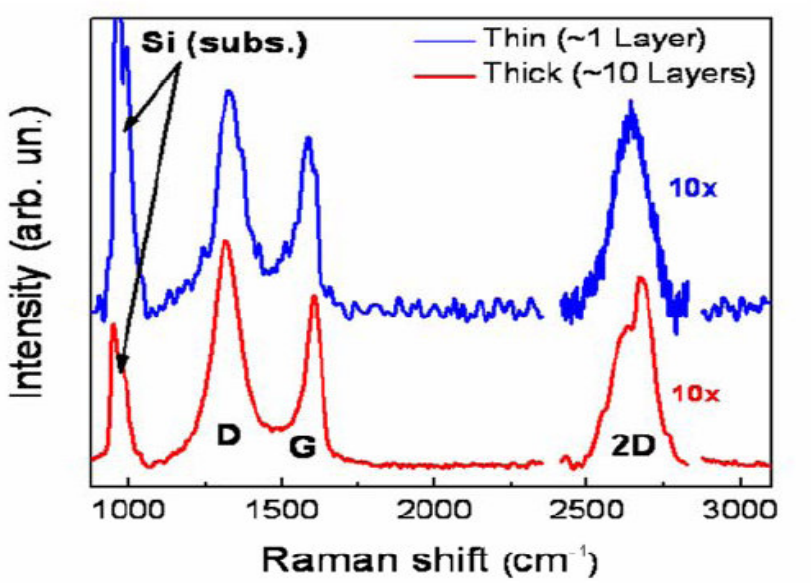

Figure 3-10 The entire Raman spectra for a single- and multi-layered reduced graphene oxide [31] .The three major carbon features (D, G and 2D peaks) along with the Si peaks from the substrates are labelled. The prominent D peak in the Raman spectra is an indication of the presence of disorder in the samples [46]

Table 2 Raman vibrational modes of graphite [46]

Name	**cm^{-1}**	**Resonance[(a)]**	**notes**
iTA (in-plane transverse acoustic)	288	DR1	iTA mode, intra-valley scattering (q=2k)
LA (longitudinal acoustic)	453	DR1	LA mode, intra-valley scattering (q=2k)
RBM (radial breathing mode)	248	SR	Nanotubes only vibration of radius
IFM^-(intermediate frequency phonon mode)	750	DR2	Combination mode oTO-LA (q=2k)
oTO (out-plane transverse optic)	860	DR1	IR active mode in graphite
IFM+	960	DR2	Combination mode oTO-LA (q=2k)
D (disorder induced)	1350	DR1	LO or ITO mode, inter-valley scattering
LO (longitudinal optics)	1450	DR1	LO mode inter-valley scattering (q=2k)
BWF^f	1550	SR	Plasmon mode, only metallic carbons
G	1582	SR	Raman active mode of graphite
M^-	1732	DR2	Overtone of oTO mode
M^+	1755	DR2	Overtone of oTO mode
iTOLA	1950	DR2	Combination mode oTO-LA
G'	2700	DR2	Overtone of D mode
2LO	2900	DR2	Overtone of LO mode
2G	3180	DR2	Overtone of G mode

[a]SR : First order, DR1 and DR2 are one and two phonons double resonance respectively.

3.1.6 Ultra-Violet and Visible Absorption Spectroscopy

Ultraviolet and visible absorption spectroscopy is the measurement of the attenuation of a beam of light with frequency range from the near UV, through the visible, into the near-IR, i.e. over the range 320−1000 nm, after it passed through a sample. Photons in this wavelength range contain enough energy to excite outer electrons to higher energy levels as they are absorbed. The optical spectrometer records the wavelength at which absorption occurs together with the degree of absorption at each wavelength. The resulting spectrum can be used for characterization of the optical and electronic properties of the material, for instance for determining the band gap from the cut-off point and the concentration, by applying the Beer-Lambert Law [47] .

Metals are opaque because incident radiation having frequencies within the visible range excites electrons into the unoccupied energy states above the Fermi energy. Consequently the incident radiation is absorbed. Total absorption takes place within a very thin outer layer, usually less than 0.1 μm thick, thus only metallic films thinner than 0.1 μm are capable of transmitting visible light. All frequencies of visible light are absorbed by metals because of the continuously available empty electron states, which permit electron transitions. Metals are opaque to all electromagnetic radiation on the low end of the frequency spectrum, from radio waves through the infrared, the visible and into about the middle of the ultraviolet region. Metals are transparent to high frequency radiation (X- and γ rays). When radiation is absorbed, most of the absorbed energy is re-emitted from the surface in the form of visible light of the same wavelength, which appears as reflected light. Non metallic materials may be opaque or transparent to visible light and if transparent, they often appear coloured. Light radiation is absorbed in this group of materials by two mechanisms which also influence the transmission characteristics of these non-metals. One of these is electronic polarization, which is only important at light frequencies in the vicinity of the relaxation frequency of the constituent atoms. The other mechanism involves transitions of the electrons from the valence band to the conduction band. The occurence of these processes depends on the electron energy band structure of the material. The possible electron band structures in solids at 0 K is displayed below in Figure 3-11. Figure 3-11 The possible electron band structures in solids at 0 K. (a) The one outermost band is only partially filled with electrons. This energy band

structure is typical of metals with a single s valence electron. (b) The electron band structure of metals, wherein there is an overlap of filled and empty outer bands. (c) The electron band structure of insulators. The filled valence band is separated from the empty conduction band by a large band gap (>2 eV). (d) The band structure found in semiconductors with a narrow band gap (<2 eV). Interactions with light radiation can also occur in dielectric solids having wide gaps, involving other than valence band-conduction band electron transitions. If impurities or electrically active defects are present, electron levels within the band gap may be introduced, such as the donor and acceptor levels. Light radiation of specific wavelengths may be emitted as a result of electron transitions involving these levels within the band gap.

Absorption of a photon of light may occur by the promotion or excitation of an electron from the nearly filled valence band, across the band gap into an empty state within the conduction band. A free electron in the conduction band and a hole in the valence band are created. These excitations with the accompanying absorption can take place only if the photon energy is greater than the band gap. The minimum wavelength for visible light is about 0.4 μm. The maximum band gap energy for which absorption of visible light is possible is 3.1 eV, as calculated below:

$$E_g(max) = \frac{hc}{\lambda(min)}$$

Where c = $3x10^8$ m/s, h=$4.13x10^{-15}$ eV.s,and λ is in meters.

On the other hand the maximum wavelength for visible light is about 0.7 μm; the minimum band gap energy for which there is absorption of visible light is 1.8 eV as calculated below

$$E_g(max) = \frac{hc}{\lambda(max)}$$

These results imply that all visible light is absorbed by valence band to conduction band electron transitions, for those semiconducting materials that have band gap energies less than about 1.8 eV. Thus these materials are opaque. Only a portion of the visible spectrum is absorbed by materials having band gap energies between 1.8 and 3.1 eV. The intensity of the net absorbed radiation is dependent on the character of the medium as well as the path length within it. The intensity of transmitted radiation decreases with the distance that the light traverses [48].

The band gaps of thin films can be determined through curve fitting using the semi-empirical Tauc and Davis–Mott model, based on the measurement of optical absorption at the visible and near infrared range. This study provides a practicable option for the determination of band gaps for ultra-thin films whose peaks cannot be well resolved in absorption spectra [49] .

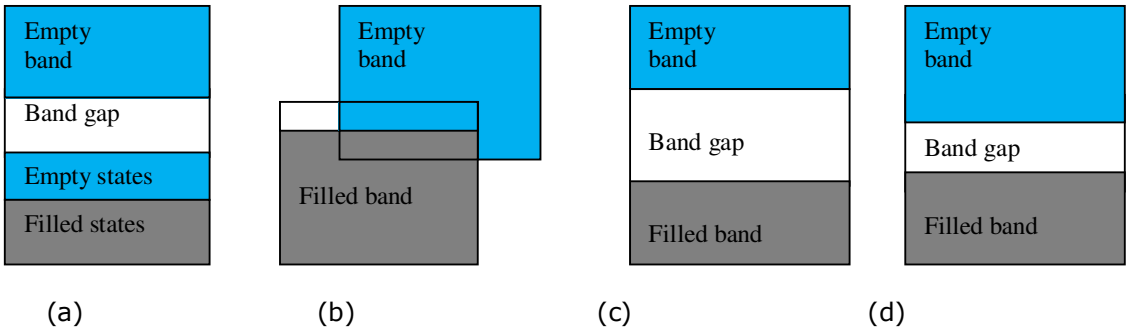

Figure 3-11 The possible electron band structures in solids at 0 K. (a) The one outermost band is only partially filled with electrons. This energy band structure is typical of metals with a single s valence electron. (b) The electron band structure of metals, wherein there is an overlap of filled and empty outer bands. (c) The electron band structure of insulators. The filled valence band is separated from the empty conduction band by a large band gap (>2 eV). (d) The band structure found in semiconductors with a narrow band gap (<2 eV).

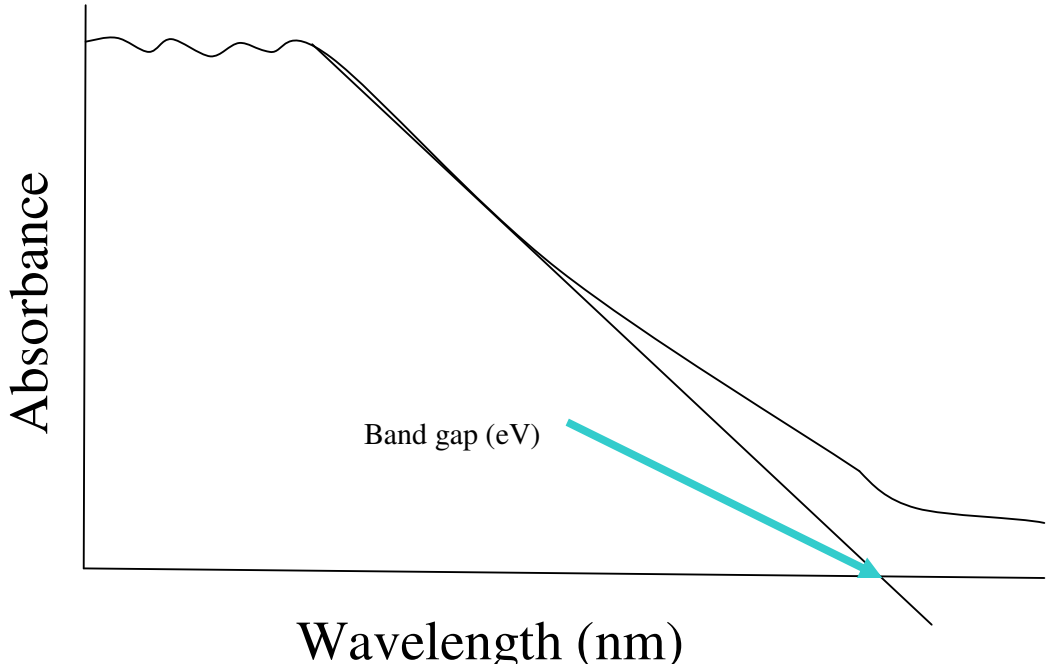

Figure 3-12 Tauc plot for estimating the optical band gap of thin films

CHAPTER 4

4.1 Experimental procedure

From all the sample preparation techniques discussed above, the Hummers method was chosen to be used in this work, because it allows for deposition on large surfaces areas. Presented below is the procedure used in this work to produce graphene sheets dispersed in water.

4.1.1 Hummers method

(a) Oxidation of graphite

An amount of 5 g of graphite powder was mixed with 3.8 g sodium nitrate in an ice bath. Then 169 ml of concentrated sulphuric acid was added to the mixture and stirred until homogenized. Next 22.5 g of potassium permanganate was gradually added to the solution over an hour while stirring. The solution was removed from the ice bath after 2 hours and then stirred for 5 days, resulting in a brown viscous slurry.

The slurry was added to 500 ml aqueous solution of 5 wt% H_2SO_4 (drying agent) over an hour while being continuously stirred and then stirred for a further 2 hours.

$C + 2H_2SO_4 \longrightarrow CO_2+2H_2O+2SO_2$

Hydrogen peroxide 30 wt% aqueous solution was added to the mixture and stirred for a further 2 hours to neutralize the $KMnO_4$.

(b) Purification of mixture

The slurry was dispersed and precipitated in a 500 ml aqueous solution of 3 wt% H_2SO_4 and 0.53 wt% H_2O_2 by centrifuging and the supernatant solution removed. This procedure was repeated 10 times.

The 0.5 ml of the slurry was dispersed in 500 ml de-ionized H_2O and then ultra-sonificated, resulting in a clear yellow suspension of exfoliated graphene oxide. The application of external energy like the ultrasonic vibration or thermal shock exfoliates the 3D graphite oxide to 2D graphite oxide sheets.

The graphene oxide consists of epoxide and hydroxyl with carbonyl and carboxyl at it's edges. These oxygen functionalities alter the Van de Waals interactions

between the GO layers into Hydropholic interactions. The GO is soluble in water allowing it to readily hydrate and exfoliate in aqueous media, forming a stable colloidal dispersion of graphite sheets in water.

4.1.2 Reduction

The colloidal suspension of individual graphene oxide sheets in water with an acidic pH=3 was mixed with a potassium hydroxide (KOH) aqueous solution increasing the Ph of the suspension to a more basic Ph=11. The solution was then stirred for 2 hours at room temperature after which hydrazine hydrate was added and the solution was then stirred at 35 °C for a further 6h resulting in a black suspension [50].

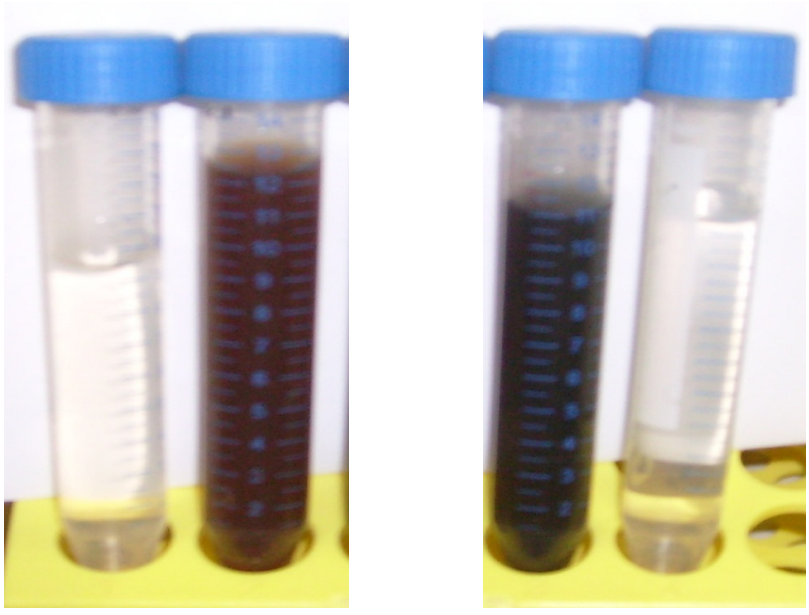

Suspension of insulating GO

Suspension of conducting rGO

Figure 4-1 Transformation of clear yellow graphene oxide to black graphene sheets suspension

4.1.3 Cleaning of substrates

The cleaning of glass and silicon oxide substrates was done using the following alcohols, added at time intervals of 12 minutes: Methanol, acetone, trichloroethylene, acetone, methanol and de-ionized water.

4.1.4 Sample preparation

a) Spin coating conditions

The solution was spread across the surface of the glass and silicon oxide substrates and the samples were then blown at the centre with dry nitrogen while simultaneously spinning the sample at 4000 rpm.

b) Drop casting conditions

The substrates were first thoroughly washed using the cleaning procedure mentioned above and dried by blowing with nitrogen gas. They were then heated at 65 °C for a couple of minutes to evaporate additional water and to slightly heat the substrate for better coating. The solution was then dropped on the substrate with the aid of a pipette and allowed to dry for an hour.

c) Solutions

Solutions were analyzed optically in a liquid cell, consisting of a small container made from NaCl (or other IR-transparent material) which can be filled with liquid. This creates a longer path length for the sample, leading to an increased sensitivity [39].

4.1.5 Annealing conditions

a) Annealing of graphene oxide and reduced graphene oxide sheets

The graphene oxide films were heated at 150 °C for 15 minutes under an argon environment. The reduced graphene oxide sheets were heated at 500 °C for 6 h in a vacuum [51].

4.1.6 Reduced Graphene Oxide irradiation

In the present study the reduced graphene oxide sample was irradiated with a 450 keV proton beam using the Van de Graaff accelerator at iThemba LABS with a fluence range given by Table 3. For the whole experiment the current was kept constant at 50 nA and the beam diameter fixed to 2 mm. However the time was varied from 30 to 180 minutes. The rGO films were also irradiated with an ultra-violent pulsed laser (EMG-203MSC University of Stellenbosch) at a 308 nm wavelength, using a 6 mm diameter aluminium mask. The voltage was adjusted from 19 kV to 25 kV and each spot was irradiated with 10 pulses. The structural dependence of the graphene sheets on the excitation power was measured using a photo-spectrometer (TUT) at 514 nm (green light) with a 50X objective to avoid sample damage by over-focusing the beam, and a 100X objective to image the sheets. Measurements were performed from 5 to 40 mW incident power at room temperature.

Table 3 Table of dose calculation for proton irradiated reduced GO film

Spot	Time (s)	Charge (C)	Dose (ions/cm^2)
1	1800	9.00E-05	1.79E+16
2	3600	1.80E-04	3.58E+16
3	5400	2.70E-04	5.36E+16
4	7200	3.60E-04	7.15E+16
5	9000	4.50E-04	8.94E+16
6	10800	5.40E-04	1.07E+17

CHAPTER 5

5.1 Results and discussion

5.1.1 Morphology

The morphology of the graphene oxide (GO) and reduced graphene oxide (rGO) films were studied using the AFM nanoscope at iThemba LABS and the Nanosurf easyScan 2 FlexAFM system at the University of Stellenbosch in non-contact mode. Figure 5-1, Figure 5-2 and Figure 5-3 are Nanoscope AFM analyses on graphene oxide (GO-G) deposited on glass substrates and Figure 5-4 is for reduced graphene oxide (rGO-G). Both these samples were used as control or reference samples. They were prepared by a group from the material science and engineering department at Rutgers University led by Professor M Chowalla. An image of the morphology was captured to get an idea of the alignment and disparity of the sheets. A height profile was also done to obtain the difference in height and width of the two samples. The films were prepared by spin coating the solutions at 5500 rpm. By comparing Figure 5-3 with Figure 5-4 it can be observed that the as-deposited graphene film had a much rougher surface with an average roughness of 7.38 nm compared to 1.99 nm of the reduced graphene oxide film. It was also found to be approximately twice the thickness of the reduced sample. This indicated that the reduced sample had less stacked layers and had a much smoother surface i.e. was more exfoliated, and that the oxygen had been removed. The roughness was attributed to the sp^3 C-O bond centres and point defects produced during oxidation in the carbon lattice, causing wrinkling of the sheets. The random attachment of oxygen on top and at the bottom surfaces creates a disorder with the O appearing as protrusions.

Figure 5-5, Figure 5-6 and Figure 5-7 are Nanosurf imaged reference samples deposited on silicon dioxide substrates by drop casting. The thicknesses of the sheets vary according to the number of sheets from 1.141 nm to 4 nm. The thickness of an individual sheet can be determined by taking a height profile of the sample at the edges, because the sheets are irregularly shaped and distributed. The sheets normally have step geometry and therefore the thickness of an individual sheet can be determined by measuring the step size.

Raman spectroscopy can also be used for the identification of graphene layers. The D peak of the multi-layered reduced graphene oxide has two components: D_1 and D_2 as compared to the single sharp D peak of the monolayer sample in Figure 5-8 . The multi-layered spectrum is characteristic of a typical graphite sample as discussed by A.C Ferraris *et al.* (2006), due to the difference in electronic structure of graphene and graphite.

In another attempt to isolate the graphene oxide films the MRG (iThemba LABS) prepared solution was vacuum-filtrated with the aim to transfer the graphene oxide film onto a variety of substrates. The results of the experiment are shown in Figure 5-9. Since the individual sheets of GO are sufficiently larger than the pore dimension, growth occurs by creating a uniform continuous thin film of a single layer first and then by building additional layers on the top, covering the membranes surface. Since the pores are not uniformly distributed on the membrane and the GO sheets are irregularly shaped with a distribution in sizes, several sheets from the nearby pore can overlap giving rise to regions consisting of multiple layers among the mono-layers.

Figure 5-10 is an AFM image of a strip of graphite 16 mm in length which was irradiated with a 2 MeV proton beam with a diameter of 2 mm and a dose ranging from 5.9×10^{18} to 29.4×10^{19} ions/cm^2. Five spots 3 mm apart were irradiated for 593 seconds each, with a current increment of 50 μA. The first spot was irradiated at a current of 50 μA and the last at 250 μA. The irradiation of the sample caused the carbon bonds between the atoms to break resulting in the transformation of the crystallographic structure of the strips from a crystalline to an amorphous structure.

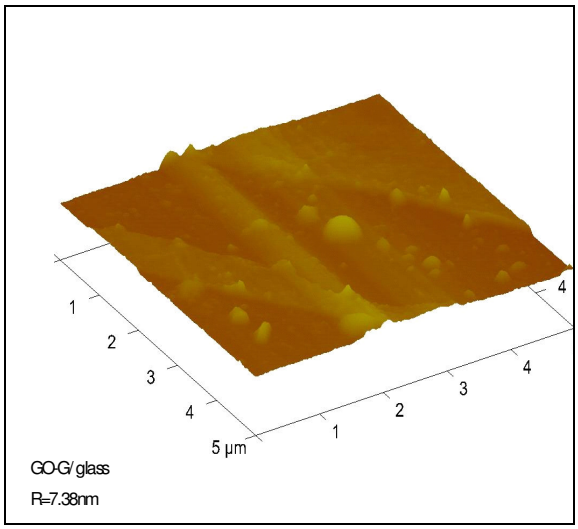

Figure 5-1 3D image of Graphene oxide reference sample deposited on glass by spin coating at 5500 rmps. The surface of the film is very rough due to the presence of the oxygen functional groups and sp^3 hybridized clusters.

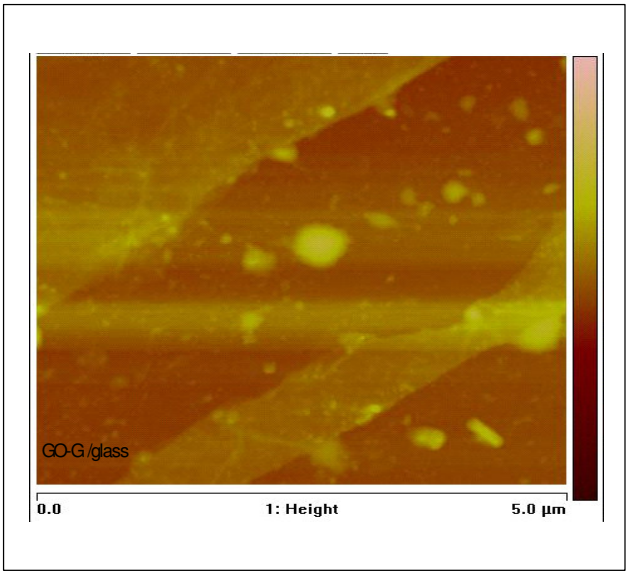

Figure 5-2 AFM image of graphene oxide (GO-G) spin coated onto a glass substrate with an average roughness of 7.38 nm. The light spots on the image can be un-dissolved salts added during the oxidation process and dust particles.

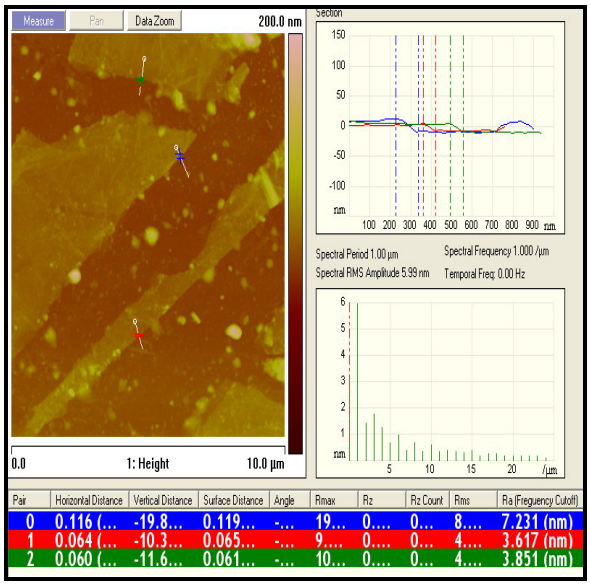

Figure 5-3 Height profile for the graphene oxide (GO-G) deposited on a glass substrate with an average thickness of 18.75nm, indicating a multi-layered sample. The thickness was calculated by taking a height profile of three different sheet edges as displayed on the right side of the image.

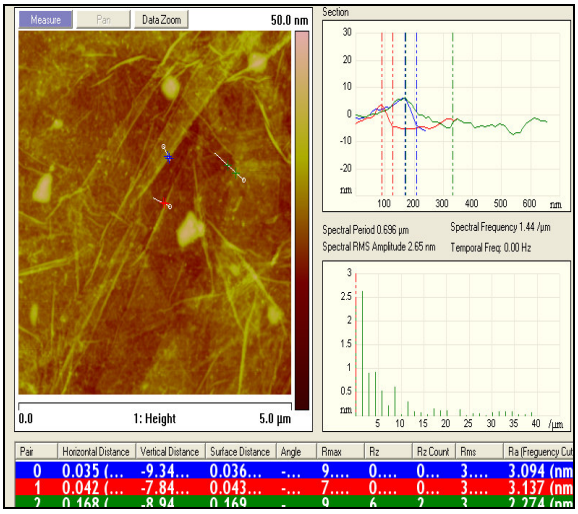

Figure 5-4 Height profiles for the reduced graphene (rGO-G) spin coated at 5500 rpm on a glass substrate with an average thickness of 7.95nm and average roughness of 1.99 nm. The removal of the epoxide and hydroxyl bonded below and above the carbon layer during reduction has resulted in an enormous decrease in the average roughness.

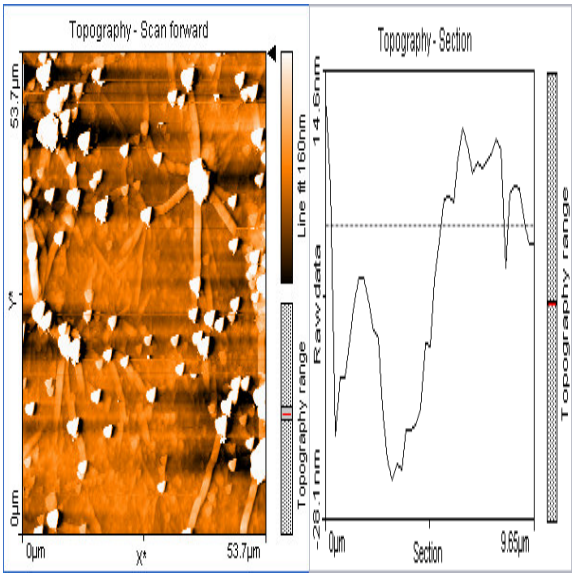

Figure 5-5 Reduced graphene oxide reference sample drop coated onto a $Si/Si0_2$ substrate with minimum thickness of 1.358 nm as determined from the cross section image on the right.

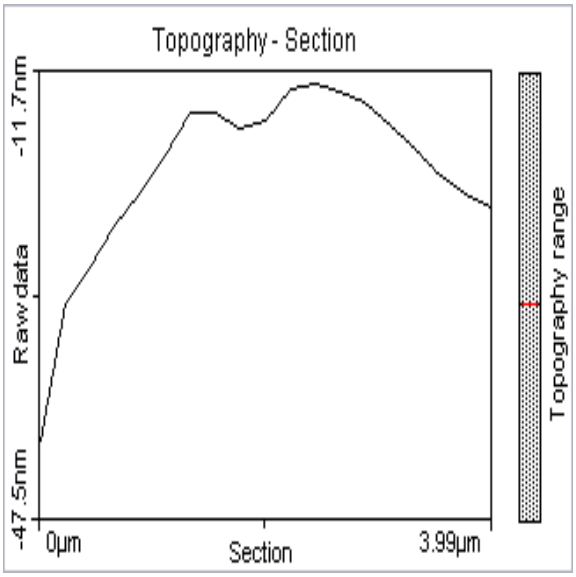

Figure 5-6 Cross section of reduced graphene oxide reference sample on $Si/Si0_2$ substrate with thickness of 1.141 nm, measured on the "step" edge of two overlapping sheets.

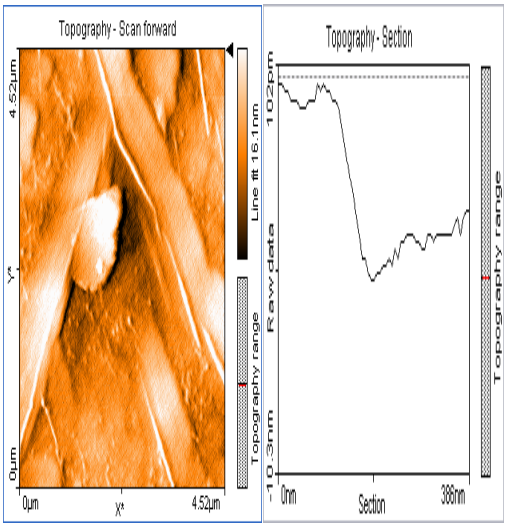

Figure 5-7 Reduced graphene oxide reference sample on $Si/Si0_2$ substrate with individual sheet thickness of 4 nm as measured from the cross section captured.

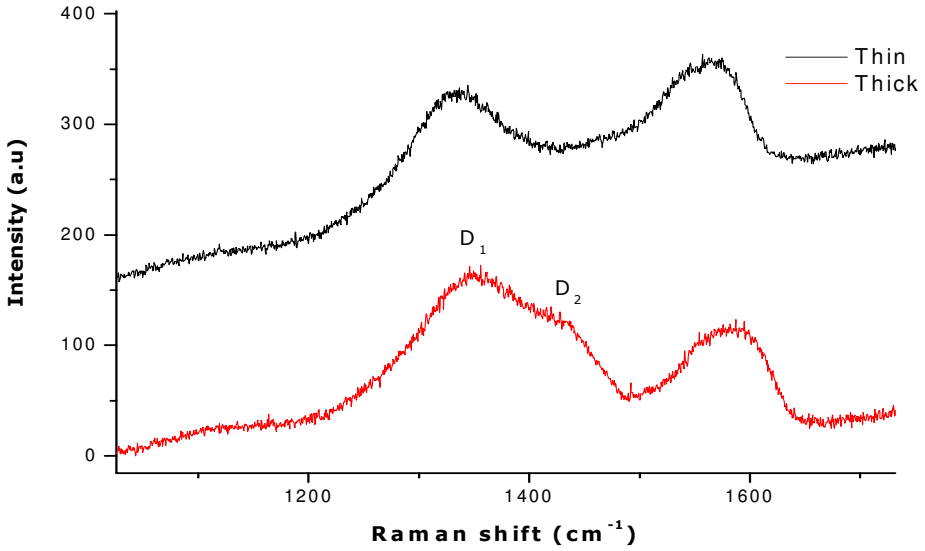

Figure 5-8 Raman spectra for reduced GO for different number of graphene layers. Black layer represents a monolayer characterized by a single sharp D peak. The red layer represents a multilayered sample as characterized by the two component D peak.

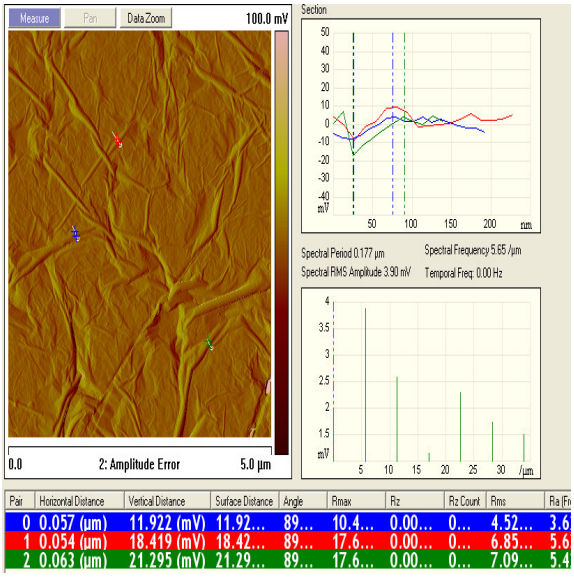

Figure 5-9 Continuous Graphene film vacuum filtrated onto a track etch membrane, consisting of multiple layers among monolayers.

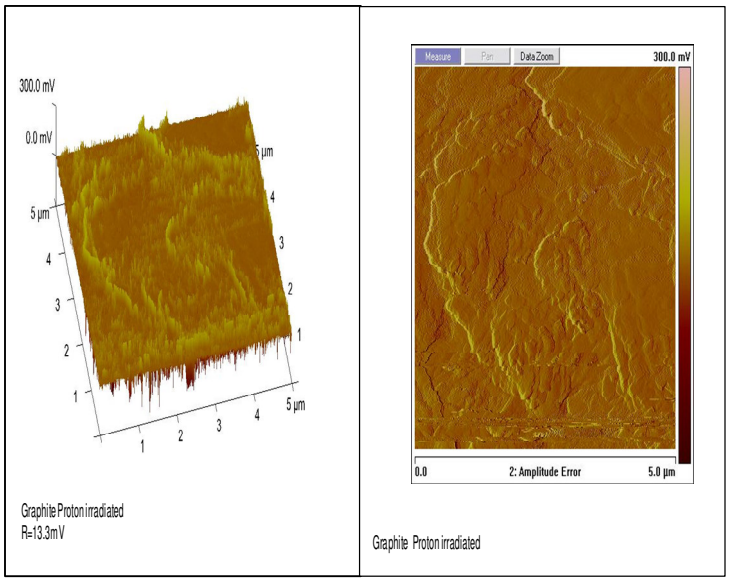

Figure 5-10 3D-image results for 2 MeV proton irradiated graphite strip with an average roughness of 13.3 rms irradiated with a dose ranging from $5.9x10^{18}$ to $29.4x10^{19}$ ions/cm^2. The surface is profoundly rough due to the reduction of crystallite size during irradiation.

Further morphological investigations of the graphene oxide and reduced graphene oxide films were obtained using the scanning electron microscope, Stereo Scan 440 at the University of Cape Town, operating at an accelerating voltage of 20 kV, and a high resolution scanning electron microscope, (JEOL) operating at an accelerating voltage of 2 kV at the CSIR in Pretoria. From the SEM images shown (see Figure 5-11), of GO-G (left) and rGO-G (right) the morphology and approximate size of the individual sheets of the film spin coated on glass can be observed. GO-G consists of a highly ordered stack of graphene oxide layers. Contrast between the conducting rGO-G films and the insulating substrate, indicates the presence of uncovered regions while the GO-G films are stacked on top of each other. The micrograph of rGO-G also displays undissolved salts at the film's surface. Figure 5-12 shows a SEM image of a reduced graphene oxide reference sample on a silicon oxide substrate grown by drop casting. Even though the samples were deposited with the aim of producing different thicknesses, the challenge of inhomogeneous deposition still prevails. There is evidence of multiple layers in the single layer deposited samples and isolated sheets in the multilayered samples. The samples were prepared by the modified Hummers method which involves the oxidation of graphite by the introduction of salts. During the purification process not all the salts introduced were dissolved, as is evident from the clusters on top of the sheets (illustrated by Figure 5-13). Figure 5-14 shows a SEM micrograph of a reduced graphene oxide MRG solution deposited on FTO substrate by drop casting. The levels of dilution of the as-prepared solutions play a role in the conglomeration of the sheets during deposition. The more diluted the solution the higher the probability of individual sheet deposition. By controlling the level of dilution of the samples the number of sheets can be controlled. Figure 5-15 is SEM micrograph of the solution of rGO-P produced at MRG and deposited on glass with different number of layers. Figure 5-15 (a) illustrates a case of only one deposition while Figure 5-15 (b) shows a case where the solution was deposited eleven times using drop casting. The more layers deposited, the thicker, rougher and harder it is to distinguish between individual flakes. The multilayered sample is not good for characterization but it is perfect for transport measurements because of the extensive network of long, broad wrinkles across the film surface. The as-prepared sheets need to be diluted up to 100 times to produce a clear solution with the sheets suspended in the water. The number of layers deposited is not the only factor to consider during deposition but also the concentration of the solution needs to be taken into account. If the solutions are too concentrated even a single layer deposition can result in a stack of sheets.

A SEM image of the Reduced graphene oxide (MRG solution) deposited on a track etch membrane with 0.3 μm pores is displayed in Figure 5-16. The figure shows the non-uniform distribution of the pores and pore sizes. It also illustrates that a monolayer of graphene can be suspended across the membrane for isolated sheet measurements.

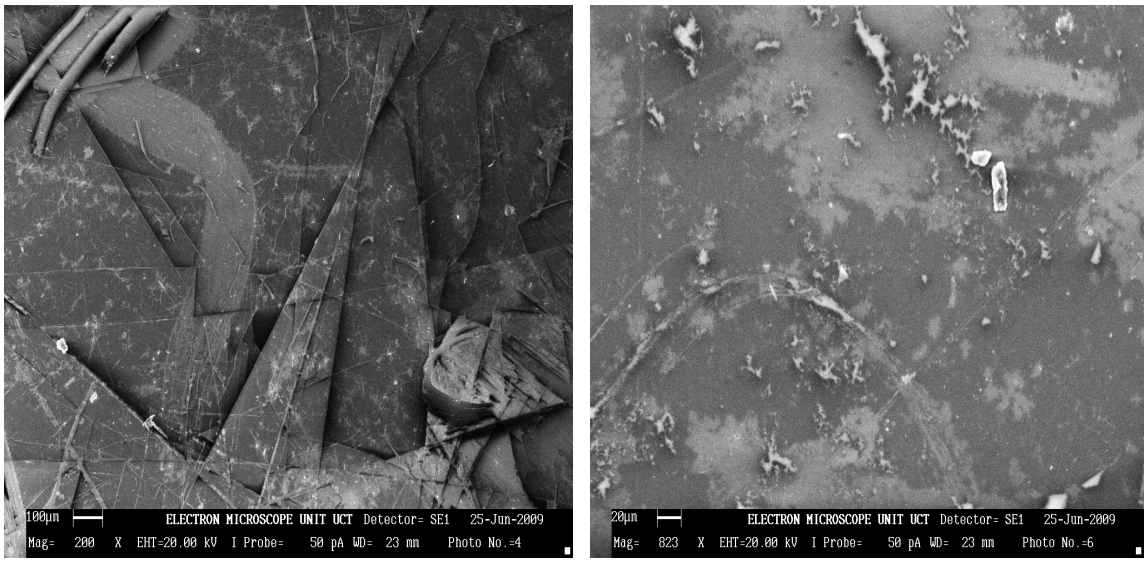

Figure 5-11 SEM images for GO-G (left) and rGO-G (right) spin coated on a glass substrate. GO-G consists of highly ordered stack of graphene oxide layers.

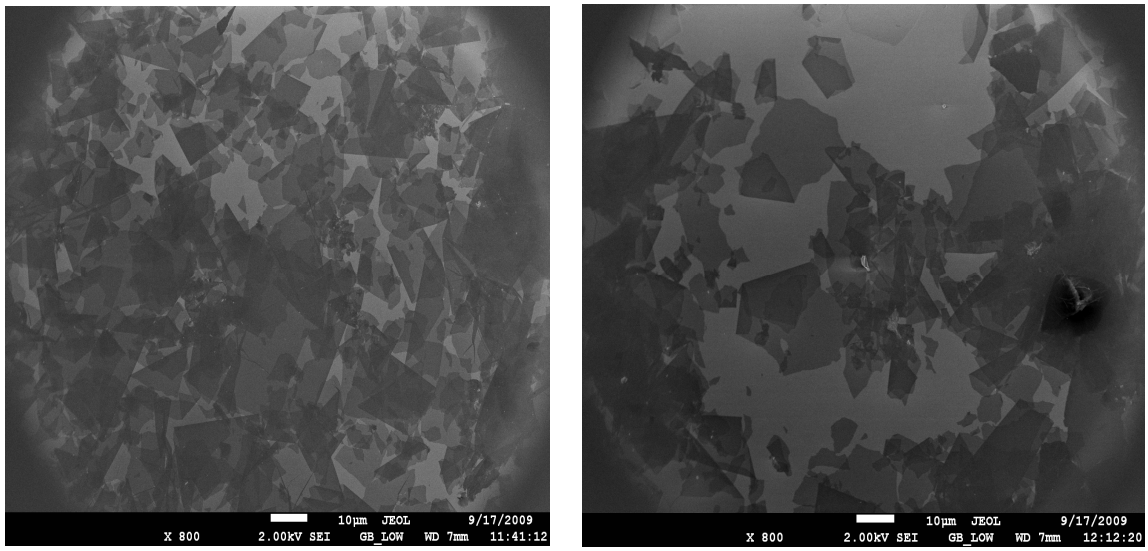

Figure 5-12 Reduced graphene oxide 10-15 nm thick (left) and 1-3 nm thick (right). The samples were deposited with an intention to obtain different thickness but as mentioned earlier one of the shortcomings of chemical reduction is the aggregation of the layers due to the attraction force between the layers.

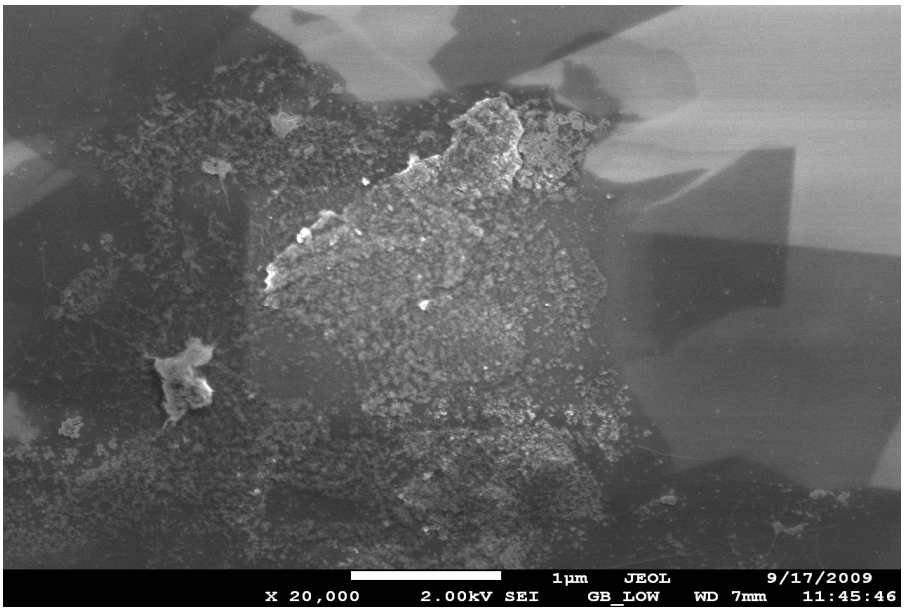

Figure 5-13 Reduced graphene oxide with undissolved salts decorating the sheet's surface. The particles are charging as indicated by their brightness in the image as compared to the semi-conducting graphene sheets.

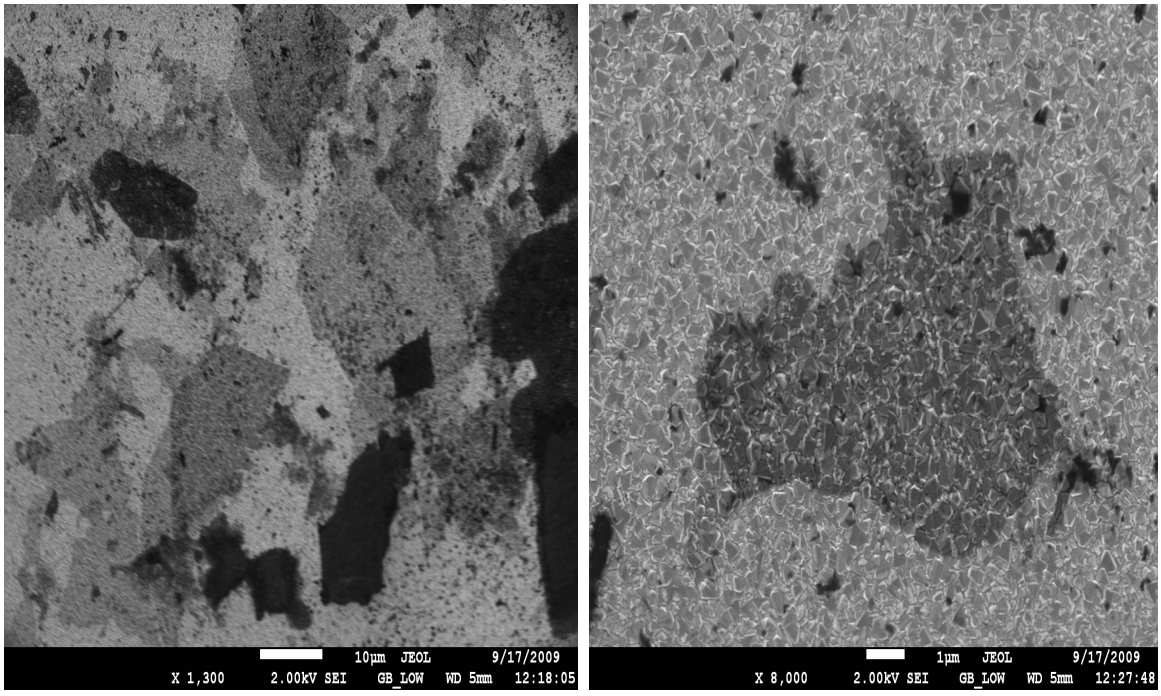

Figure 5-14 Reduced graphene oxide sheets and zoomed isolated reduced GO graphene oxide sheet deposited on FTO by drop coating, supporting the fact that the dilution level of the as-prepared solution is correlated to the number of deposited layers.

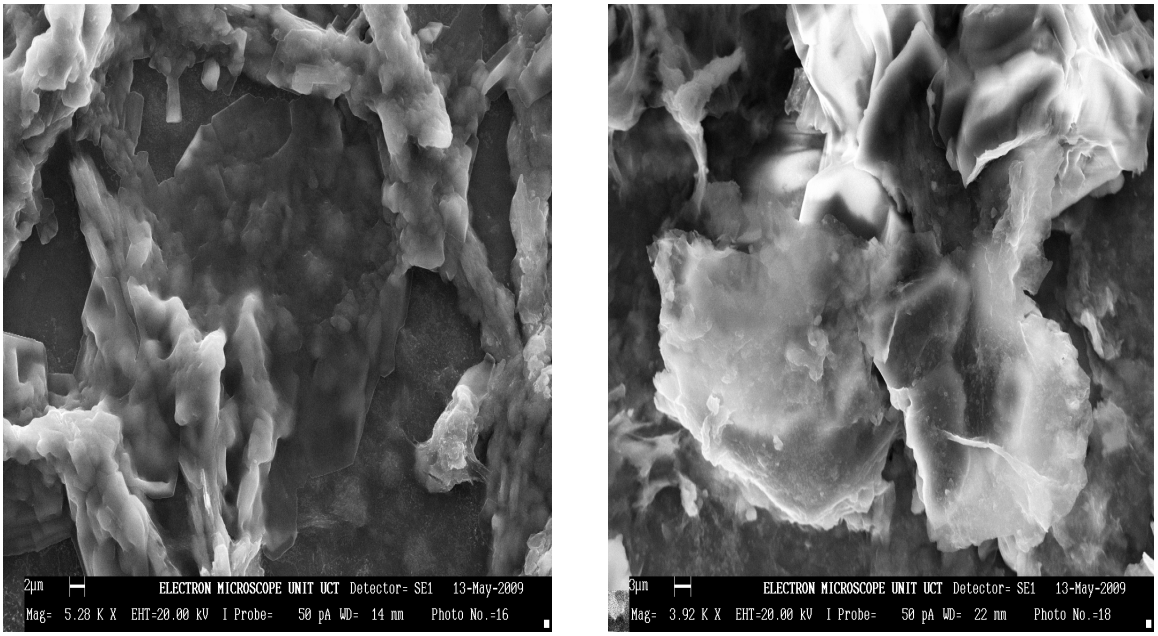

Figure 5-15 SEM image of rGO-P solution on glass drop coated once (left) and eleven times (right). When the number of layers coated on to the substrate increase the number of layers also increase.

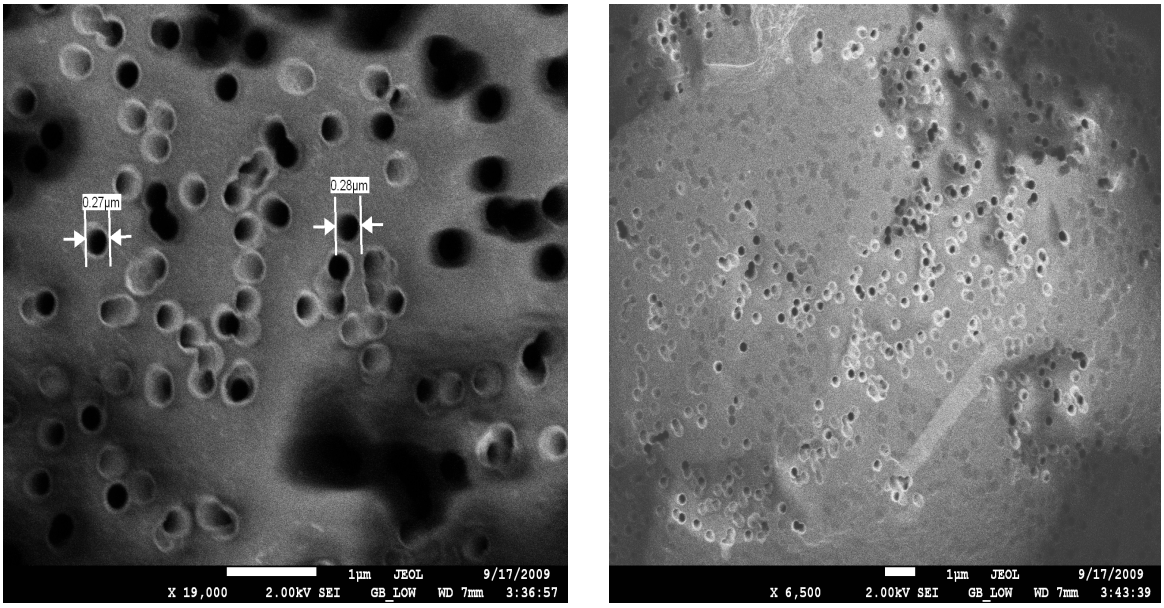

Figure 5-16 SEM micrograph of graphene sheet on track etch membrane revealing the ununiform distribution of the pores on the membrane.

5.1.2 Structure

A few drops of the graphene oxide and reduced graphene oxide from a MRG suspension were cast onto the copper grids used to support the targets for the transmission electron microscope so that they were covered by a thin layer of carbon film. The graphene oxide and reduced graphene oxide sheets were left on the grids after the solvent evaporated. The environment and atmosphere under which the films were grown had an impact on the structure of the sheets. The RT grown sample showed a compact amorphous structure, characterized by onion shaped fullerene structures, as shown in Figure 5-17, similar to that reported by E. Cappelli et al in 2007 [52]. Aqueous dispersions also aggregate during the evaporation process as illustrated by Figure 5-18. High resolution images of graphene oxide consisting of two layers and reduced graphene oxide consisting of three layers are displayed in Figure 5-19, with the number of layers indicated by the dark lines. Lattice fringes are also visible on the edges due to folds and rolls. The separation between the neighbouring fringes were measured to be 0.4 nm, which is larger than the inter-planar spacing of graphite (0.34 nm). This is attributed to the presence of oxygen functional groups on the graphene oxide layers as well as the possible inclusion of inter-lamellar molecules.

Figure 5-19 shows the electron diffraction pattern of graphene oxide, displaying the hexagonal structure of graphene. The significant structural changes occurring during the chemical processing from graphite to GO, and then to the reduced GO, are also reflected in their Raman spectra presented in Figure 5-20. The Raman spectrum of the graphite, as reported by S Stankovich (2007), displays a D peak at 1359 cm^{-1} and a prominent G peak at 1587 cm^{-1}, corresponding to the first-order scattering of the E_{2g} mode. In the Raman spectrum of GO, the D band becomes prominent, indicating the reduction in size of the in-plane sp^2 domains, possibly due to the extensive oxidation. In addition, the G band is broadened and shifted to 1599 cm^{-1}. The Raman spectrum of the reduced GO also contains both D and G bands at 1359 and 1590 cm^{-1} respectively, however with a decreased D/G intensity ratio compared to that in GO. This change suggests an increase in the average size of the sp^2 domains upon reduction of the exfoliated GO, indicating that new graphitic domains were created during the reduction process [50].

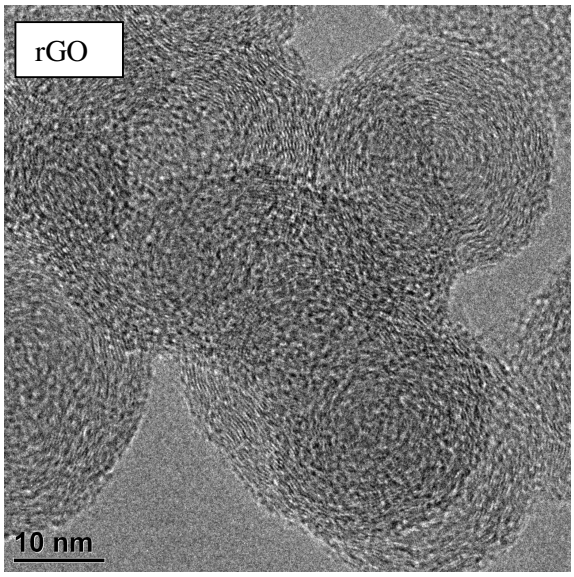

Figure 5-17 TEM image of onion shaped particles of carbon film deposited at RT.

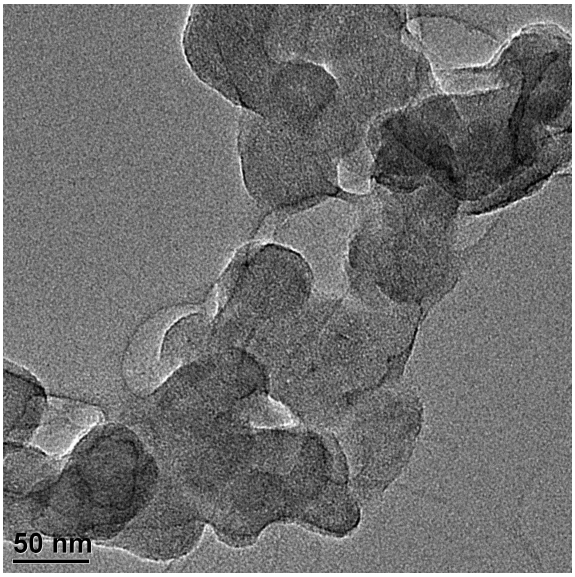

Figure 5-18: TEM image of graphene oxide showing aggregation of sheets.

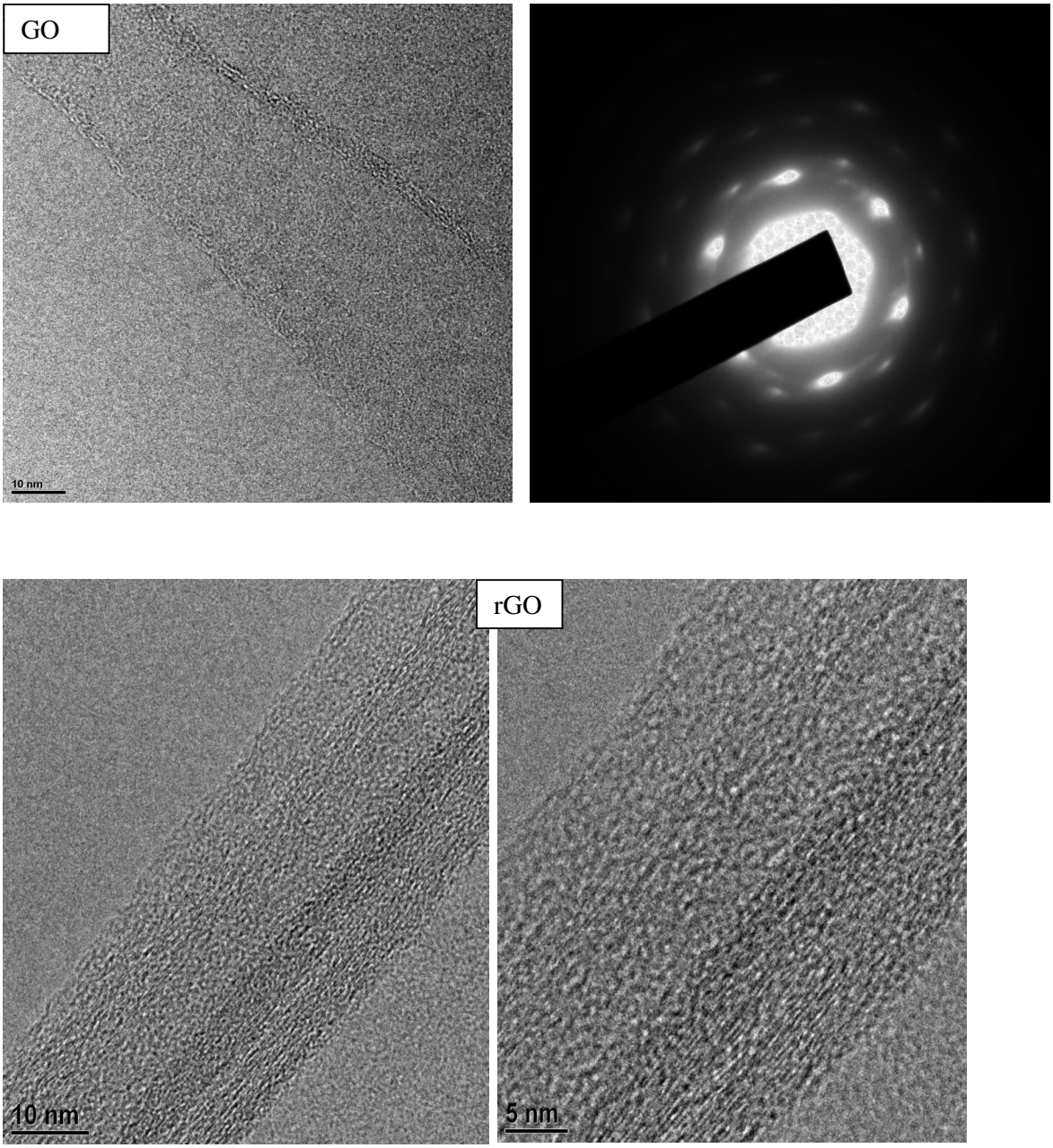

Figure 5-19 TEM images of suspended graphene. Top: GO and electron diffraction pattern , bottom left: rGO and bottom right: zoom rGO edge of two and three layers dominated by two and three dark lines respectively.

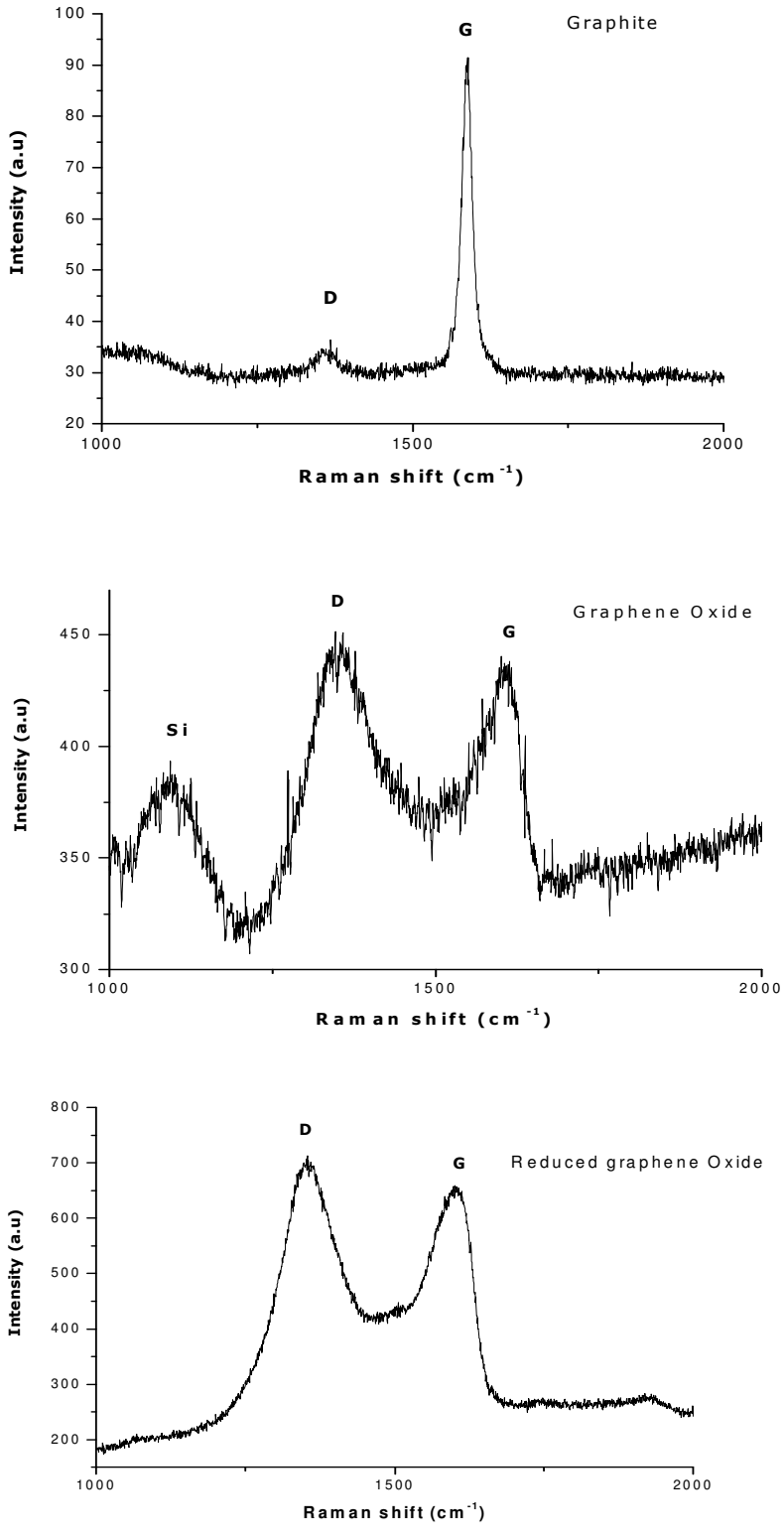

Figure 5-20 Raman spectra of graphite. GO and reduced GO display a disordered D peak at 1359 cm^{-1} and a G peak at 1587 cm^{-1}, corresponding to the first-order scattering of the E_{2g} mode.

5.1.3 Optical properties

TEM samples of suspended graphene oxide and reduced graphene oxide were used to demonstrate the optical properties of the sheets. The chemical reduction process does not have much effect on the optical properties of an individual sheet. The graphene oxide and reduced graphene oxide films are both fairly transparent due to the low Z value of carbon, revealing the copper grid edges on which the samples were deposited. The number of sheets, however, do affect the optical properties. As the number of sheets increases, the transparency of the sheets decreases as can be seen from Figure 5-21. If one has more than 5 layers it is no longer graphene but graphite, and therefore the properties of the sample will resemble that of graphite. The sheets tend to be unstable along the edges and will fold, roll or wrinkle (Figure 5-22) while most parts of the sheet, particularly the central area, are homogeneous and quite smooth.

For the solutions and the samples deposited on glass (Figure 5-22), ultra-violent to visible near infrared spectroscopy measurements were done. It was found that as the concentration of the sheets in distilled water solvent increased the transparency decreased. The as-GO (graphene oxide) was the most concentrated solution. It was diluted with de-ionized water to give the GO-D which was then chemically reduced to rGO-D. The solutions rGO-1, rGO-2, and as-GO chemically reduced, were stages of the same solution taken one after the other. As can be observed, the rGO-2 had a higher transmittance because the sheets had started to precipitate. The final solution was the reference solution GO-G which consisted of fewer sheets in the solution and therefore was the most transparent among the graphene oxide solutions. A description of the solution is given in Table 4. As compared to the unreduced samples the reduced samples are opaque. All of the solutions have a common absorption peak at approximately 972 cm^{-1} which is due to the hydroxyl group asymmetric stretching. The absorption peak at 1630 cm^{-1}, 2105 cm^{-1} and 3303 cm^{-1} are due to the presence of C=N, C=C and O-H functional groups respectively in the solutions presented in Figure 5-23.

The band gaps for the thin films were determined through curve fitting using the semi-empirical Tauc and Davis–Mott model, based on the measurement of optical absorption at the visible and near infrared range as shown in Figure 5-24. The point where the straight line intercepts the x-axis was determined and then converted to energy using the following equation:

$$E_g = \frac{hc}{\lambda}$$

The intercepting wavelength was 312 nm for the rGO-D solution and 301 nm for the rGO, as-GO and GO-G. Converted to the energy band gap these values are 3.98 and 4.12 eV, respectively. All the films have their band gap energies greater than 3.1 eV. Therefore no visible light is absorbed by these films, and if they are of high purity, the films will appear transparent and colourless. These band gaps are higher than those reported in literature but close to that of graphite at 5.6 eV, which is typical of an insulator.

The samples for the ATR-FTIR measurements (see Figure 5-25) were prepared by drop casting from different solutions onto glass substrates. The solution as-GO is the solution which was prepared using the modified Hummers method. After preparation it was diluted to produce the GO-D solution. As-GO dc5 is produced from the as-GO solution drop casted five times onto the glass substrate, followed by an hour of drying. The spectra obtained from GO and rGO are essentially the same except that the absorption peak intensities are considerably reduced in the case of the rGO. The GO for the 5 layered sample spectrum reveals the presence of O-H, C=O stretching of the COOH (carboxylic) groups situated at the edge of the GO. It also shows C=C conjugation and CH_2 at 3390cm^{-1}, 1725cm^{-1}, 1580cm^{-1} and 1433cm^{-1} respectively. The absence of the O-H and C=O peaks for the rGO indicates the removal of the hydroxyl and carboxyl groups during the reduction process. Figure 5-26 The transmission spectra for graphene before and after annealing at 500 ^{0C} for 6 h under a vacuum. The transmittance of the graphene film decreases with annealing due to further reduction of the film and increased number of free electrons.

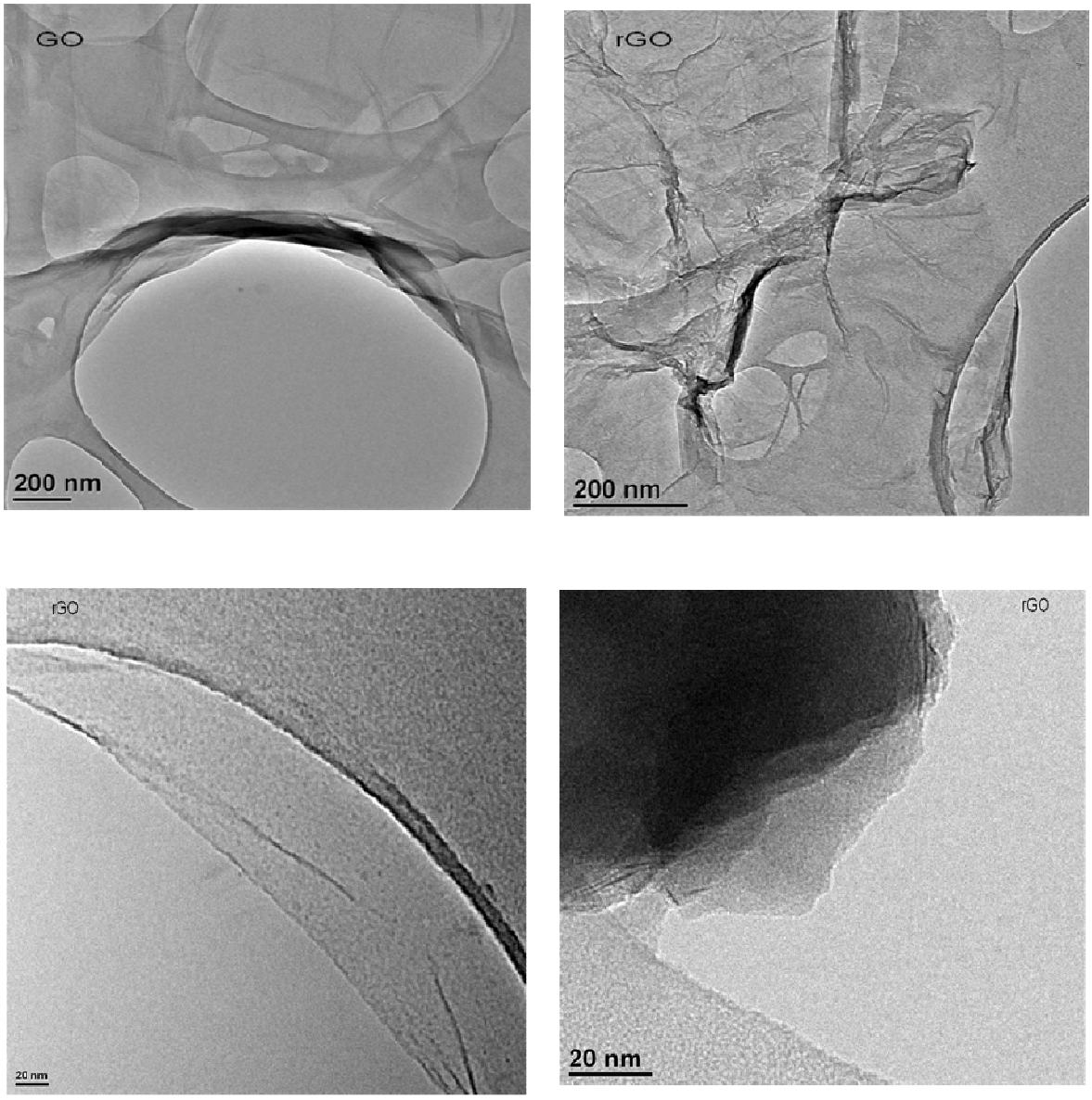

Figure 5-21 The GO and rGO edge respectively. The reduction of GO does not affect the transmittance of individual sheets but the transmittance decreases as the number of layers increases.

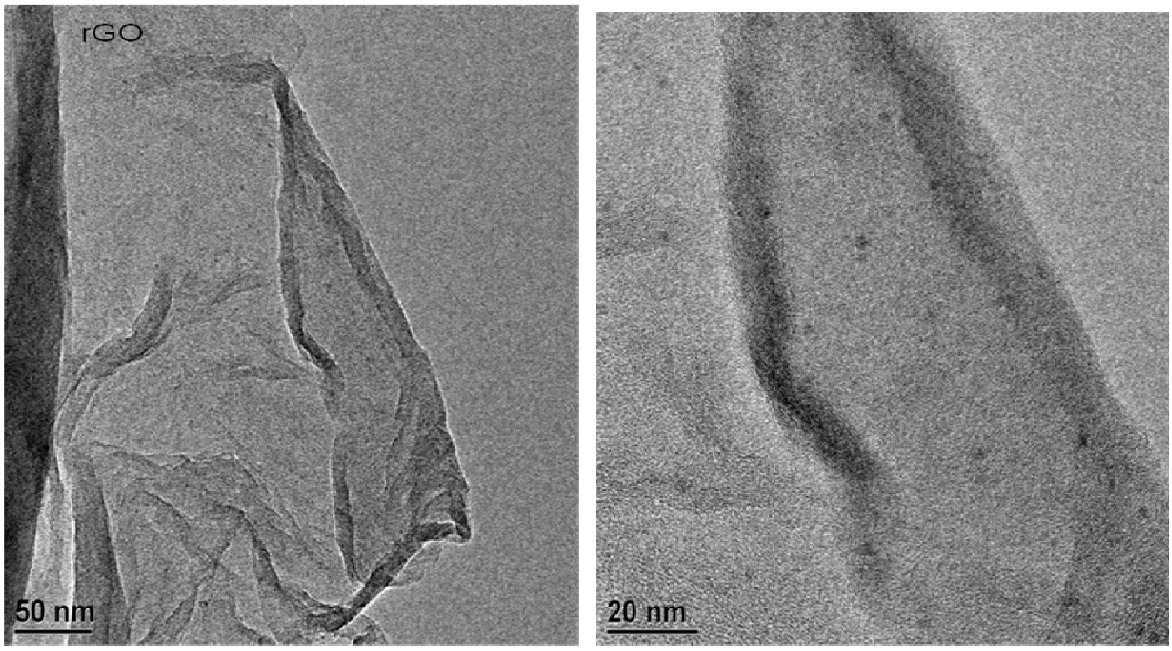

Figure 5-22 The edges of the sheets are unstable and therefore tend to fold and wrinkle.

Table 4 Summary of sample description

Sample	**Description**
As-GO	Concentrated graphene oxide solution
GO-D	As-GO + distilled water (diluted solution of As-GO)
rGO-1	As-GO reduced graphene oxide solution
rGO-2	rGO-1 over time (precipitated rGO-1)
GO-G	GO reference solution (courtesy of Prof. Chhowallas group)
rGO-D	GO-D reduced graphene oxide solution
As-GO dc5	As-GO solution: five layers drop coated

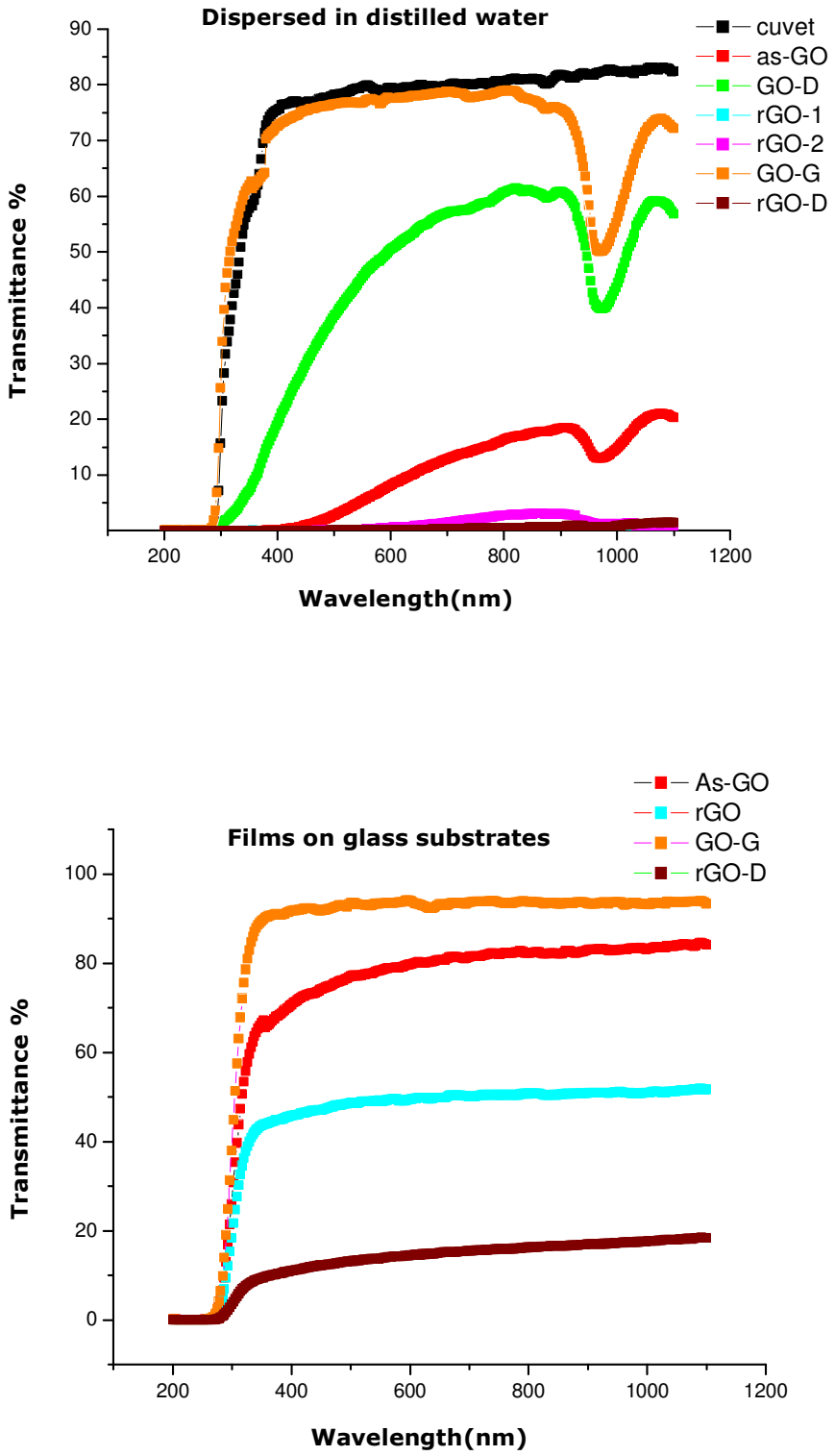

Figure 5-23 Plot of transmittance % as a function of wavelength for graphene oxide and graphene in the ultra-violent and visible ranges.

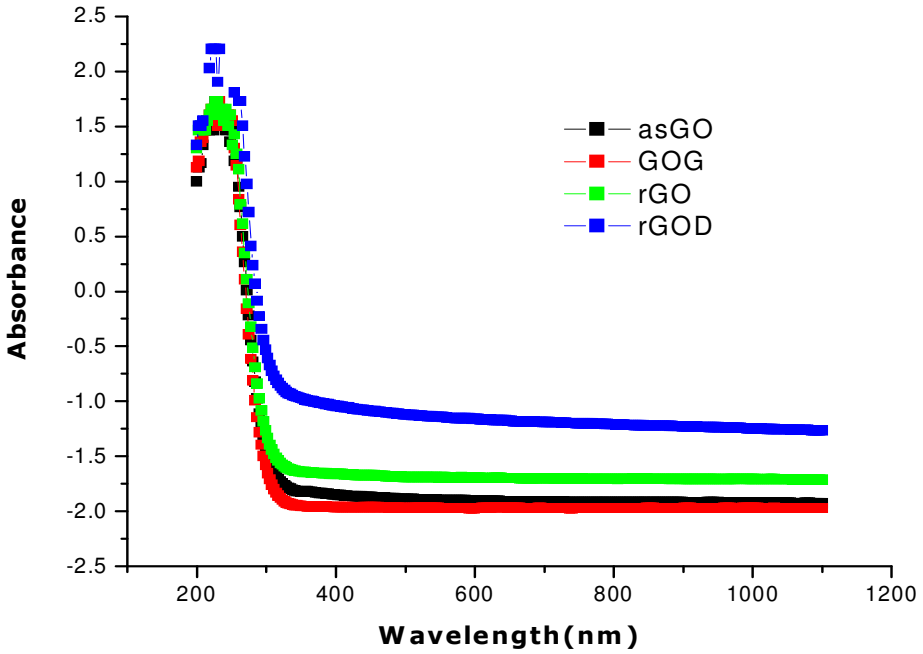

Figure 5-24 Absorption spectra for different graphene films. Most of the films have the same band gap of 4.12 eV while that of the diluted reduced graphene is 3.97 eV; nevertheless they are both above the maximum band gap energy for the absorption of visible light.

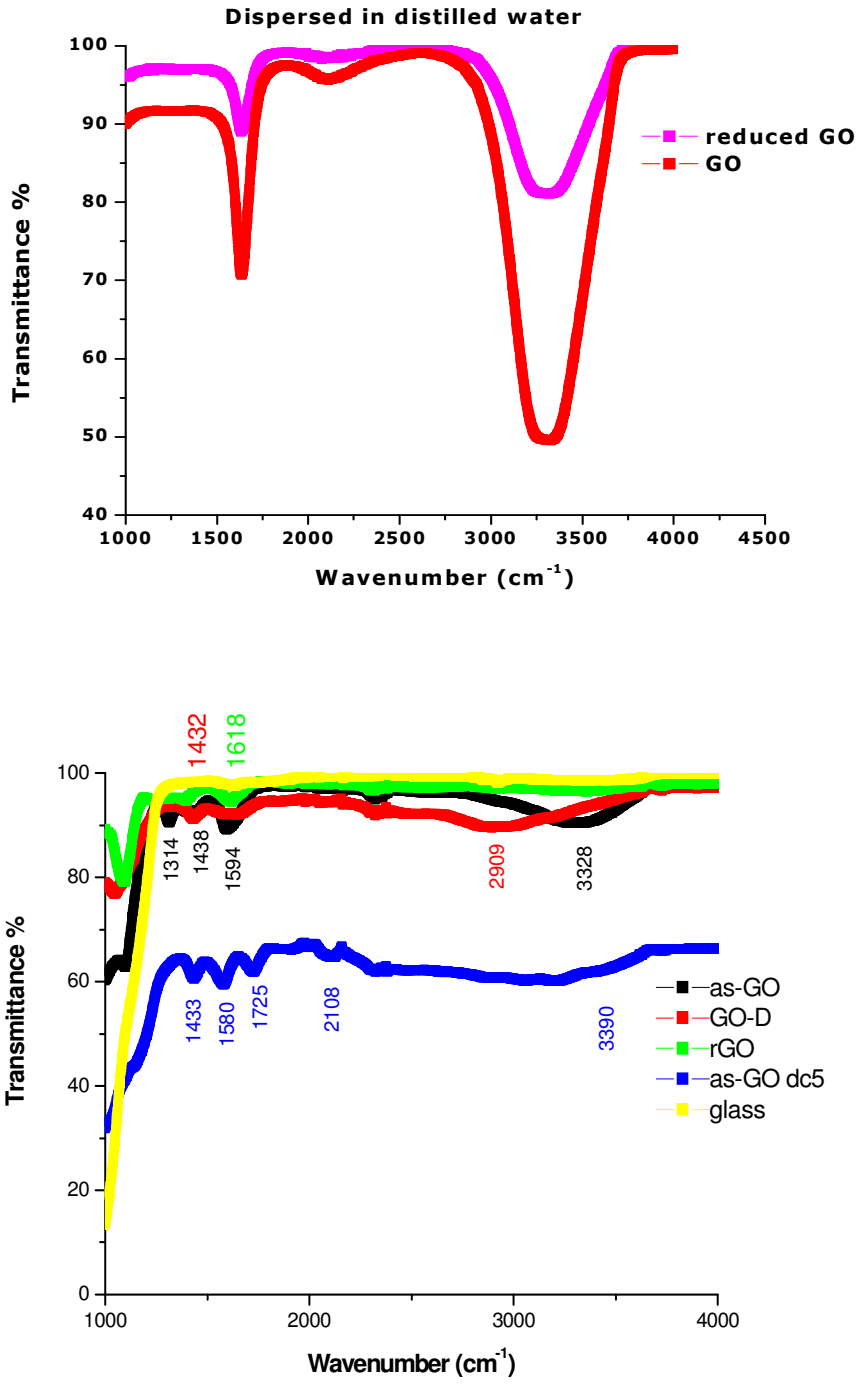

Figure 5-25 Transmittance % plotted as a function of wave number in cm^{-1} for the different chemically treated samples.

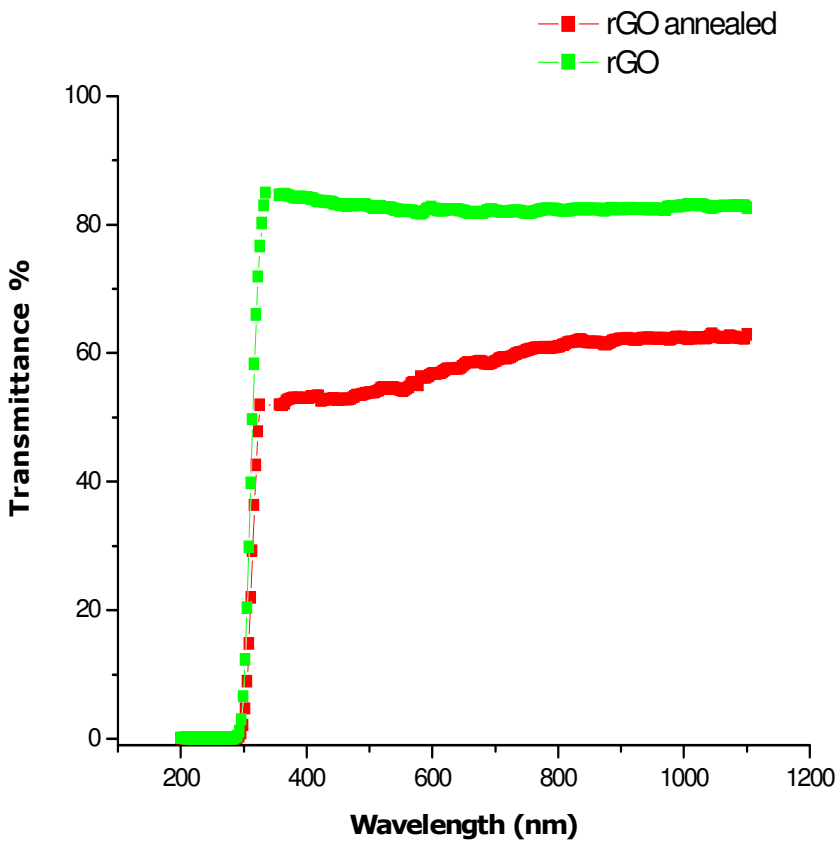

Figure 5-26 The transmission spectra for graphene before and after annealing at 500 ^{0}C for 6 h under a vacuum. The transmittance of the graphene film decreases with annealing due to further reduction of the film and increased number of free electrons.

5.1.4 Current - Voltage Characteristics

The field effect devices were produced by drop casting of a reduced graphene oxide solution onto a 2x2 cm^2 SiO_2 substrate, followed by contacting with silver source- and drain-electrodes on top of the graphene sheets. All the measurements were carried out in a $4x10^{-7}$ Torr vacuum. As the temperature was increased from 44 K to 280 K, the voltage and current data were recorded and plotted. The results are presented in Figure 5-27. It shows that P-type behaviour was observed at voltages ranging from 0 to -16 V and n-type behaviour occured when the polarity was changed as a result of electric field doping. According to the conventional MOSFET model, when a negative gate potential is applied, a positive dc current will recover electrons loss and restore the n-channel transistor. A negative dc bias will enhance the p-channel dominated behaviour. An almost symmetric and hysteresis free behaviour for the electron and hole doping regions is observed, unlike that observed by Inhwa Jung *et al*. [53], when he exposed the graphene oxide devices to room environment or water vapour. When the films were exposed to water vapour there was an increase in the hysteretic response to back gate potential due to the adsorbed molecules becoming polarized in the applied electrical field. In the reverse bias voltages the breakdown voltage, where a large number of charge carriers were generated, was lower at 280 K than at lower temperatures. At temperatures below 280 K the resistance was high but at 280 K the resistance rapidly increased when a reverse bias voltage was applied. This may have been due to a higher hole mobility at higher temperatures but further investigation needs to be done.

Figure 5-27 illustrates that we observed a current of -46 μA at a voltage of -4.58 V, which is an improvement compared to the 25 μA reported by S. Gilje [54] at a source and drain voltage of -5 V. Our measurements were done at considerably larger channel length than the 7 μm of Gilje. This comparison is made regardless of the difference in channel length, because of the results reported by G. Ade [31]: "Of the numerous (>100) TFT devices we tested, all showed uniform transfer characteristics regardless of the channel length". Similar results were reported by Inhwa Jung *et al*. [53]: "The I-V curves are independent of the contact area or length of the electrodes edges, unlike for a 2-probe configuration. Charge transport in graphene oxide is thus not contact-limited; instead, it is space-charge limited." Further studies on numerous samples need to be conducted for concrete conclusions to be made.

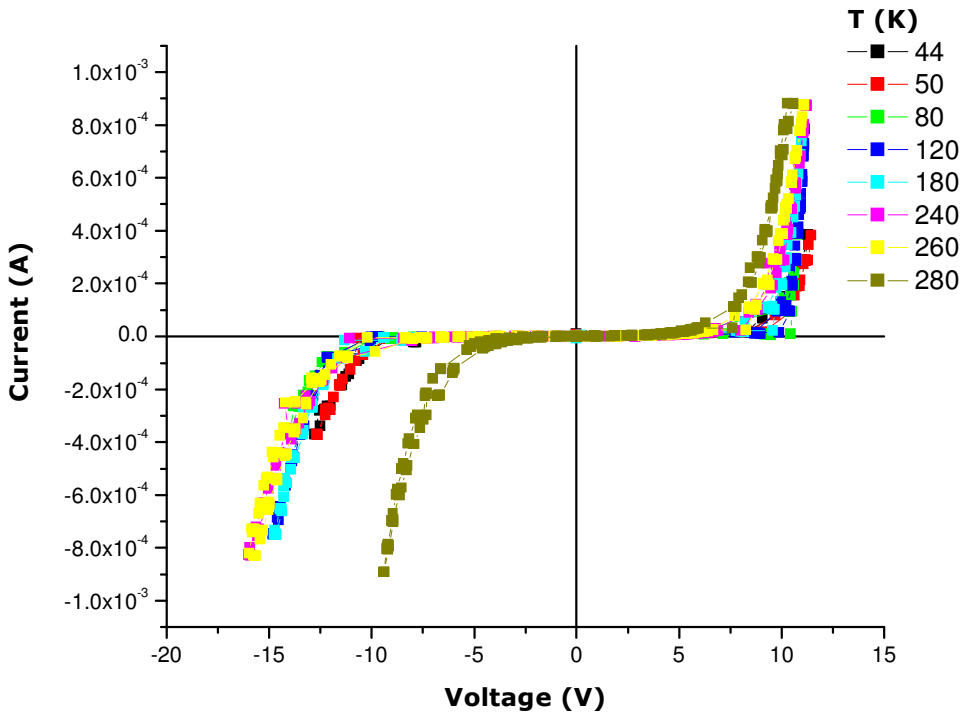

Figure 5-27 The current and voltage characteristics of graphene as a function of temperature.

5.1.5 Raman spectroscopic studies of irradiated graphene

In attempt to record the Raman spectra of multilayered sheets, Raman spectra for the unstable folded edges like the ones displayed in Figure 5-22 were measured. The images captured by the light microscope component of the Raman system, displayed in Figure 5-28, prove this. The bright areas of the images indicate the thicker regions in the image while the faded regions indicate the thinner regions in the sample. The brighter areas in Figure 5-28 (a) to (d) were found at the edges of the sheets from which it could be concluded that they were folded sheet edges. This assumption is further supported by the splitting of the G peak as reported by M. Hulmana *et al*. [23] and M.S Dresselhaus *et al.* [46] for semiconducting single walled nanotubes. The Raman spectra shown in Figure 5-29 (a) to (d) display the same features, i.e. a D, G^- and G^+ peak. The D band is induced in the first order scattering process by the presence of finite size effects, vacancies, grain boundaries etc., all of which lower the symmetry of the quasi infinite lattice. The G peak is due to the doubly degenerate zone centre E_{2g} mode, which is caused by the in-plane bond stretching motion of the pairs of carbon atoms. Figure 5-29, presenting the spectrum for the non-irradiated sheet, indicates that the G-band feature consists of two main components, one peak at 1604 cm^{-1} (G^+) and the other at 1510 cm^{-1} (G^-). The G^+ feature is associated with carbon atom vibrations along the nanotube axis (longitudinal optic phonon mode). The G^- feature in contrast is associated with vibrations of carbon atoms along the circumferential direction of the SWNT (tangential optical phonon mode). Another set of Raman measurements on the previous sample were done, only this time at the centre of the monolayer sheets. The images of the measured sheets are displayed in Figure 5-30. Figure 5-31 compares the 514 nm Raman spectra of sheets irradiated with different fluences. The two most intense features are the D and G peaks as discussed above. The crystallite size was calculated using the Tuinstra and Koening relation [55]:

$$\frac{I(\mathbf{D})}{I(\mathbf{G})} = \frac{C(\lambda)}{L_a}$$

where C (514.5 nm) ≈ 4.4 nm and L_a is the crystallite size. The intensity of the D and G peaks were estimated by fitting the spectra, using a multiple Lorentz fit. The non-irradiated film had a crystalline size of 6.1 nm; this size reduced upon irradiation to ~ 4.1 nm. The characteristics of the Raman spectra for non-irradiated and irradiated samples are different but the spectra for the different

fluences do not change. As illustrated by the stable plot of the ratio of the intensities of the D and G peaks as a function of the proton irradiation dose shown in Figure 5-32, there might be a critical concentration of defects. Further defect production is not favourable and the additional defects are cured. The defects move and coalesce, still leaving enough parts of the graphene lattice unperturbed [23]. The increase in the intensity ratio from the non-irradiated to the irradiated sample indicates a decrease in crystallite size of the irradiated sample. The decrease in the crystallite size is due to the introduction of defects by the irradiation. As the protons pass through the graphene film they interact with the film, causing bonds to break, the formation of new bonds and the creation of vacancies. The resulting defects are not due to proton implantation in the graphene film because carbon has a low Z-value, and the Z-value is proportional to the stopping power. In this work 480 keV protons were used, which have a calculated penetration depth of 9120 nm. Therefore they passed right through the film. If the six carbon atoms accumulate to form a hexagonal structure, the sample will retain its sp^2 hybridization [56].

The results of the Raman spectra characteristics for the UV irradiated sample is similar to that of the proton irradiated sample. It can therefore be concluded that the splitting of the G band as in semiconducting SWNT is an indication that the samples were originally semiconducting, because the splitting can also be observed in the non-radiated sheets. As the sheets are irradiated with the UV laser, a transition from semiconducting to more metallic occurs, because the G^- line shape is highly sensitive to whether the SWNT is metallic or semiconducting. This assumption is also supported by the inspection of images in Figure 5-33, the non-irradiated sample (b) is light in colour but the irradiated samples are black (c-f) and the same is observed at the edge of irradiation (a). This change in colour of the sheets is also observed in the reduction of GO to rGO. As in the proton irradiated samples, the increase in the intensity ratio from the non-irradiated to the irradiated sample indicates a reduction in the average size of the sp^2 domains upon irradiation. This can be explained if new graphitic domains were created that are smaller in size but more numerous in number when the sample was irradiated [57]. These results are in agreement with that observed by S. Mathew *et al*. [56] for graphite samples, irradiated by 2.25 MeV H^+ ions at a fluence of 2×10^{17} ions/cm^2.

The Raman spectrum features for the film irradiated by visible light is similar to that of the proton and UV irradiated spectra, which have already been explained above. But unlike the former the crystalline size increases from 1.82 nm to an average of 2.5 nm which may be due to the stabilization of vacancies produced

by irradiation, by creating pentagon-heptagon defects and at the same time pushing one carbon atom out of the graphene plane. Subsequently, a cross-link between neighbouring graphene layers is formed if they meet each other [23]. On the other hand we know that graphene is transparent to visible light as explained in the optical properties section and the change is not that significant.

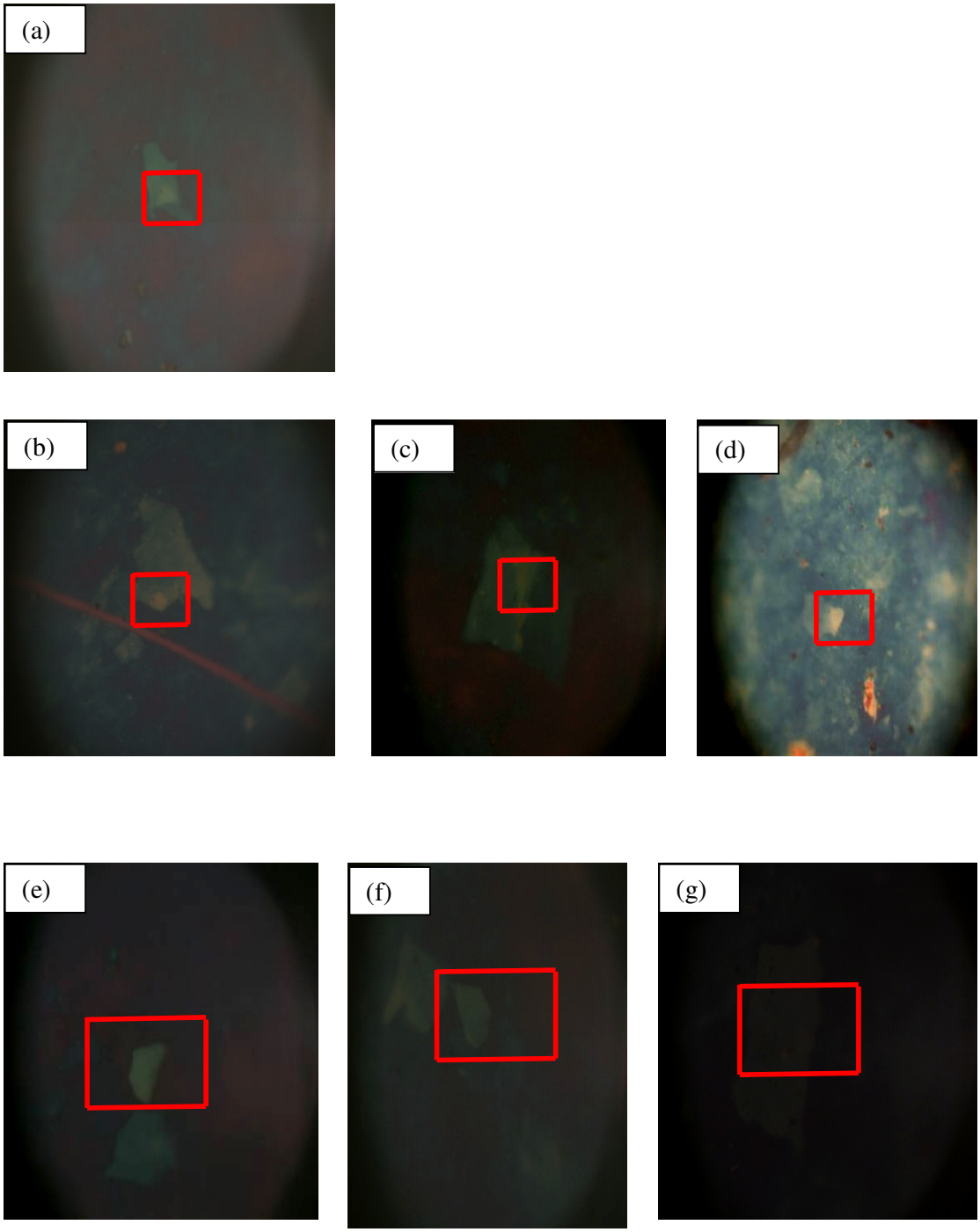

Figure 5-28 Images of proton irradiated sheets. (a) Non-irradiated sheet (b) to (g) Spot 1 to spot 6 respectively. The bright areas of the images indicate the thicker regions in the sample while the faded regions indicate the thinner regions in the sample.

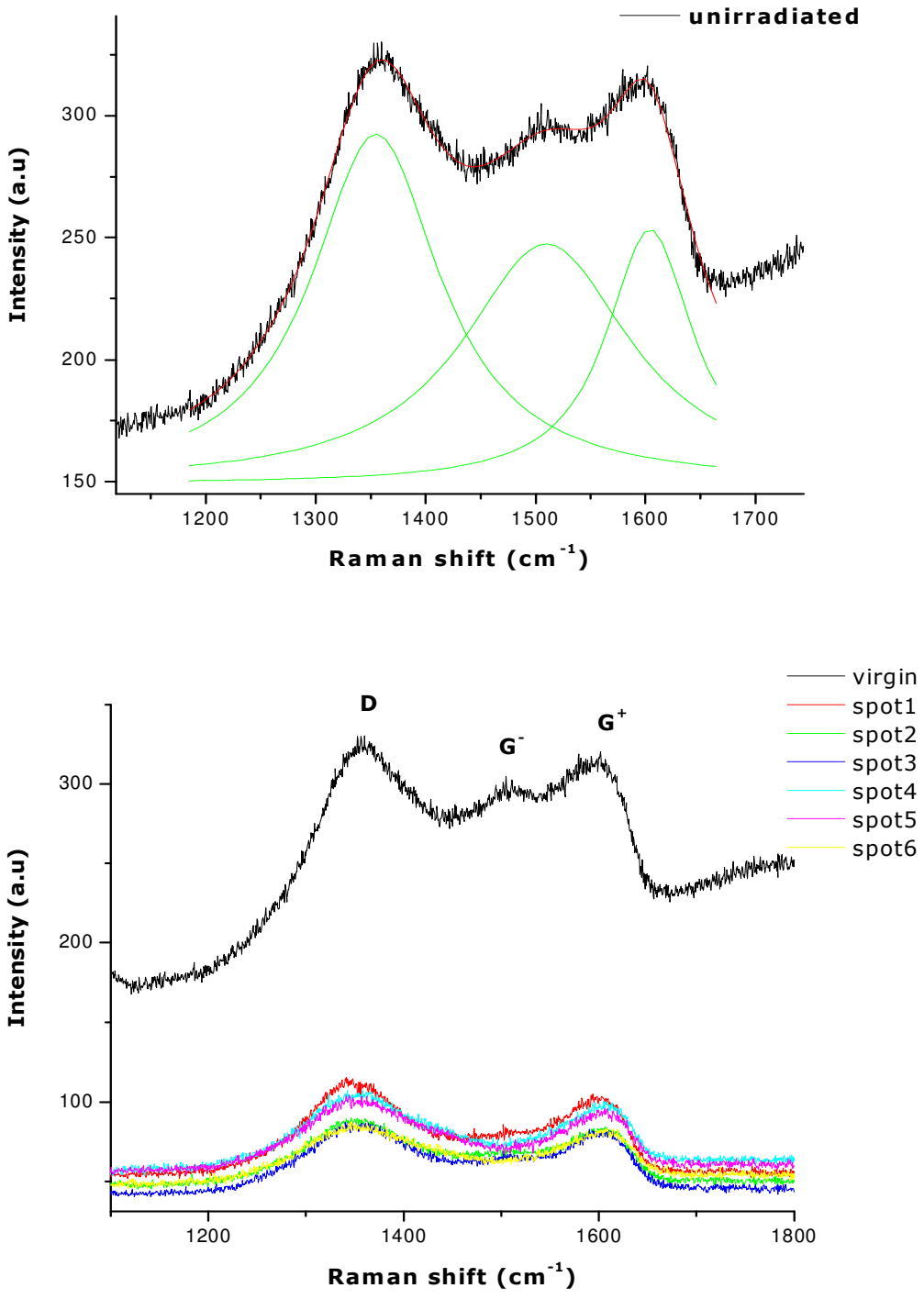

Figure 5-29 Raman spectra of rGO-G films on Si/SiO_2 substrate irradiated with protons. The G^+ feature is associated with carbon atom vibrations along the nanotube axis. The G^- feature in contrast is associated with vibrations of carbon atoms along the circumferential direction of the SWNT. The splitting of the peaks indicates that the measurements were done at a folded edge.

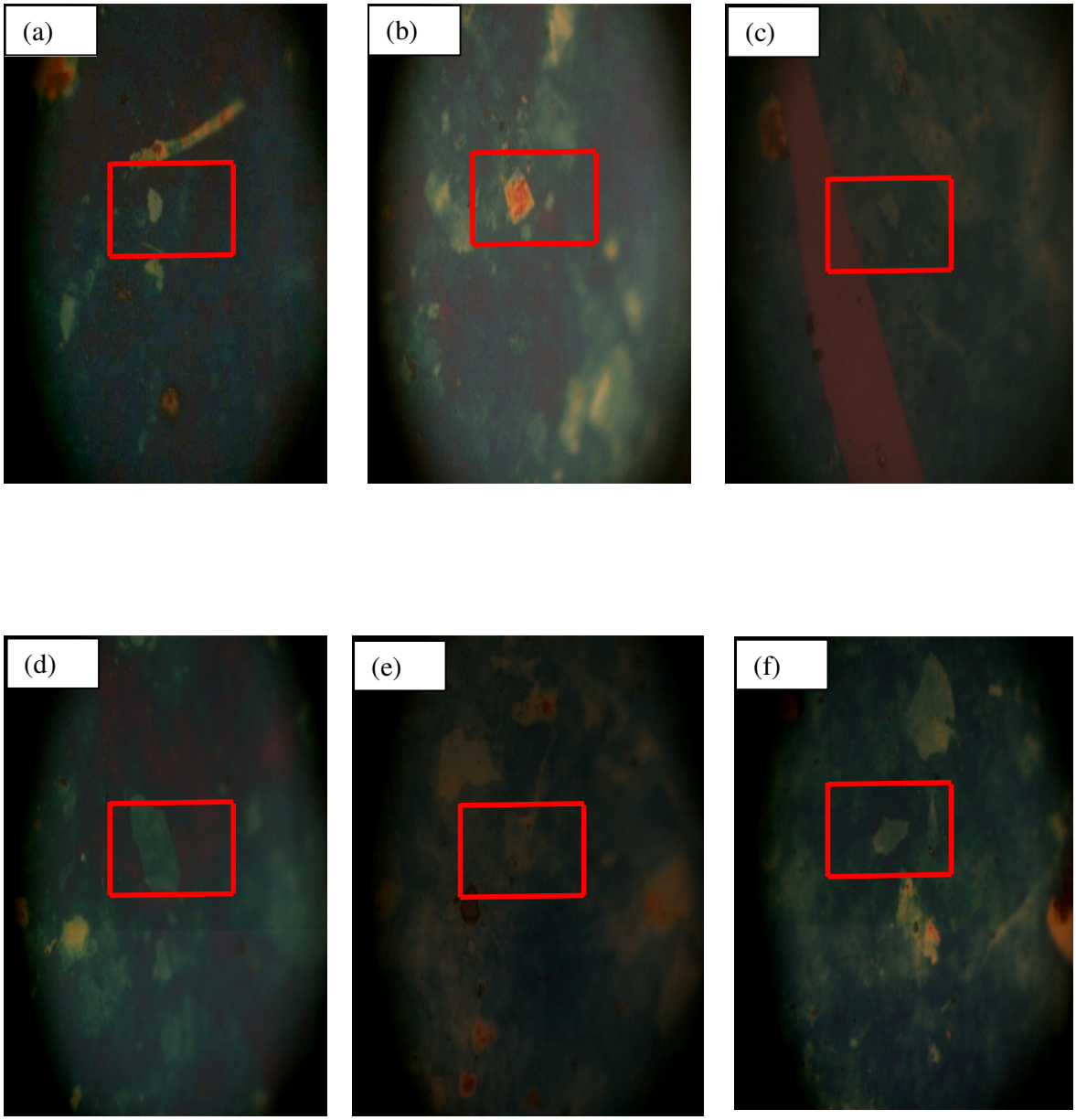

Figure 5-30 Images of proton irradiated sheets. (a) Spot 1: 1.79×10^{16} ions/cm^2 to (f) Spot 6: 1.07×10^{17} ions/cm^2.

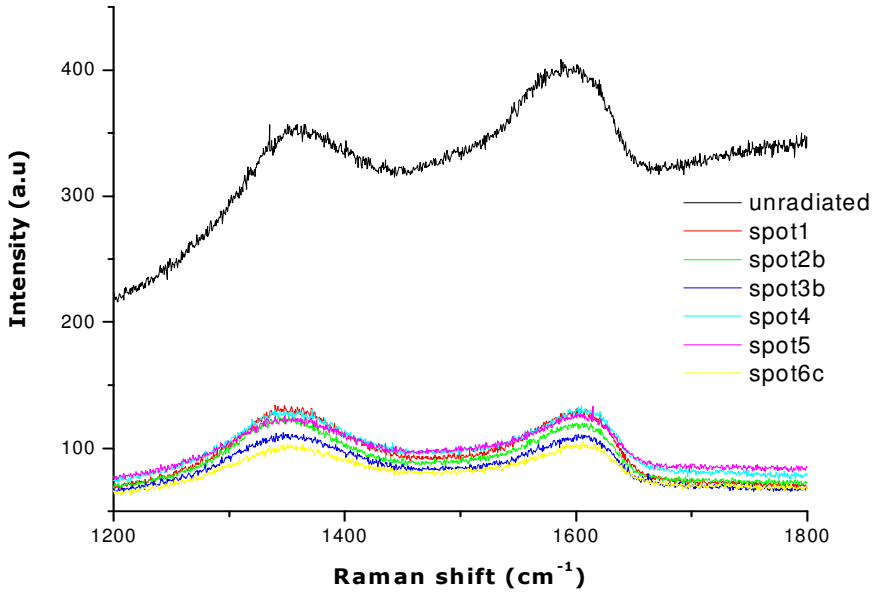

Figure 5-31 Raman spectra of rGO-G films on Si/SiO_2 substrate irradiated with protons with a single sharp D peak confirming, by the visual inspection of Figure 5-31, that the measurements were done on monolayers.

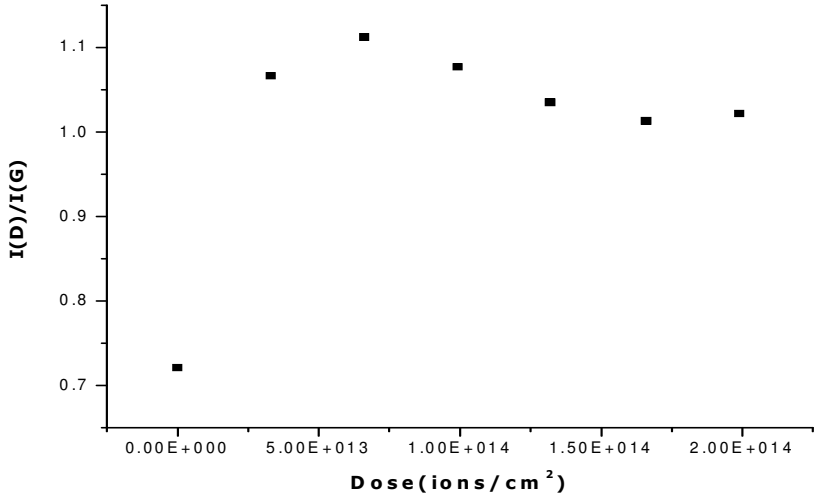

Figure 5-32 Plot of the ratio of the intensities of the D and G peaks as a function of the proton irradiation dose. The increase in the ratio from the non-irradiated to the irradiated sample indicates a decrease in crystallite size of the irradiated sample.

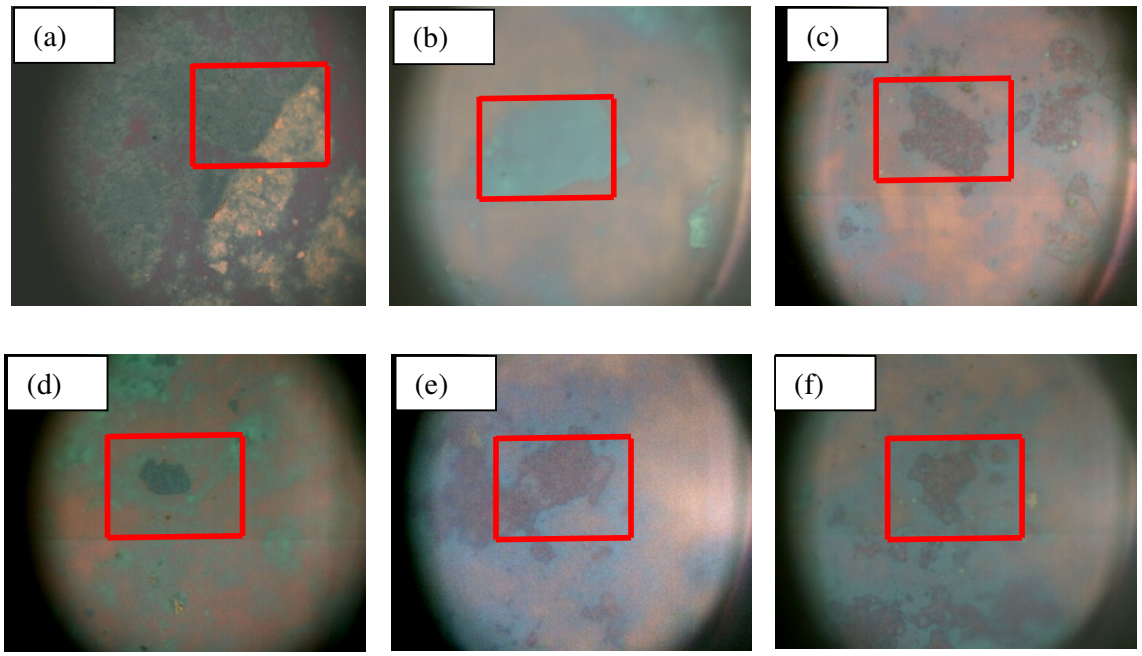

Figure 5-33 Images of UV irradiated sheets: (a) Boundary between irradiated and non-irradiated. The black portion is the area which was irradiated with a mask to focus the beam. (c) Spot 1 =19 keV to (f) Spot 4= 24 keV.

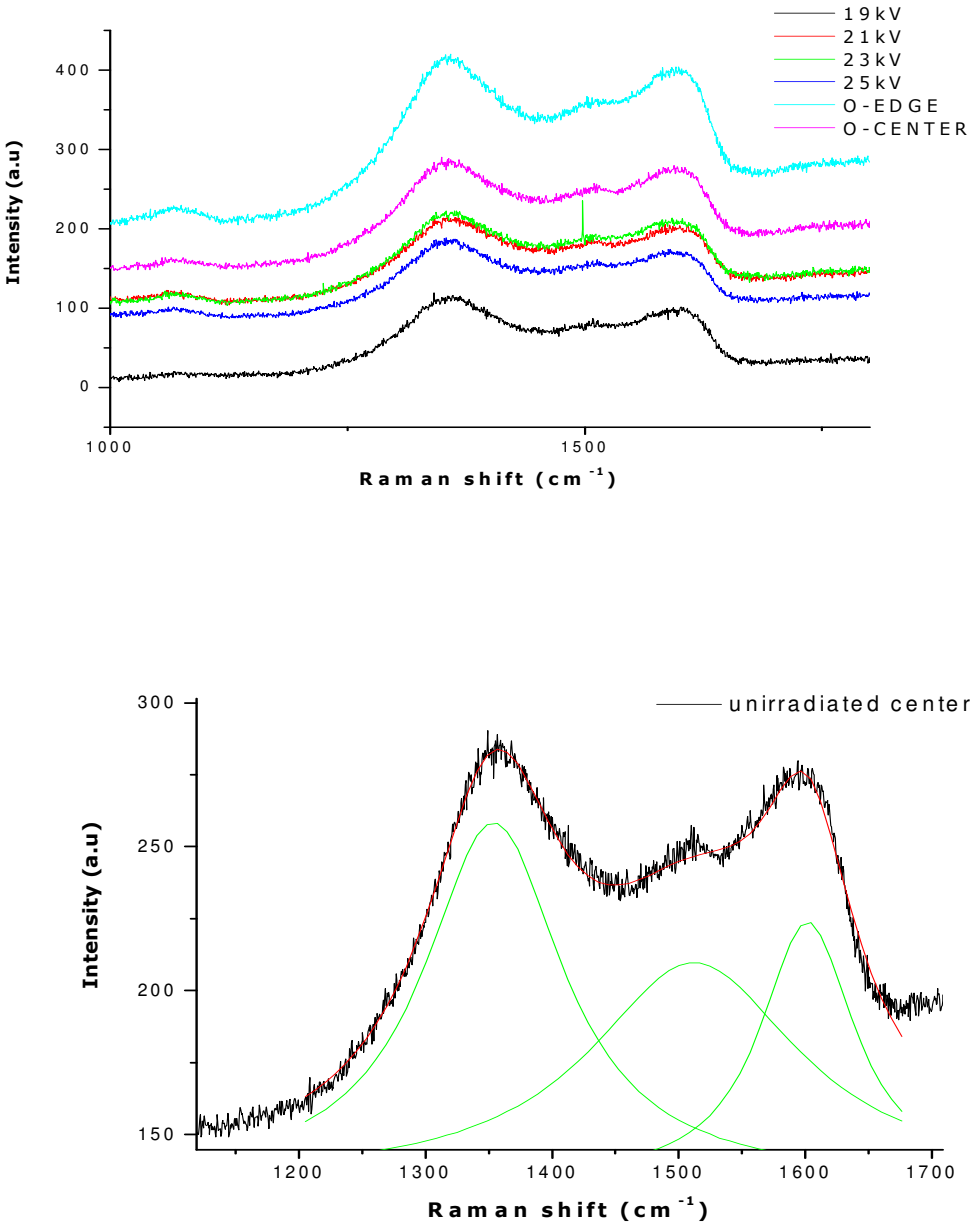

Figure 5-34 Raman spectra of rGO-G films on Si/SiO_2 substrate. After UV irradiation the G peak also consists of two components as in the case of the proton irradiated graphene.

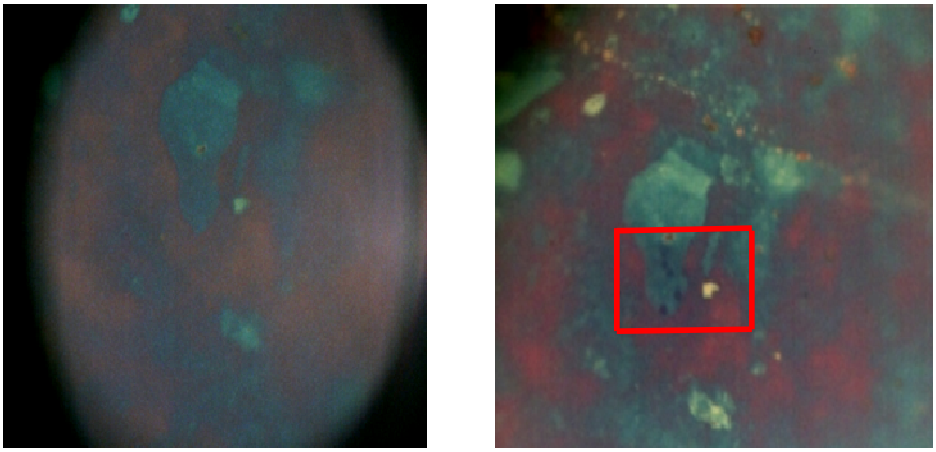

Figure 5-35 Raman spectra of rGO-G films on a Si/SiO_2 substrate for different amounts of the incident power. There was no induced damage of the sheet at 5 mW but above this value there was visible damage, as illustrated by the marks left by the beam.

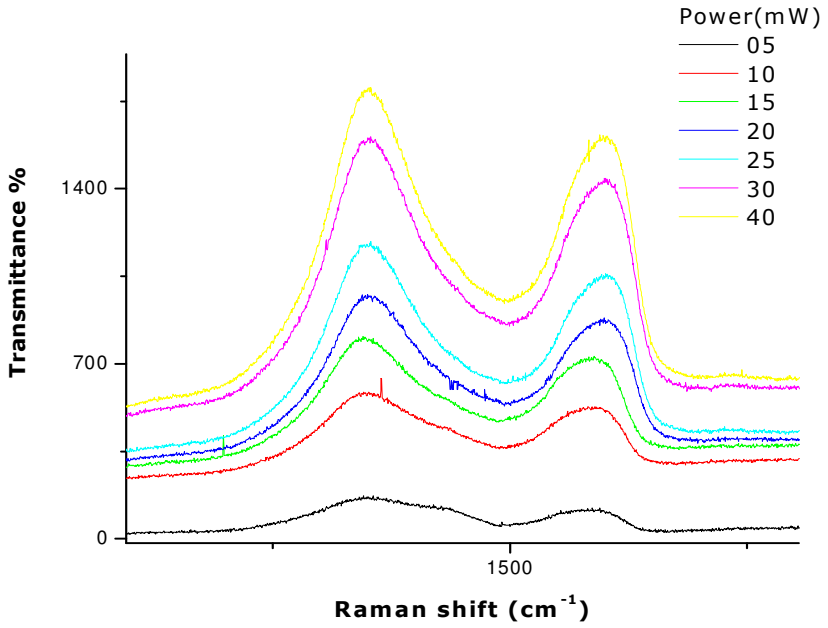

Figure 5-36 Raman spectra of rGO-G films on Si/SiO_2 substrate as a function of the incident power, varying from 5 to 40 mW, when irradiated with visible (green) light.

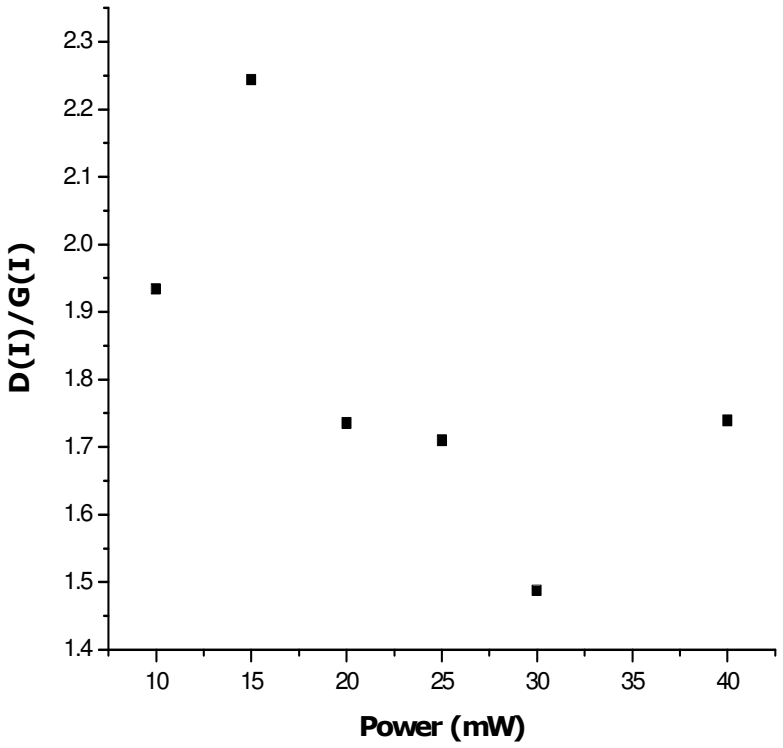

Figure 5-37 D and G peak intensity ratio as a function of the incident power. The net change in the ratio is a decrease but there is no major change.

CHAPTER 6

6.1 Conclusion

Large scale production of single graphene sheets, controlling individual features for reproducibility and homogeneous layer deposition are the challenges of the synthesis process. The individual sheets are irregularly shaped and have a random distribution of size and one of the disadvantages of the Hummers method is that a reduction in the solution stage causes the sheets to aggregate due to the attractive force between layers and decrease in hydrophilicity. The solution based method has numerous disadvantages; the resulting sheets are found to be wrinkled or folded, and cross-sectional step heights of more than 1 nm are often observed for a single sheet. This is larger than the theoretical values due to hydroxyl and epoxide groups and aggregation of the sheets during evaporation when drying the solution. The alternative methods include mechanical exfoliation and heating of silicon carbide at high temperatures, which both have the disadvantage of low yield. Large scale production of single graphene sheets is an important factor for the applications of graphene. Quality is just as important. The alternative methods produce high quality graphene while the chemical route produces defective graphene, with the defects affecting the properties of grapheme, as illustrated by the Raman spectra at different levels of the chemical treatment process. The work done by W.Frank, A. Balandin, K.S Novoselov and G Eda with their groups proves that the properties of graphene produced by the Hummers method are largely reproducable and resemble those of graphite. So despite the numerous disadvantages it is still a convenient production method.

There are a number of parameters to consider when depositing individual graphene sheets. Firstly, the concentration of the solution determines the number of layers produced. In this work the morphology of different layered samples grown by drop casting were studied with the aid of the SEM. It was noted that as the number of deposited layers increased, the stacking of the sheets also increased, but the interesting aspect was that even for the sample that was deposited only once stacking occurred. The solution was diluted 20x and deposited five times by drop casting. It was noted that the sample which consisted of one layer had isolated sheets, while if the number of layers increased it become more difficult to locate isolated graphene sheets. All the evidence presented leads to the conclusion that increasing the number of layers deposited

had the same effect as was obtained by increasing the concentration of the solution. Secondly the drying temperature is important. The sheets are initially dispersed in de-ionized water and drop casted onto a selected substrate and then placed in the oven. The oven has to be sufficiently hot to evaporate the excess of water but not too hot so as to reduce the yellow graphene oxide to black graphene. In the reduced graphene oxide it also plays a role. Although it enhances the properties to that of graphite it compromises the transparency of the sheets. High temperatures also cause the sheets to be unstable and result in the folding of the sheets. Thirdly the deposition method plays a role. Spin coating produces smoother, thinner and less dense sheets, but this can be matched by depositing a solution of an appropriate concentration.

FTIR spectroscopy was done to identify the elements present in the samples. The theory is that bonds vibrate at various frequencies, depending on the elements involved and therefore the wavelength of the light absorbed is characteristic of the chemical bond and element present. The spectra obtained from GO and rGO are essentially the same but the peak intensities have been considerably suppressed in the case of the rGO. The GO spectra show the presence of O-H, C=O stretching of the COOH (carboxylic) groups situated at the edge of the GO C=C conjugation and CH_2 at 3390cm^{-1}, 1725cm^{-1}, 1580cm^{-1} and 1433cm^{-1} respectively. The absence of the O-H and C=O peaks for the rGO indicates the removal of the hydroxyl and carboxylic groups during the reduction process.

The optical properties of the graphene and graphene oxide were investigated with ultraviolet and visible absorption spectroscopy. The transmittance percentage can be as high as 90 % for both rGO and GO but it is also a function of concentration. As the concentration of sheets is increased the transparency decreases. The reduction of the sheets also cause the transparency to decrease. The transparency of the reduced GO can be as high as that of the GO if the sheets concentration is monitored carefully. Another set of measurements were done on the same solution with a time interval between measurements. It was noted that the transmittance increased and observation of the solution revealed that it was a result of the aggregation of the sheets due to the force of attraction between them.

The band gaps for the thin films were determined through curve fitting, using the semi-empirical Tauc and Davis–Mott model, of the optical absorption at the visible and near infrared range. The intercepting wavelength was 312 nm for the rGO-D solution and 301 nm for the rGO, as-GO and GO-G, which converted to energy

band gap values of 3.98 and 4.12 eV respectively. All the films have band gap energies greater than about 3.1 eV, therefore no visible light is absorbed by these films.

Transport measurements were done on graphene deposited onto a SiO_2 substrate. We observed p-type behaviour at voltages ranging from 0 to -16 V and n-type behaviour when the voltage polarity was changed as an effect of electric field doping. Following the conventional MOSFET model, when a negative gate potential is applied, a positive dc current will recover electrons loss and restore the n-channel transistor and a negative dc bias will enhance the p-channel dominated behaviour. In the reverse bias voltages the breakdown voltage, where a large number of charge carries are generated, was observed to be lower at 280 K than at lower temperatures.

Tetsuo Tanabe *et al*. [24] stated: "We propose a new model for interpretation of both damaging and annealing processes. In this model, sp^3 bonding is produced by the displacement effect. This sp^3 bonding along with its cluster growing and shrinkage is then the cause of radiation effects such as turbulence of the basal planes, volume expansion by irradiation and shrinkage by annealing, loss of thermal conductivity, increase of electrical resistivity and other effects". In a nutshell: the changes in the properties are due to the lattice displacement and not the implanted species. The results obtained are in agreement with this model even though they were referring to graphite. The samples were irradiated with protons, ultraviolet and visible range radiation, and in all the irradiations the fluence was increased. The Raman spectra characteristics of the three samples are similar, consisting of the D and G mode. The D band is induced in the first order scattering process by the presence of finite size effects, vacancies and grain boundaries, all of which lower the symmetry of the quasi infinite lattice. The G peak is due to the doubly degenerate zone centre E_{2g} mode, due to the in-plane bond stretching motion of the pairs of carbon atoms. The results of the Raman spectra characteristics for the UV irradiated sample is similar to that of the proton irradiated sample in that in both cases there is a splitting of the G mode. The G^+ feature is associated with carbon atom vibrations along the nanotube axis (longitudinal optic phonon mode). The G^- feature, in contrast, is associated with vibrations of carbon atoms along the circumferential direction of the SWNT (tangential optical phonon mode). It can therefore be concluded that the splitting of the G band as in semiconducting SWNT is an indication that the samples are semiconducting, because there is splitting even in the non-irradiated film. However the G^- line shape is highly sensitive to whether the SWNT is metallic or semiconducting and in the UV irradiated sample there is a transition from

semiconducting to more metallic [41]. This assumption is also supported by the images in Figure 5-33. The non-irradiated sample (b) is light in colour but the irradiated samples are black (c-f) and the same is observed at the edge of irradiation (a). This change in colour of the sheets is also observed in the reduction of GO to rGO. In the proton and UV laser irradiated sheets, there was an increase in the D intensity and G intensity ratio from the non-irradiated to the irradiated sample indicating a reduction in the average size of the sp^2 domains upon irradiation. This can be explained if new graphitic domains were created that are smaller in size but more numerous in number, when the samples were irradiated. In the visible light irradiated sheets, the crystalline size increases from 1.82 nm to an average of 2.5 nm which may be due to the stabilization of vacancies produced by irradiation, by creating pentagon-heptagon defects and at the same time pushing one carbon atom out of the graphene plane. Subsequently, a cross-link between neighbouring graphene layers is formed if they meet each other. On the other hand we know that graphene is transparent to visible light, as was explained in the optical properties section and the change is not that significant.

6.2 References

[1] B. Boer, J.L. Kloosterman , D. Lathouwers and T.H.J.J. van der Hagen. *In-core fuel management optimization of pebble-bed reactors*. Annals of Nuclear Science and Engineering36(8), 1049-1058 (2009)

[2] www.sibmar.org/manchester/graphene_membranes/index.html (February 2009)

[3] A.K. Geim and K.S. Novoselov.*The Rise of Graphene*. Nature Materials 6, 183-191(2007).

[4] invsee.asu.edu/nmodules/Carbonmod/bonding.html (February 2009)

[5] J Buckley, D Edie. *Carbon-carbon materials and composites*. Noyes Publication,NJ(1993)

[6] H.0 Pierson. *Handbook of carbon, graphite, diamond, and fullerenes : properties, processing, and applications.* Noyes Publications, NJ(1993)

[7] K.S. Novoselov, A.K. Geim, S.V.Morozov, D.Jiang, M.I.Katsnelson, I.V.Grigorieva, S.V.Dubonos and A.A.Firsov. *Two-Dimensional Gas of Massless Dirac Fermions in Graphene*.Nature 438, 197-200 (2005).

[8] M.I Katsnelson *Optical properties of graphene: The Fermi-liquid approach.* EPL, 84 37001(2008)

[9] S.A. Mikhailov. *Electromagnetic response of electrons in graphene: Non-linear effects*. Physica E40 ,2626–2629(2008)

[10] S.V. Syzranov , M.V. Fistul and K.B. Efetov*. Effects of raditation on transport in graphene*. Phys. Rev. B 78, 045407 (2008)

[11] Jiajie Liang, Yan Wang. *Electromagnetic interference shielding of graphene/epoxy Composites*. Carbon 47, 922-923(2009)

[12] Goki Eda, H. Emrah Unalan, Nalin Rupesinghe, Gehan A. J. Amaratunga, Manish Chhowalla. *Field emission from graphene based composites thin film.* Applied physics letters 93, 233502 (2008)

[13] Zhong-Shuai Wu, Wencai Ren, Libo Gao, Bilu Liu, Chuanbin Jiang, Hui-Ming Cheng. *Synthesis of high-quality graphene with a pre-determined number of layers*. Carbon47, 4 9 3 –4 9 9(2009)

[14] Antonio Castro Neto, Francisco Guinea and Nuno Miguel Peres.*Drawing conclusions from graphene*. Physics World (2006)

[15] I. W. Frank , D. M. Tanenbauma , A. M. van der Zande and P. L. McEuen*. Mechanical properties of suspended graphene sheets.* J. Vac. Sci. Technol. B 2(6) (2007)

[16] A. Balandin, S. Ghosh, W. Bao,I. Calizo,D. Teweldebrhan, Feng Miao, Chun Ning Lau.*Superior Thermal Conductivity of Single-Layer Graphene.* Nano Letters 8 (3), 902-907 (2008)

[17] K.S. Novoselov, A.K. Geim, S.V. Morozov, D. Jiang, Y. Zhang, S.V. Dubonos, I.V.Grigorieva, A.A. Firso*v. Electric Field Effect in Atomically Thin Carbon Films*. Science 22 (2004)

[18] Goki Eda, Yun-Yue Lin, Steve Miller, Chun-Wei Chen, Wei-Fang Su, and Manish Chhowalla. *Transparent and conducting electrodes for organic electronics from reduced GO*. Applied Physics Letters 92 (2008)

[19] Miroslav Pardy.*The photo-electric effect in the bi-layer graphite*. arXiv: 0707.2668v2 [hep-ph] (2008)

[20] F.J. L´opez-Rodr´ıguez, G.G. Naumis. *Electrons and holes in graphene under electromagnetic waves: gap appearance and non-linear effects*. arXiv:0809.4284v3 cond-mat.mtrl-sci 3(2009)

[21] S. A. Mikhailov. *Non-linear electromagnetic response of graphene*. arXiv:0704.1909v1 [cond-mat.mes-hall]. (2007)

[22] R. H. Telling, C. P. Ewels, A. A. El-Barbary and M. I. Heggie. *Wigner defects bridge the graphite gap.* Nmat 876 (2003)

[23] Martin Hulmana, Viera Skákalová, Siegmar Roth and Hans Kuzmany. *Raman spectroscopy of single-wall carbon nanotubes and graphite irradiated by rays.* Journal of Applied Physics 98, (2005)

[24] Tetsuo Tanabe. *Radiation Damage of Graphite - Degradation of Material Parameters and Defect Structures.* Physica Scripta. Vol. T64, 7-16(1996)

[25] K Won Lee and C Eui Lee. *Structural Modification in Proton Irradiated Highly-Oriented*. Journal of the Korean Physical Society 6,2468-2471(2009)

[26] H. S. S. Ramakrishna Matte, K. S. Subrahmanyam , C. N. R. Rao. *Novel magnetic properties of graphene: Presence of bothferromagnetic and antiferromagnetic features and other aspects.* J. Phys. Chem. C, 113 (23), 9982–9985 (2009)

[27] Xiaoying Yang, Xiaoyan Zhang, Zunfeng Liu, Yanfeng Ma, Yi Huang, Yongsheng Chen. *High-Efficiency Loading and Controlled Release of Doxorubicin Hydrochloride on graphene oxide*. J. Phys. Chem. C, 112, 17554–17558 (2008)

[28] Vincent C. Tung, Matthew J. Allen, Yang Yang and Richard B. Kaner. *High throughput solution processing of large scale graphene*. NNANO 329(2008)

[29] P. Sutter.*Epitaxial graphene*.Nature materials 8(3),(2009)

[30] Xiaolin Li, Guangyu Zhang, Xuedong Bai, Xiaoming Sun, Xinran Wang, Enge Wang, Hongjie Dai. *Highly Conducting Graphene Sheets and Langmuir-Blodgett Films.* Nature Nanotechnology, 538-542 (2009)

[31] Goki Eda, Giovanni Fanchini , Manish Chhowalla. *For large-area ultra-thin films of reduced graphene oxide as a transparent and flexible electronic material*.Nature Nanotechnology 3, 270 - 274 (2008)

[32]Guoxiu Wang, Bei Wang, Jinsoo Park, Juan Yang, Xiaoping Shen, Jane Yao. S*ynthesis of enhanced hydropholic and hydrophobic graphene oxide nanosheets by solvothermal method.* carbon47, 68-72 (2009)

[33] T Jeremy ,T. Robinson, M Zalalutdinov, J. W Baldwin, E.S Snow, Z Wei, P Sheehan, and H. Houston. *Wafer-scale Reduced Graphene Oxide Films for Nanomechanical Devices*. Nano Letters 8 (10), 3441-3445 (2008)

[34] P.C. Mayan Kutty ,T.S. Thankachan, Al Jubail Abdullah Al Ajlan and Ghazzai Al Mutairi,Amer Al Rabeh, *Decomposition of Hydrazine in preserved boilers*. Technical Report No. SWCC RDC(1993)

[35] www.nanoscience.com(march2009)

[36] NanoSurf.*easyScan 2FlexAFM Operating instructions*. version 2.1, revision 2.

[37] C. Blanchard. *Atomic Force Microscopy. The Chemical Educator* 1(5),(1996)

[38] P.J Goodnew, J.Humphreys ,R. Branland, *Electron Microscopy and analyses*. 3rd edition 122-166 Teylor and Frecis Group (2001)

[39]http://nobelprize.org/educational_games/physics/microscopes/1.html(July2009)

[40] B Fultz, J Howe. *Transmission Electron Microscopy and Diffractometry of Materials*. 3rd edition, Springer Berlin Heidelberg (2008)

[41] http://www.wcaslab.com/TECH/tech2.htm (march2009)

[42] Daniel T. Schwartz. *Raman Spectroscopy: Introductory Tutorial*

[43] W. Uhmann, A. Becker, C. Taran, and F. Siebert. *Time-Resolved FT-IR Absorption Spectroscopy Using a Step-Scan Interferometer*. Appl. Spectrosc. 45, 390-397 (1991)

[44] Xiaoying Yang, Xiaoyan Zhang, Zunfeng Liu, Yanfeng Ma, Yi Huang, Yongsheng Chen.*High-Efficiency Loading and Controlled Release of Doxorubicin Hydrochloride on graphene oxide*. J. Phys. Chem. C, 112, 17554–17558 (2008)

[45] http://physics.nist.gov/Divisions/Div844/div844(march2009)

[46] M.S Dresselhaus, G. Dresselhaus, R. Saito, A.Jorio. *Raman spectroscopy of carbon nanotubes.* Physics Report 409, 47-99 (2005)

[47] Brian M. *Ultraviolet and Visible Absorption Spectroscopy (UV-Vis)*. National Physics laboratory(2009)

[48] W Callister, J. Material Science and Engineering an Introduction. 6th edition John Wiley and Sons,Inc.(2003)

[49] Xinming Li, Hongwei Zhu , Jinquan Wei, Kunlin Wang, Eryang Xu, Zhen Li and Dehai Wu. *Determination of band gaps of self-assembled carbon nanotube films using Tauc/Davis–Mott model*. Applied Physics A: Materials Science & Processing 97 (2009)

[50] Sungjin Park, Jinho An, Richard D. Piner, Inhwa Jung, Dongxing Yang, Aruna Velamakanni. *et al*. *Aqueous Suspension and Characterization of Chemically Modified Graphene Sheets*.Chem. Mater 20, (21) 6592-6594 (2008)

[51] J.T. Robinson, F. K Perkins, E.S Snow, Z Wei and P.E Sheehan*. Reduced Graphene Oxide Molecular Sensors*. *Nano Letters* 8 (10), 3137-3140 (2008)

[52] E. Cappelli, S. Orlando, V. Morandi, M. Servidori, C. Scilletta. *Nano-graphene growth and texturing by Nd:YAG pulsed laser ablation of graphite on silicon*. Journal of physics 59, 616-624 (2007)

[53] Inhwa Jung, Dmitriy A. Dikin, Richard D. Piner and Rodney S. Ruoff. *Tunable Electrical Conductivity of Individual Graphene Oxide Sheets Reduced at "Low" Temperatures.* Nano Letter 8, 323–327 (2008)

[54] S. Gilje, S. Han, M. S. Wang, K. L. Wang &, R. B Kaner*. A chemical route to graphene for device applications*. Nano Letter 7, 3394–3398 (2007).

[55] F. Tuinstra and J.L. Koening, Journal of Chemical Physics53, 1126 (1970)

[56] S. Mathew, B. Joseph, B.R. Sekhara and B.N. Dev*. X-ray photoelectron and Raman spectroscopic studies of MeV proton irradiated graphite*. Nuclear Instruments and Methods in Physics Research (266), 3241-3246 (2008)

[57] S. Stankovich, D. Dikin, R. Piner, K. Kohlhaas, A. Kleinhammes, Y. Jia, Y. Wu, S. Nguyen, R. Ruoff. *Synthesis of graphene based nanosheets via chemical reduction.* Carbon 45, 1558–1565 (2007).